Unterschrift BetreuerIn

DIPLOMARBEIT

Study of Λ_c^+, Ξ_c^0 and Ξ_c^+ Charmed Baryons using Belle II Data at the $\Upsilon(4S)$ energy

ausgeführt am Institut für Hochenergiephysik der Österreichischen Akademie der Wissenschaften
zur Erlangung des akademischen Grades

Diplom-Ingenieur

im Rahmen des Studiums

Technische Physik

unter der Anleitung von

Privatdoz. Dipl.-Ing. Dr.techn. Christoph Schwanda

eingereicht an der Technischen Universität Wien von

Cristhian Ricaurte, BSc
Matr.Nr.: 01208517

March 21, 2025

Unterschrift StudentIn

Abstract

The spectroscopy of Charmed Baryons presents a field of study that is yet to be well understood; this is despite the great experimental and theoretical progress of the past decade. There exists a plethora of resonances that have been observed whose true compositions and quantum numbers are unknown, and in a similar token, there are states that are predicted by various models but have not been observed.
In this work, we study the ground-state singly charmed baryons allocated to an SU(3) $J^P = \frac{1}{2}^+$ antisymmetric antitriplet symmetry of flavor space: $\Lambda_c^+(udc)$, $\Xi_c^0(dsc)$ and $\Xi_c^+(usc)$. These charmed baryons decay weakly into hadrons such as protons, pions and kaons, as well as strange baryons (hyperons).
Using up to 90.16 fb^{-1} of integrated luminosity data collected by the Belle II detector from events corresponding to e^+e^- collisions at near the $\Upsilon(4S)$ energy, we reconstruct charmed baryons from combinations of hadrons and other final state particles, particularly of the channel modes: $\Lambda_c^+ \to pK^-\pi^+$, $\Xi_c^0 \to \Xi^-\pi^+, \Lambda^0 K^-\pi^+$ and $\Xi_c^+ \to \Xi^-\pi^+\pi^+, \Lambda^0 K^-\pi^+\pi^+$, with the secondary decays $\Xi^- \to \Lambda^0\pi^-$, and $\Lambda^0 \to p\pi^-$. The charge conjugate combinations of every mode are also included in the reconstruction.
We distribute reconstructed events primarily in their invariant mass and x_p value. The x_p variable represents the ratio of the center-of-mass momentum of the charmed baryons to the total available momentum from the e^+e^- collision. By optimizing the x_p distributions of the charmed baryon candidates to the true signal in Monte Carlo simulations, we gain insights into the preferred prompt mechanism and kinematic regimes for the production of optimal signal events.
In this thesis, it is demonstrated that the reconstruction of charmed baryons at Belle II is optimal for events from prompt $c\bar{c}$ fragmentations. Beyond establishing an optimal selection criteria for the reconstructed charmed and strange baryons, we also provide a measurement of the ratios of branching fractions $\mathcal{B}(\Xi_c^0 \to \Lambda^0 K^-\pi^+)/\mathcal{B}(\Xi_c^0 \to \Xi^-\pi^+)$, and $\mathcal{B}(\Xi_c^+ \to \Lambda^0 K^-\pi^+\pi^+)/\mathcal{B}(\Xi_c^+ \to \Xi^-\pi^+\pi^+)$.

Acknowledgement

I would like to thank the Belle II collaboration for making this study possible. Special thanks go to the institute of High Energy Physics (HEPHY). My passion for particle physics was sparked by its inspiring teachers, organizers, and colleagues whom I had the privilege of meeting. I am grateful to my colleague Nikolaus Schneider for his great company and invaluable help during the research phase leading to my thesis. I would also like to thank Dr. Daniel Dorner for his many helpful tips related to the analysis of Belle II data. With great appreciation, I thank Dr. Philipp Horak for the insightful support I received during the many challenges I faced.

My deepest gratitude goes to my adviser, Dr. Christoph Schwanda, for his skillful guidance and incredible dedication. Through his support, I had the privilege of getting my first glimpse into what it feels like to be a particle physicist, and I am immensely grateful for this opportunity.

I would also like to express my profound gratitude to my wife, whose unwavering support and love has been with me every step of the way. I am deeply thankful to my best friend, whose curiosity continues to inspire mine.

Contents

1. Introduction

The discovery of the J/ψ resonance in 1974 [1, 2] played a crucial role in solidifying the idea that hadrons, such as protons and neutrons, are made up of even smaller constituents, called quarks. At the time, the properties assigned to hadrons included isospin and strangeness, where the former described the hadron composition involving up-quarks (u) and down-quarks (d), and the latter represented the strange-quark (s) composition. The J/ψ particle was found in both electron-positron [1] and hadron [2] collisions, and its excitations [3] undisputedly indicated a new property—charmness—that involved a new quark type, the charm quark (c). Charmness became a natural extension to the quark model, introduced by Murray Gell-Mann [4], which related the known hadrons to one another. Today, two additional quarks are known: top (t) and bottom (b).
The interactions of elementary particles, like quarks, are governed by the Standard Model (SM) of Particle Physics. The SM is one of the most precisely tested theories ever conceived, and the existence of six quarks unequivocally contributed to its success. Despite this, the SM is faced with challenges; aside from the lack of a theoretical framework for gravitational effects, there are still open questions on the origin of the matter-antimatter imbalance in the universe, and among others, the nature of dark matter and dark energy. Similarly, and from a phenomenological standpoint, the quark model has proven to be a very successful framework for understanding the structure of many observed hadrons. Hadrons composed of two quarks are called mesons, and those composed of three quarks are called baryons. The ground states of baryons composed of u, d or s quarks and those containing one heavy quark (either c or b) have been observed. Only one of three predicted doubly charmed baryons has been observed, as reported by the LHCb experiment [5]. The quantum numbers associated with many of these ground states have not been measured [6], and much of the excited spectrum of baryons, especially of those containing heavy quarks, remains an resolved mystery. Since the start of the millennium, the unexpected observation of XYZ states (charm-like mesons) and tetra-/penta-quarks (hadron-like structures composed of four/five quarks), has prompted numerous new explanations. These new models go beyond mere extensions of the quark model and reveal the potential for a plethora of new states [6, 7].
A step towards addressing some of these mysteries is a precise determination of the ground-state baryons. Baryons containing a heavy quark, like charmed baryons, are especially interesting, both theoretically and experimentally. Theoretically, they offer an environment where a three body problem is essentially reduced to a two body problem, as the charm quark induces a potential which is sufficiently strong for this treatment. These type of baryons offer an interesting scenario where the non-perturbative regime of Quantum Chromodynamics (QCD) crosses over to a perturbative regime. Experimentally, some of these charmed baryons decay weakly and can thus be studied in a controlled environment with high precision. By combining mesons and photons with these baryons, the higher excitations can be reached and their properties precisely assessed.

1.1. Focus and Outline

In this thesis, we study the ground state charmed baryons Λ_c^+, Ξ_c^0 and Ξ_c^+ in the modes:

$$\Lambda_c^+ \to pK^-\pi^+, \tag{1.1}$$
$$\Xi_c^0 \to \Lambda^0 K^-\pi^+, \tag{1.2}$$
$$\Xi_c^0 \to \Xi^-\pi^+, \tag{1.3}$$
$$\Xi_c^+ \to \Lambda^0 K^-\pi^+\pi^+, \tag{1.4}$$
$$\Xi_c^+ \to \Xi^-\pi^+\pi^+. \tag{1.5}$$

In Chapter 2, we introduce the theory underpinning charmed baryons and discuss the symmetrical structures that relate them to one another. In Chapter 3, we introduce the particle collider, SuperKEKB, and the detector, Belle II, which provide the data used in our analysis. In Chapter 4, we give an overview of the various methods and tools involved in the discrimination of events from data collected by the Belle II detector. In Chapter 5, we delve into our first mode reconstruction, $\Lambda_c^+ \to pK^-\pi^+$, and discuss in detail the various steps taken to maximize the signal significance of this mode. Here, we also discuss the agreement between simulation and data. In Chapter 6, we outline the reconstruction of the various decays of Ξ_c, Eq. (1.2) through Eq. (1.5). At the heart of the thesis is the measurement of the ratio branching fractions

$$\frac{\mathcal{B}(\Xi_c^0 \to \Lambda K^-\pi^+)}{\mathcal{B}(\Xi_c^0 \to \Xi^-\pi^+)} \tag{1.6}$$

and

$$\frac{\mathcal{B}(\Xi_c^+ \to \Lambda K^-\pi^+\pi^+)}{\mathcal{B}(\Xi_c^+ \to \Xi^-\pi^+\pi^+)}, \tag{1.7}$$

which we present at the end of the chapter. Lastly, in Chapter 7, we conclude with a summary and an outlook on charmed baryons.

2. Charmed Baryons in the Standard Model of Particle Physics

In this chapter, we elaborate on the theoretical concepts that underpin the phenomenology of charmed baryons. In Sec. 2.1, we begin by introducing the standard model of particle physics, briefly discussing the symmetries that give rise to particle interactions in the theory. In Sec. 2.2, we introduce the Cabibbo-Kobayashi-Maskawa (CKM) matrix, which illustrates the mechanism by which quarks undergo weak decays. Delving deeper into symmetries, in Sec. 2.3, we present the Quark Model, which categorizes combinations of quarks into groups of hadrons with discrete quantum properties. In Sec. 2.4, we conclude with a discussion of the quark model predictions in relation to the observed mass spectrum of the charmed baryons, Λ_c and Ξ_c.

2.1. Standard Model of Particle Physics

The standard model of particle physics, or simply SM, is based on the symmetry structure [8–10]

$$SU(3)_c \otimes SU(2)_{\mathrm{L}} \otimes U(1)_Y . \tag{2.1}$$

These symmetries are based on the framework of Lie groups, within which particle interactions are expressed in terms of a local gauge-invariant Lagrangian density [9, p. 461].[1] The Lagrangian formalism provides a relativistic treatment of fields with spin-0 (scalar bosons), spin-$\frac{1}{2}$ (fermions), and spin-1 (vector bosons). For an interaction involving fermions, where the fermion is represented by the Dirac spinor[2] $\boldsymbol{\Psi}$, the gauge-invariant kinetic terms of the Lagrangian can be expressed as

$$\overline{\Psi}_\alpha \left(i\gamma^\mu D_\mu\right)_{\alpha\beta} \Psi_\beta , \tag{2.2}$$

where γ^μ are the Dirac γ-matrices [9, p. 91] and D_μ is the covariant derivative containing the gauge fields involved in the interaction, [11, 12]

$$D_\mu = \partial_\mu + \underbrace{ig\frac{\tau^b}{2}W^b_\mu}_{SU(2)_L} + \underbrace{ig'YB_\mu}_{U(1)_Y} + \underbrace{ig_s G^a_\mu T^a}_{SU(3)_c} , \quad b = 1,2,3 , \quad a = 1,\ldots,8 . \tag{2.3}$$

The individual terms of this equation, along with the meaning of the indices α and β, are elaborated next.

[1] Local gauge invariance implies that the physics remain unchanged under covariant transformations of the Lagrangian density. The covariant derivative is discussed in the main text.

[2] A four-component wave function.

$\mathbf{SU(3)_c}$ denotes the symmetry group of Quantum Chromodynamics (QCD) which describes how quark fields of different flavors (u, c, t, d, s, b) shape into hadrons through an underlying symmetry of *color* exchanges (r: red, g: green, b: blue). The generators of the $SU(3)_c$ group, T^a with $a = 1, ..., 8$, can be represented using the Gell-Mann matrices, which are 3×3 matrices that obey the Lie algebra $[T^a, T^b] = i f_{abc} T^c$, where f_{abc} is the structure constant of the group. Due to the non-abelian nature of this group, a local gauge transformation—requiring the conservation of color charges (r, g, b)— gives rise to 8 *self-interacting* gauge fields G^a_μ, $a = 1, 2, 3, \ldots, 8$. These fields are called gluons, and they couple to quarks with the coupling strength g_s. In QCD, quarks carry color charge, thus α and β of Eq. (2.2) represent the color charge.
Given that only color singlets are observed in nature, hadrons themselves are confined to color singlets; this is discussed in more detail in Sec. 2.3.

$\mathbf{SU(2)_L \otimes U(1)_Y}$ represents the unification of Quantum Electrodynamics (QED) with Weak interactions, hence electroweak unification—It is often referred to as the Glashow-Salam-Weinberg (GSW) model, whose named contributors were awarded the Nobel prize in 1979 [13]. Specifically, the GSW model sets *a priori* left-handed (L) fermions as doublets and right-handed (R) fermions as singlets. Thus α and β of Eq. (2.2) represent the handedness of the fermion. The generators of $SU(2)_L$, τ^b with $b = 1, 2, 3$, can be represented using the 2×2 Pauli matrices. In the case of $U(1)_Y$, the local gauge transformation leads to the conserved charge Y, referred to as the weak hypercharge. The gauge fields W^b_μ, with $b = 1, 2, 3$, of $SU(2)_\mathrm{L}$ couple (with strength g) to left-handed particles, whereas the gauge field B_μ of $U(1)_Y$ couples (with strength g') to both—left and right—handed particles.
The physical fields A_μ and Z_μ can be expressed as a linear combination of the GSW fields,

$$\begin{pmatrix} Z_\mu \\ A_\mu \end{pmatrix} = \begin{pmatrix} \cos(\theta_W) & -\sin(\theta_W) \\ \sin(\theta_W) & \cos(\theta_W) \end{pmatrix} \begin{pmatrix} W^3_\mu \\ B_\mu \end{pmatrix}, \quad \text{with} \quad \tan\theta_W = \frac{g'}{g}, \tag{2.4}$$

where θ_W is known as the weak mixing angle [9, p. 419]. A natural definition for the remaining gauge fields, W^1_μ and W^2_μ after symmetry breaking, is in terms of the physical ladder-like operator fields,

$$W^\pm_\mu \equiv \frac{1}{\sqrt{2}} \left(W^1_\mu \mp i W^2_\mu \right) . \tag{2.5}$$

A summary of the particles and interactions involved in the SM is shown in Fig. 2.1.

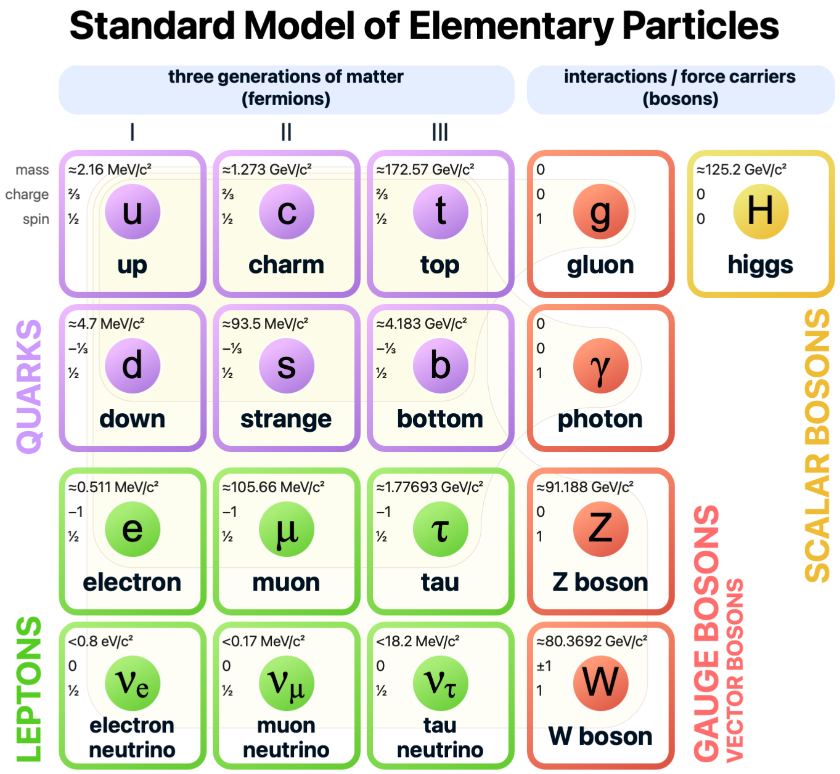

Figure 2.1.: Summary of the fermions and bosons involved in the SM. The fermions contain the quarks and leptons, all of which have spin $s = 1/2$. The vector bosons ($s = 1$) represent the force carriers of QCD (gluon), QED (photon), and weak interactions (Z and $W^{\pm}$ bosons). The Higgs boson (H) is also listed, which is a scalar boson ($s = 0$) responsible for providing mass to the particles involved in electroweak interactions. Note that the SM also accounts for the antiparticle partners of each fermion. Illustration adapted from [14].

2.2. Cabibbo-Kobayashi-Maskawa Matrix

The Cabbibo-Kobayashi-Maskawa (CKM) matrix [15], V_{CKM}, is a unitary matrix that characterizes the coupling magnitude for charged flavor-changing processes in the quark-sector of the Standard Model. It corresponds to an SU(3) generalisation of the Cabbibo-Mechanism[3] by extending it to three families of quarks (family 1: u, d, family 2: c, s, family 3: t, b). The CKM matrix can be expressed using 4 independent parameters, e.g., with the Wolfenstein parametrization one obtains a $\mathcal{CP}$-violating phase and three mixing angles [6, 9]. Thus, the CKM matrix presents a theoretical and experimental milestone [18] in our understanding of quark interactions within the framework of the Standard Model. The weak-eigenstate quarks can be written as a superposition of mass-eigenstate quarks, such that when a pair of quarks interact via the exchange of a weak vector boson $W^{\pm}$, the interaction lagrangian takes the form: [6]

$$-\frac{g}{\sqrt{2}}(\overline{u_L}, \overline{c_L}, \overline{t_L})\gamma^{\mu}W_{\mu}^{+}\underbrace{\begin{pmatrix} V_{ud} & V_{us} & V_{ub} \\ V_{cd} & V_{cs} & V_{cb} \\ V_{td} & V_{ts} & V_{tb} \end{pmatrix}}_{V_{\text{CKM}}}\begin{pmatrix} d_L \\ s_L \\ b_L \end{pmatrix} + \text{h.c.}\,, \tag{2.6}$$

where the GSW model condition for $W^{\pm}$—that only left-handed quarks are involved—is written explicitly.

Eq. (2.6) indicates that a weak interaction through the exchange of a $W^{\pm}$ vector boson can induce flavor change that spans across all the three families of quarks. At tree-level (no loops), the quark flavor change must be charged, i.e., down type quarks (d, s, b) with charge $Q = -1/3$ transition into up-type quarks (u, c, t) with charge $Q = 2/3$, and vice versa. From experimental observations, it is known that the CKM matrix expresses an almost diagonal form, [6]

$$|V_{\text{CKM}}| \approx \begin{pmatrix} 0.974 & 0.225 & 0.004 \\ 0.225 & 0.973 & 0.042 \\ 0.009 & 0.041 & 0.999 \end{pmatrix}. \tag{2.7}$$

Therefore, transitions within the same quark family are preferred, and transitions such as $b \to u$ are less favored than $b \to c$.

[3] In 1963, Nicola Cabibbo [16] hypothesized universal weak-eigenstate couplings for light quarks (u,d,s) via a mixing angle $\theta_c \approx 13°$. It was later in 1970 recognized that such a universal weak coupling serves well for demanding the existence of a fourth quark (charm) via the SU(2) GIM mechanism [17], [9, p. 367]. In 1973, the CKM quark-mixing matrix provided a generalization of these ideas to SU(3) which gave rise to an explanation for CP violation in the quark-sector [15].

2.3. Quark Model

In QCD, hadrons are described as *colorless* bound states of flavored quarks. A quark q may take on any of the following flavors: u, d, c, s, t, b. The word "colorless" points to the idea that only color singlets are observed in nature. Given that quarks carry color charge, a colorless state is reached when at least two quarks (quark and antiquark) of complementary color charge bind together, e.g., $r\bar{r}, g\bar{g}, b\bar{b}$. A colorless state formed by three quarks involves the complete color combination rgb. Naturally, combinations of colorless states are also colorless. The quark model classifies the bound states composed of two quarks as mesons, which are bosons (spin-0), while bound states composed of three quarks are classified as baryons, which are fermions (spin-$\frac{1}{2}$). Colorless states composed of four or more quarks fall under the category of exotic hadrons. [6]

The quark model's primary purpose is to illustrate the flavor symmetries associated with the observed spectrum of mesons and baryons. Notably, QCD was developed only after the quark model had been introduced, it therefore lifted some of the seeming paradoxes that arose from the treatment of hadrons without color confinement [7].

Given the significant role of baryons in this thesis, we will focus on the flavor symmetries associated with bound states composed of three quarks.

2.3.1. Quantum Numbers of Flavor

Let us first consider an $SU(3)$ group where a baryon involves the three flavors u, d and s. The eight generators of $SU(3)$ can be represented using the Gell-Mann matrices (see Appendix A). The eigenvalues of the two simultaneously diagonalisable matrices are referred to as the third component of isospin I_3 and the hypercharge Y. These are quantum numbers where I_3 is $+1/2$ for u-quarks, $-1/2$ for d-quarks, and 0 for the other quarks. The hypercharge Y in this group relates to the quantum number that encodes the strangeness (S) by the identity

$$Y = \mathcal{B} + S. \tag{2.8}$$

$\mathcal{B}$ represents here the baryon number, defined as $\mathcal{B} = 1$ for a baryon and $\mathcal{B} = -1$ for an anti-baryon. In terms of *constituent* quarks[4], each quark that constitutes a baryon has $\mathcal{B} = 1/3$ and each antiquark has $\mathcal{B} = -1/3$.

Generally, when involving all the quark flavors, the hypercharge Y relates to other complementary quantum numbers such as the charmness (C), the bottomness (B) and topness (T), giving the expression: [6]

$$Y = \mathcal{B} + S + \frac{1}{3}(B - C - T). \tag{2.9}$$

In table 2.1, the quantum numbers corresponding to each quark flavor are summarized.

[4]The constituent quarks of a baryon also take on "constituent masses". As opposed to current masses, which are as low as a few MeV, the constituent mass is understood as the effective mass of a valence quark in a baryon. Their mass is attributed to the exchange of gluons, in other words, the quarks are confined in a gluon exchange potential.

	d	u	s	c	b	t
I_3	$-1/2$	$+1/2$	0	0	0	0
Y	$1/3$	$1/3$	$-2/3$	0	0	0
S	0	0	-1	0	0	0
C	0	0	0	1	0	0
B	0	0	0	0	-1	0
T	0	0	0	0	0	1

Table 2.1.: The flavor quantum numbers of constituent quarks. The antiparticles have opposite flavor sign.

Note that a charge Q (in units of the electron charge) is related to the quantum numbers by the Gell-Mann-Nishijima formula [6],

$$Q = I_3 + \frac{1}{2}(\mathcal{B} + S + C + B + T). \tag{2.10}$$

2.3.2. $SU(3)$ Flavor Symmetry

We continue our discussion of an $SU(3)$ flavor symmetry which involves three flavors (e.g., u, d, s). Each of the three quarks in the baryon can take on any of the three different flavors, such that their combinations are represented as $3 \otimes 3 \otimes 3$. This tensor product can be decomposed into irreducible representations—that form *multiplets*—using the Young tableaux formalism [19].
The fundamental representation 3 in $SU(3)$ is then a unit box ($\square$), such that the tensor product $3 \otimes 3 \otimes 3$ in $SU(3)$ is visualized as:

$$\square \otimes \square \otimes \square = \left(\underbrace{\ydiagram{2}}_{6_\mathrm{S}} \oplus \underbrace{\ydiagram{1,1}}_{\bar{3}_\mathrm{A}}\right) \otimes \ydiagram{1} = \underbrace{\ydiagram{3}}_{10_\mathrm{S}} \oplus \underbrace{\ydiagram{2,1}}_{8_\mathrm{M}} \oplus \underbrace{\ydiagram{2,1}}_{8_\mathrm{M}} \oplus \underbrace{\ydiagram{1,1,1}}_{1_\mathrm{A}} \tag{2.11}$$

where the underbracing number is the multiplet dimension and its subscript stands for S : symmetric, A : antisymmetric, and M : mixed-symmetry, under the exchange of any two quarks. For the decomposition into multiplet groups we therefore have $3 \otimes 3 \otimes 3 = 10_\mathrm{S} \oplus 8_\mathrm{M} \oplus 8_\mathrm{M} \oplus 1_\mathrm{A}$, i.e., a decuplet, two octets and a singlet.
Note that if we were to replace the quark flavors by color charge (r, g, b), the color singlet would evidently be antisymmetric.

Baryon Wave Function

The baryon wave function accounting for color, space, spin and flavor, reads [9]

$$\Psi(\text{baryon}) = \psi_{\text{color}}\psi_{\text{space}}\psi_{\text{spin}}\psi_{\text{flavor}}. \tag{2.12}$$

As a fermion, the total wave function $\Psi(\text{baryon})$ must be antisymmetric. The spin can be decomposed in $SU(2)$, because each quark can be represented by spin $+1/2$ and spin $-1/2$, such that $2 \otimes 2 \otimes 2 = 4_{\text{S}} \oplus 2_{\text{M}} \oplus 2_{\text{M}}$. For a spatially symmetric function, i.e., the ground state of the baryon where the orbital angular momentum $L = 0$ (between the constituent quarks), the total wave function can only be antisymmetric if the combination $\psi_{\text{spin}}\psi_{\text{flavor}}$ is symmetric.
This means that for a baryon involving three flavors, the decuplet in Eq. (2.11) must be combined with the quadruplet of spin, i.e., it must be represented with spin 3/2. In the case of the octets, the mixed-symmetries can be combined with the mixed-symmetry of the spin doublets to make $\psi_{\text{spin}}\psi_{\text{flavor}}$ symmetric, where the corresponding spin is 1/2.

Light Baryon Multiplets

Baryon states are usually labeled by their spin-parity J^P, where P stands for the parity (reflection in space $x \to -x$) with $P = (-1)^L$ and J is the total angular momentum $J = L+S$, with S signifying here the spin state of the baryon. Thus, for an orbital angular momentum $L = 0$, $J \equiv S$.
For the light baryons (composed of u, d and s), we show in Fig. 2.2(a) the $J^P = 3/2^+$ decuplet and in Fig. 2.2(b) the $J^P = 1/2^+$ octet, structured in accordance with their flavor quantum numbers. In the ground-state octet, we find the proton (p) and the neutron (n), which are often simply referred to as nucleons (N). In the ground-state decuplet, the designation for these baryons—composed of u and d quarks—changes to Δ. In general, baryons that contain at least one strange quark are referred to as hyperons: Λ and Σ with one strange quark, Ξ with 2 strange quarks, and Ω with 3 strange quarks. To differentiate them from the octet, a star ($*$) is appended to the hyperon naming scheme in the decuplet.

Mass Allocations / The Known Light Baryons

Baryons of a multiplet with the same J^P assignment are expected to have very similar properties. However, it is important to note that these symmetries are slightly broken due to the presence of the s-quark, which is heavier than the u and d quarks. Nevertheless, the approximate symmetry holds, and in fact, all of these ground-state baryons are *known*, i.e., their existence is certain [6][5].
The first observations of the hyperons Λ, Σ, Ξ dates back to the 1950's, followed by the discovery of Ω in 1964. The Ω hyperon was in fact a quark model prediction made by Gell-Mann two years before its discovery [7, 20, 21]. Leading to this prediction is the consideration of the symmetry in the measured masses of baryons allocated to a multiplet: For the decuplet, one can express a mass difference that correspond to the strange quark

[5] The Particle Data Group (PDG) assigns 4 stars to states that are marked as known in their summary tables.

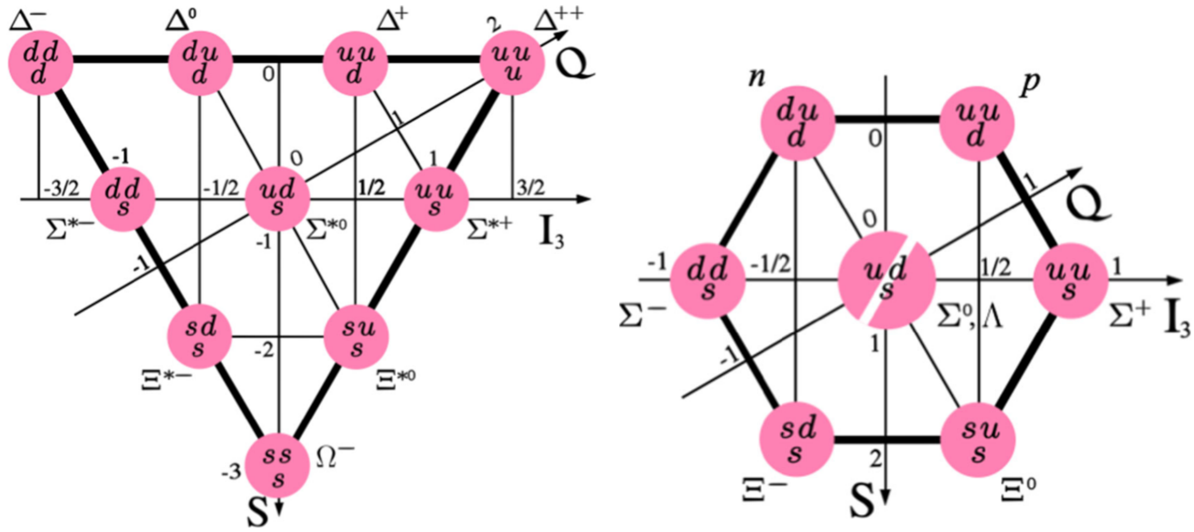

(a) (b)

Figure 2.2.: Multiplets from the $SU(3)$ flavor symmetry of baryons containing u, d and s quarks. In (a), the $J^P = 3/2^+$ decuplet. In (b), the $J^P = 1/2^+$ octet. Illustration adapted from [7] CC BY 4.0.

$SU(3)$ flavor multiplet	J^P	designation and mass association [MeV]			
8	$1/2^+$	$N(939)$	$\Lambda(1116)$	$\Sigma(1193)$	$\Xi(1318)$
10	$3/2^+$	$\Delta(1232)$	$\Sigma^*(1385)$	$\Xi^*(1530)$	$\Omega(1672)$

Table 2.2.: The known ground-state baryons of $SU(3)$ flavor symmetry.

mass ($\sim 150\,\mathrm{MeV}$), [7, 20]

$$M_{\Sigma^*} - M_\Delta = M_{\Xi^*} - M_{\Sigma^*} = M_\Omega - M_{\Xi^*}, \tag{2.13}$$

and similarly, for the octet, the mass relation

$$(M_N + M_\Xi)/2 = (3M_\Lambda + M_\Sigma)/4 \tag{2.14}$$

holds.
In table 2.2, we summarize the known ground-state baryons, where the number in parenthesis denotes their assigned approximate mass (by convention in MeV).

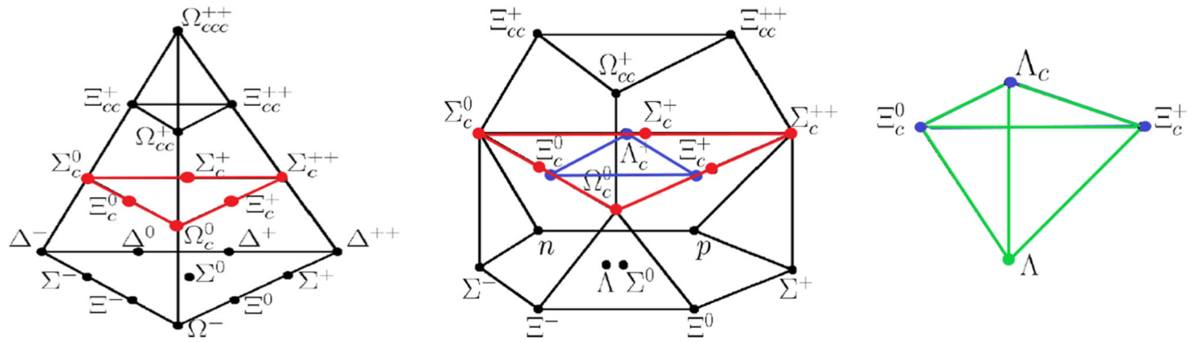

Figure 2.3.: Multiplets from the $SU(4)$ flavor symmetry of baryons containing u, d, s and c quarks. Left: The 20_{S}-plet with $J^P = 3/2^+$. Middle: The 20_{M}-plet with $J^P = 1/2^+$. Right: The 4_{A}-plet with $J^P = 1/2^-$. Note that the 4_{A}-plet is only shown for completeness; baryons would be required to have negative parity (orbital excitations) to be allocated to this multiplet. Illustration adapted from [7] CC BY 4.0.

2.3.3. $SU(4)$ Flavor Symmetry

We can extend the concepts discussed in Sec. 2.3.2 to four flavors: u, d, s and c. In this case, we have

$$4 \otimes 4 \otimes 4 = 20_{\mathrm{S}} \oplus 20_{\mathrm{M}} \oplus 20_{\mathrm{M}} \oplus 4_{\mathrm{A}}. \tag{2.15}$$

Naturally, this $SU(4)$ flavor symmetry already contains the previously introduced $SU(3)$ symmetry. The only difference is that we now account for charmness as an additional flavor structure.

As before, for $L = 0$, we require that $\psi_{\mathrm{spin}}\psi_{\mathrm{flavor}}$ be symmetric. Therefore, the baryons corresponding to 20_{S} have $J^P = 3/2^+$ and the baryons in 20_{M} have $J^P = 1/2^+$. These multiplets are shown in Fig. 2.3, where the naming scheme is borrowed from the light baryons by appending a subscript that indicates the c-quark content. The level increases (from bottom to top) according to the number of charm quarks contained in the baryons: the ground level contains light (uncharmed) baryons, the first level above the ground level contains singly charmed baryons, etc. Note that the ground level of each respective multiplet contains the $SU(3)$ decuplet (with $J^P = 3/2^+$) and the $SU(3)$ octet (with $J^P = 1/2^-$).

As illustrated in Fig. 2.1, the charm quark is much heavier than the light quarks (u, d, s). These symmetries are therefore heavily broken. However, many of these states have been measured. As of 2024, the baryon summary tables, produced by the Particle Data Group (PDG) [6], list 28 singly charmed baryons (including excitations), where 10 of these states have not yet received a quark model J^P assignment. Only one doubly charmed baryon has been *seen*[6], the Ξ_{cc}^{++}, without J^P assignment. Of the 28 singly charmed baryons, only the $J^P = 1/2^+$ ground states Λ_c, $\Sigma_c(2455)$ and Ξ_c^0 are considered known (where the J^P values have *actually* been measured), the others have simply been seen.

[6] These are states where the existence is likely to certain, given 3 stars in the PDG summary tables [6].

2.4. Singly Charmed Baryons of the $J^P = 1/2^+$ $\overline{3}_\mathrm{A}$-plet

Of particular relevance to this thesis are the singly charmed baryons located at the corners of the blue triangle within the middle level of the $J^P = 1/2^+$ 20_M-plet in Fig. 2.3: Λ_c^+ and $\Xi_c^{0,+}$. Their flavor wave functions can be expressed as: [20]

$$\Lambda_c^+ = \frac{1}{\sqrt{2}}(ud - du)c\,, \tag{2.16}$$

$$\Xi_c^+ = \frac{1}{\sqrt{2}}(us - su)c\,, \tag{2.17}$$

$$\Xi_c^0 = \frac{1}{\sqrt{2}}(ds - sd)c\,. \tag{2.18}$$

These charmed baryons are part of an antisymmetric $\overline{3}$ (anti-triplet) within the $SU(3)$ subgroup of the $SU(4)$ 20_M-plet. The motivation behind this $SU(3)$ subgroup decomposition is elaborated next.

Quark-diquark System

The study of the properties of baryons which contain a heavy quark—in this case a charm quark accompanied by two light quarks—becomes more tractable if the baryon is treated as a reduced 3-body system. We use Fig. 2.4 to illustrate this argument. The light quarks, represented by $q_1 = q_2 = q$, are treated together as *diquark* oscillators with reduced mass, $m_\rho = m_q$, where ρ represents the separation of the light quarks as a function of their positions,

$$\vec{\rho} = (\vec{r}_1 - \vec{r}_2)/\sqrt{2}. \tag{2.19}$$

The reduced mass from the interplay between the heavy quark (Q) and the diquark is then given by $m_\lambda = 3m_q m_Q/(2m_q + m_Q)$, where

$$\vec{\lambda} = (\vec{r}_1 + \vec{r}_2 - 2\vec{r}_3). \tag{2.20}$$

Therefore, if the angular momentum of each subsystem is denoted by l_ρ and l_λ, respectively, then $L = l_\rho + l_\lambda$. Naturally, this points to the idea that baryon excitations can be described by orbital excitations of ρ and λ. [7, 20, 21][7]

It is evident by this quark-diquark construction that the middle level of the 20_M-plet in Fig. 2.3 should ideally be decomposed in a 2-quark $SU(3)$ flavor symmetry that couples to the charm quark flavor. As we saw in Eq. (2.11), for two quarks, each with 3 flavors to choose from, we have $3 \otimes 3 = 6_\mathrm{S} \oplus \overline{3}_\mathrm{A}$. The 6_S-plet implies a flavor symmetric diquark (i.e., a flavor-symmetric ρ system), and because it corresponds to baryons allocated within a mixed-symmetric 20-plet, the charm-diquark (i.e., the λ system) flavor must be antisymmetric. Similarly, the $\overline{3}_\mathrm{A}$-plet implies a flavor antisymmetric diquark, requiring a flavor symmetric charm-diquark system. [7]

[7] This approach is also applied to the study of the light baryons, but in that case, the mixing of the ρ and λ configurations is more prevalent than in baryons with one heavy quark (c or b).

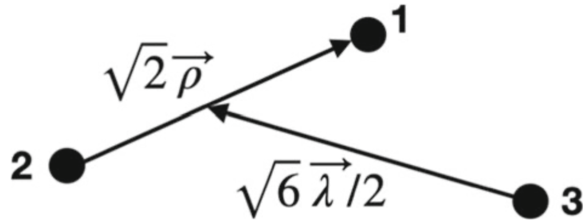

Figure 2.4.: Schematic of a quark-diquark system using Jacobi coordinates. The light quarks are signified by the filled circles, "1" and "2", and the heavy quark is signified by the filled circle "3". Illustration adapted from [7] CC BY 4.0.

Mass Spectrum

The $\overline{3}_{\mathrm{A}}$-plet singly charmed baryons, Λ_c^+ and $\Xi_c^{+,0}$, decay weakly[8], while the other $SU(4)$ ground-state singly charmed baryons (except for the Ω_c^0) decay strongly or electromagnetically [20]. Fig. 2.5 shows the mass spectrum of the singly charmed baryons with allocated J^P.

Notably, the $J^P = 1/2^+$ charmed baryons are the lowest lying states. As their mass increases, the J^P and multiplet association of the baryons also changes. The higher energy levels are attributed to orbital excitations, where the level is furthermore split due to the spin-spin interactions of the ρ (diquark) and λ (charm-diquark) modes [7, 20].[9]

The lowest lying states for Λ_c^+ and $\Xi_c^{+,0}$ correspond to the weakly decaying members of the $\overline{3}_{\mathrm{A}}$-plet. Thus far, the highest reported mass for Λ_c is the $J^P = 3/2^-$ $\Lambda_c(2940)$ which sits at 653 MeV above the ground-state Λ_c. For Ξ_c, the highest plotted excitation in Fig. 2.5 is the $J^P = 3/2^-$ $\Xi_c(2815)$, however the PDG now also reports a higher mass state, the $J^P = 1/2^+$ $\Xi_c(2970)$, first measured by Belle [22]. In practice, excitations are identified by their emission of photons, pions (mesons with u and d quarks) and kaons (mesons with u, d and s quarks), as they reach a lower state.

Evidently, many expected states have not been measured, and the limitations of the quark model are yet to be well understood. A precise determination of the properties of the weakly decaying ground-state baryons, Λ_c^+ and $\Xi_c^{+,0}$, is thus crucial for a clear understanding of the excited spectrum.

[8]The charm quark undergoes a flavor change, e.g., $c \to s$.

[9]This is analogous to the hyperfine splitting seen in the Hydrogen atom, where the spin of the proton couples to the spin of the electron depending on its spin orientation.

A similar spectrum is seen for the *beauty* baryons, where the charm quark in the singly charmed baryon is replaced by the much heavier bottom quark. However, the mass splittings get smaller as the heavy quark gets heavier. The opposite effect is seen for the hyperons, where due to the lighter mass of the strange quark, the mass splittings are large. [7, 20]

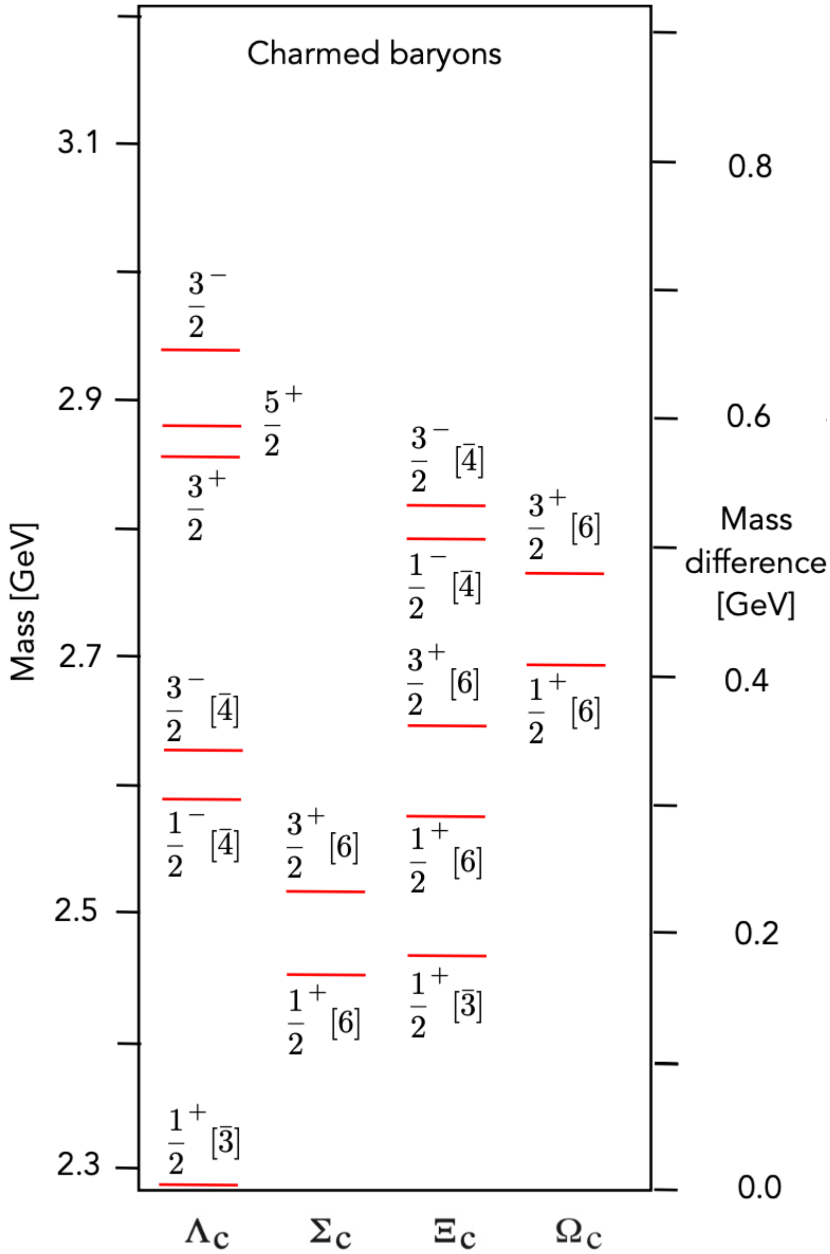

Figure 2.5.: Level scheme for singly charmed baryons with J^P assignment. The numbers in brackets indicate the associated multiplet (if identified). The mass difference is in reference to the lowest lying state, Λ_c^+. Illustration adapted from [6].

3. SuperKEKB and the Belle II Detector

In this chapter, we introduce the experimental setup, which consists of the SuperKEKB collider and the Belle II detector. The SuperKEKB collider and the Belle II detector have been in joint operation since 2019. They present a variety of upgrades and design improvements over their predecessors, the KEKB accelerator [23] and the Belle detector [24], which operated from 1999 to 2010.
We begin by briefly mentioning some of the characteristics of the SuperKEKB collider. Thereafter, we examine the Belle II detector and its components along with the methods used for the identification of different particle types. We conclude the chapter by discussing the collection of data and the simulation of physics events.
The information provided in this chapter is substantially based on the SuperKEKB Collider publication [25], the Belle II technical design report [26], and the Belle II physics book [27].

3.1. The SuperKEKB Collider

SuperKEKB is an asymmetric-energy electron-positron double-ring collider located in Tsukuba, Japan. It has a single interaction region (IR) which is located at the center of the Belle II detector. Collision events are typically produced at a center-of-mass energy of 10.58 GeV. This energy facilitates the production of $B\overline{B}$ events which are threshold products of a $b\overline{b}$ bound-state resonance referred to as $\Upsilon(4S)$, see Fig. 3.1 for an overview. For this reason, SuperKEKB is often categorized as a B-factory. However, together with the data-taking capabilities of the Belle II detector, superKEKB is also used for producing a broader spectrum of center-of-mass collisions, ranging from 9.4 GeV to 11 GeV. Thus, SuperKEKB can be used to scan the entire bottomonium spectrum.
In this thesis, we are interested in events from collisions at near the $\Upsilon(4S)$ rest energy, thus our discussion of the collider is grounded on the operation at this energy.

3.1.1. Collider Design

A depiction of the SuperKEKB collider is given in Fig. 3.2. The circumference of each storage ring, one for 7 GeV electron beams and one for 4 GeV positron beams, spans a distance of approximately 3 km. Before entering the storage rings, electrons are injected into a linear accelerator (linac) and accelerated to an energy of 7 GeV with a bunch charge of 4 nC (2 bunches). On the other hand, positrons are created from the interaction of injected electrons with a Tungsten material target found half-way in the linac; the created positrons are then deflected using a magnetic field into a 1.1 GeV positron damping ring

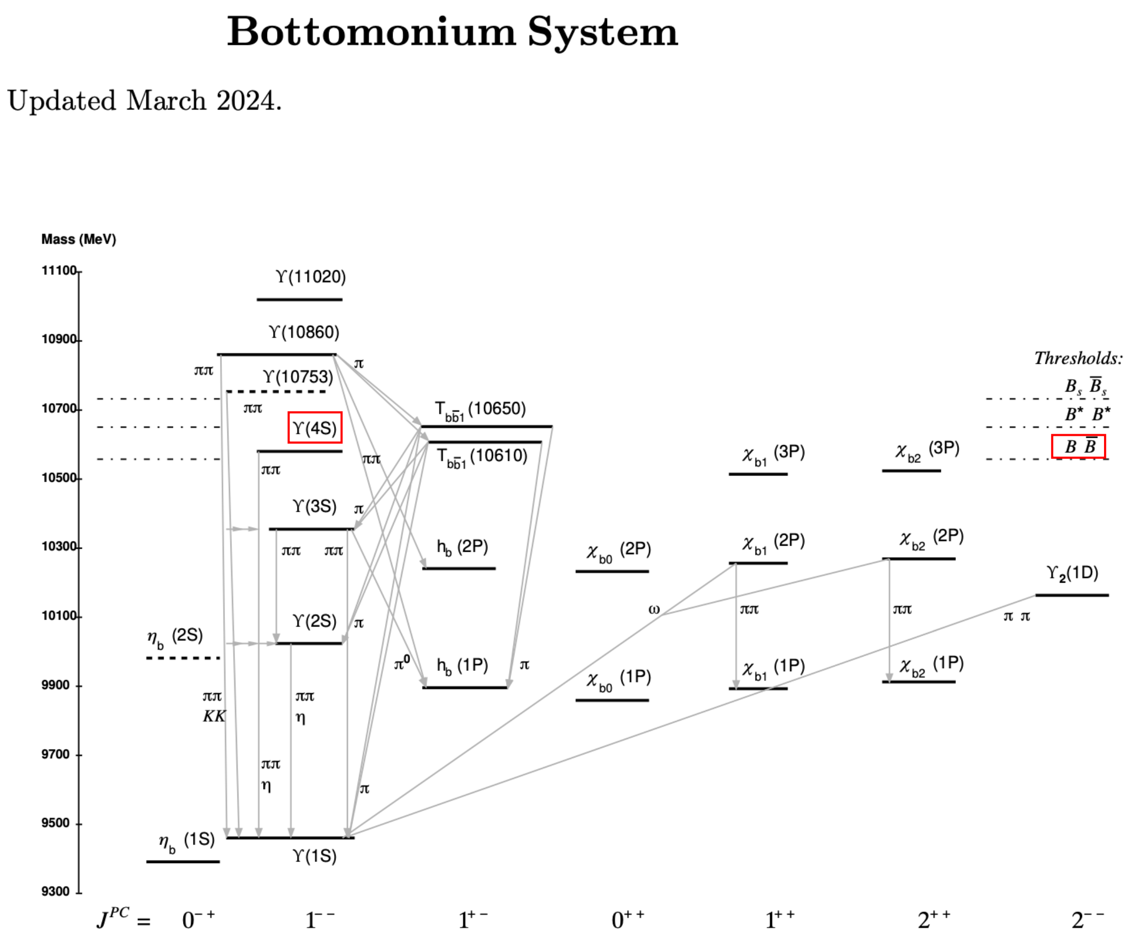

Figure 3.1.: This level scheme from [6, p. 2023] portrays the bound states of $b\overline{b}$ which form the bottomonium system. Particularly for electron-positron collision experiments, the quantum numbers for these $b\overline{b}$ resonances lie in the $\Upsilon(nS)$ column with $J^{PC} = 1^{--}$ (the charge conjugation C is defined for bound states of two quarks with opposing charge, here $C = -1$). As seen by the threshold dash-dotted lines, the $\Upsilon(4S)$ resonance is found right above the energy of the open beauty pairs $B\overline{B}$.
Note that states shown with dashed lines need confirmation, i.e., $\Upsilon(10753)$ is not a confirmed state according to the PDG [6].

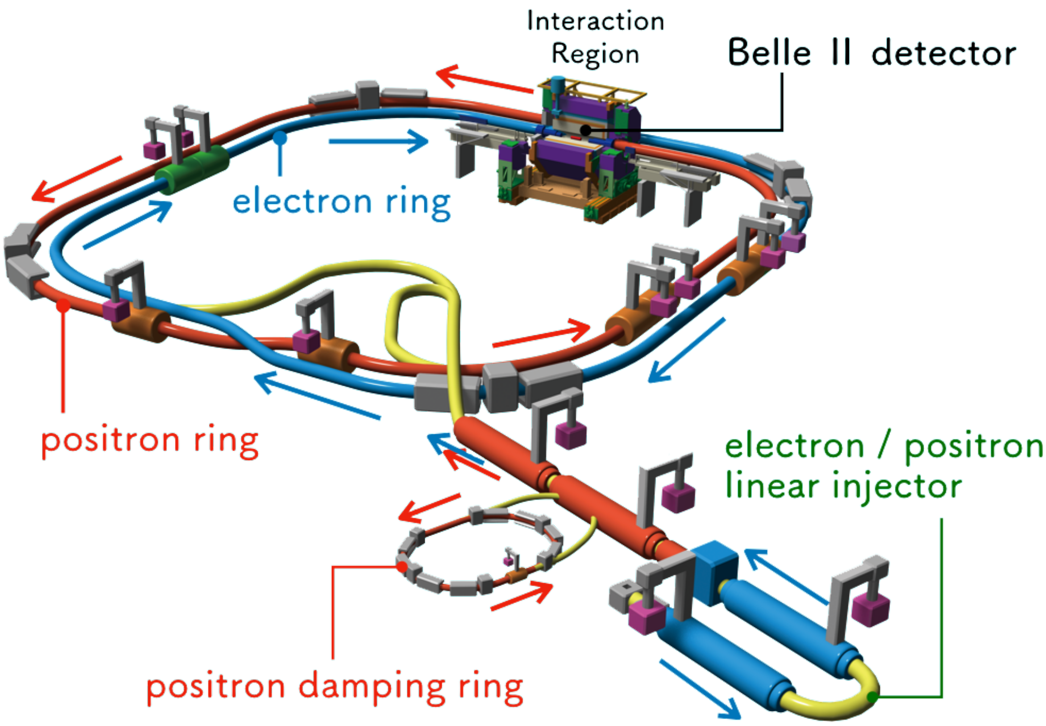

Figure 3.2.: Illustration of the SuperKEKB collider, ©KEK.

(DR) which reduces the emittance of the positron bunches. The DR positron bunches are then re-injected into the linear accelerator and accelerated to 4 GeV with a bunch charge of 4 nC (2 bunches). The storage rings can store up to 2500 bunches each, where each bunch contains about 9×10^{10} positrons (at a current of 3.6 A) and 6.5×10^{10} electrons (at a current of 2.6 A).[1] These beam currents are roughly twice as large as those of KEKB (e^+ beams of 1.64 A and e^- beams of 1.19 A) for the production of 10.58 GeV events.

A striking design feature of SuperKEKB is the employment of a *nanobeam* collision scheme. In this scheme, the high-current beams are tightly focused using additional quadrupole magnets located close to the interaction point (IP). The beams collide at a crossing angle of 2ϕ = 82 mrad (compared to 22 mrad at KEKB), see Fig. 3.3 for a schematic. Given the low emittance and dimensions of the colliding bunches, the vertical beta function at the IP, β_y^*, can be as low as 0.3 mm for both beams, which is about 20× smaller than that achieved at KEKB.

[1]See also [25, tab. 1].

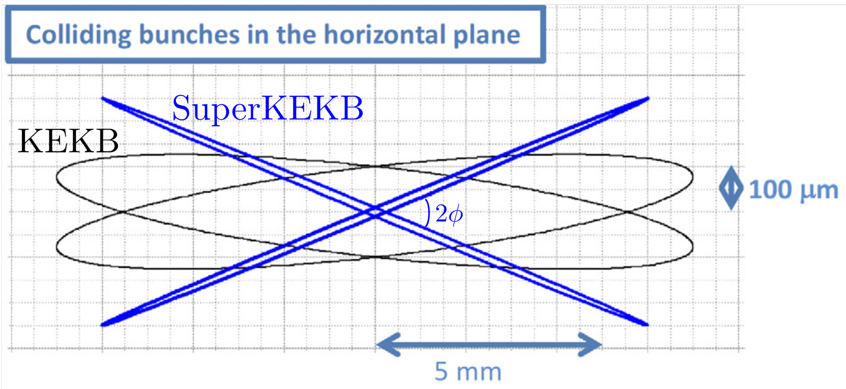

Figure 3.3.: Schematic of the nanobeam scheme [25] at SuperKEKB. The schematic represents a top view of the collider rings where the bunches cross. For comparison, drawn in black is the beam crossing at KEKB.

3.1.2. Luminosity Implications

The instantaneous luminosity $\mathcal{L}$ of a collider where bunches cross at an angle can be expressed as [28]

$$\mathcal{L} = \frac{N_+ N_- f N_b}{4\pi\sigma_x\sigma_y} S, \tag{3.1}$$

where $N_{+,-}$ are the number of particles in the colliding bunches, f is the frequency of the bunch collisions, N_b is the number of bunches, $\sigma_{x,y}$ are the horizontal and vertical beam sizes at the collision point, and S is a geometric loss factor due to the crossing angle. For ideal head-on collisions, $S = 1$.
In terms of the operation at SuperKEKB, we find that [25, 29]

$$\mathcal{L} \propto \frac{I_\pm \xi_{y\pm}}{\beta^*_{y\pm}} \tag{3.2}$$

where $\xi_{y\pm}$ is a beam-beam parameter which encodes the strength of the beam-beam interactions at the IP and $I_\pm$ is the current of the beams. The signs (+) and (−) stand for the positron and electron beams, respectively.
As discussed earlier, SuperKEKB can drive the beams up to twice the current I compared to KEKB, and under the nanobeam scheme, it could squeeze β^*_y down to 20× smaller. Keeping ξ_y the same for KEKB, this results in a rough estimate of 40× higher peak luminosity than achieved at KEKB.
In Fig. 3.4, we show the evolution of the peak luminosity at SuperKEKB over the past years. In the first run (RUN 1) from March 2019 until June 2022, SuperKEKB broke the previous KEKB record, 2.11×10^{34} cm^{-2} s^{-1}, setting a world record at $\mathcal{L} = 4.7 \times 10^{34}$ cm^{-2} s^{-1} (with $\beta^*_y \approx 1\,\mathrm{mm}$) in June, 2022.

Challenges

A successful operation of SuperKEKB at the intensity frontier is not without challenges. After a long shutdown (LS1) from June 2022 to January 2024, where subsequent maintenance and improvements to the accelerator and the Belle II detector took place, the

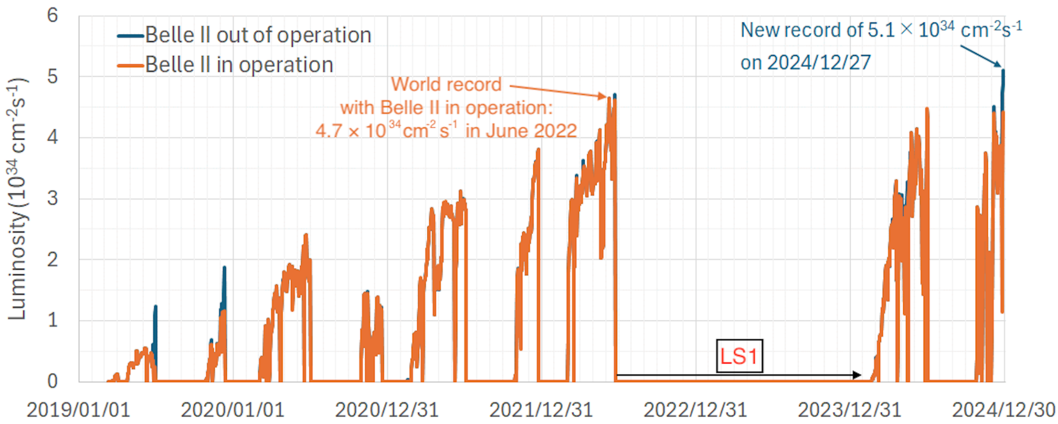

Figure 3.4.: Instantaneous luminosity evolution since the start of operation in 2019 [30].

full re-initiation of SuperKEKB was complicated by a 'sudden beam loss' (SBL). This led to the removal of some of the detector components to avoid damage. Much of 2024 was dedicated to addressing the SBL problem.

While the exact cause was not fully understood, removing dust accumulated from degraded vacuum sealing materials of the beam pipes significantly reduced beam losses. Under these cleaner conditions and before the winter break, SuperKEKB achieved yet another world record in peak luminosity, reaching 5.1×10^{34} cm^{-2} s^{-1}, see Fig. 3.4, albeit without the complete Belle II detector in place.

Projections elaborated in [31] indicate that SuperKEKB is expected to achieve a peak luminosity of 2×10^{35}cm^{-2}s^{-1} prior to any new additional upgrades. The target peak luminosity, 6×10^{35} cm^{-2} s^{-1}—which is a re-adjusted estimate of 30× higher than achieved at KEKB—is said to require further upgrades to the collider, especially near the IR. Upgrades to both the collider and the detector are under discussion, though they are expected to be implemented during the next long shutdown (LS2), by 2032.

3.1.3. Beam-induced Backgrounds

Interesting physics events are often overshadowed by numerous unwanted events. Particles that enter the vicinity of the detector due to intrinsic beam-control imperfections, vacuum impurities in the trajectory of the beams, or are not the desired products of the IP collisions, are referred to as background events.

With a higher luminosity at SuperKEKB compared to KEKB, comes a higher beam-induced background. The most substantial background sources at SuperKEKB are due to Touschek scattering, beam-gas scattering, synchrotron radiation, radiative Bhabha scattering, and two-photon processes.

Touschek Scattering

Touschek scattering describes the interaction of charged particles in the same bunch (intrabeam scattering) with large momentum exchange. Coulomb interactions between two charged particles causes one particle to slow down and the other to speed up, in this manner the particles may deviate from the nominal energy and escape the trajectory of the beam. Compared to KEKB, the Touschek effect is estimated to increase by a factor of 20 in SuperKEKB due to the nanobeam scheme. To mitigate the number of lost particles that reach the detector, movable collimators are placed around the storage rings, and metal shields are placed near the IR.

Beam-gas Scattering

This process involves Coulomb and Bremsstrahlung scattering of beam particles with residual gas molecules inside the beam pipes. The Coulomb interaction alters the direction of beam particles, while the Bremsstrahlung interaction affects their energy. Due to a smaller beam pipe radius at SuperKEKB, the Coulomb interaction is the dominant effect with a rate up to 100× higher than in KEKB.
The mitigation of scattered particles entering the detector involves installing metal shields and movable collimators near the IP, thus it involves similar counter-measures as those for Touschek scattering.

Synchrotron Radiation

The charged particles in the beams radiate as they are accelerated by bending magnets to keep them in the beam pipe trajectory. For relativistic circular acceleration, the synchrotron radiation power is proportional to the square of the beam energy and the square of the magnetic field strength [32]. Thus, the higher energy ring (HER, e^- beam) is the primary source of radiation as opposed to the low energy ring (LER, e^+ beam). To mitigate the number of radiated photons that enter the detector inner layers, $\mathcal{O}$(KeV), the inner surface of the beam pipes are coated with gold plates, and a ridge pipe design is adopted near the IP.

Radiative Bhabha Scattering

Bhabha scattering involves the interaction of electrons and positrons resulting in photons, electrons and positrons, $e^+e^- \to e^+e^-\gamma$, see Fig. 3.5(a) for a schematic. The radiated photons are often produced at a low angle and travel towards the walls of the beam pipes. The primary background source in the outer layers of the Belle II detector are due to neutrons; these are released from the interaction of the radiated photons with the iron cores of the beam pipe magnets. The rate of interaction is proportional to the luminosity, therefore significantly higher at SuperKEKB compared to KEKB.
At SuperKEKB the employment of a quadrupole magnet system and additional shields help to mitigate the neutron contamination in the detector. However, particles for which the energy loss due to Bhabha scattering is large, do contaminate the IR. They become a source of background in the detector with a rate comparable to Touschek and beam-gas scattering.

Two-photon process

The two-photon process for beam particles involves the exchange of two intermediate photons in the process $e^+e^- \to e^+e^-e^+e^-$, see Fig. 3.5(b) for a schematic. This process

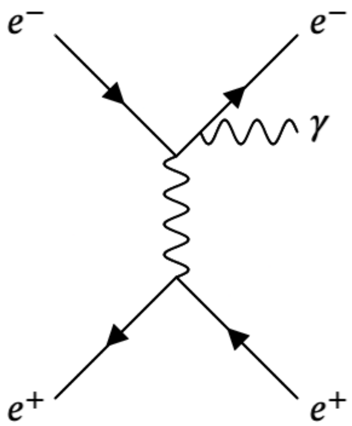

(a)

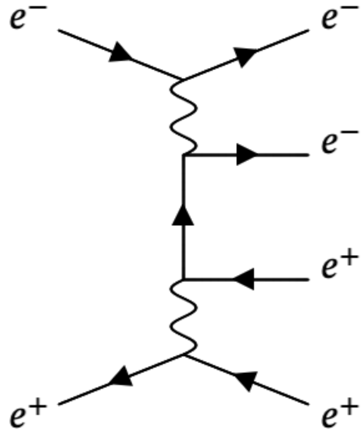

(b)

Figure 3.5.: (a) A low order Feynman diagram representing Bhabha scattering, $e^+e^- \to e^+e^-\gamma$. (b) A two-photon process, $e^+e^- \to e^+e^-e^+e^-$.

is—like Bhabha scattering—also luminosity dependent. Due to momentum conservation, the final electrons and positrons are slow and thus spiral inside the IR becoming a source of background for the detector.

3.2. The Belle II Detector

Like its predecessor (the Belle detector), the Belle II detector is built around the IP with an asymmetric design that is optimized to capture events from asymmetric e^+e^- collisions at near the $\Upsilon(4S)$ energy. In fact, the Belle II detector has been fitted within the same outer shell as the Belle detector, however, the Belle II detector features various significant upgrades.
As discussed in the last section, the increase in luminosity at SuperKEKB results in higher beam-induced background levels compared to KEKB. Consequently, the Belle II detector requires detection systems that can accommodate the higher physics rates and can deal with the increased number of background hits. Moreover, due to the smaller Lorentz boost of $\beta\gamma = 0.28$, compared to $\beta\gamma = 0.42$ at KEKB, a more refined decay-vertex detection system is implemented. The overall design and choice of sub-detector components for the Belle II detector ensure at least a similar level of performance as Belle.

3.2.1. Detector Overview

The Belle II detector is composed of various subsystems of detection (sub-detectors) arranged in cylindrical layers oriented along the beam axis, with the IP at the center.
At the IP is the origin of the detector coordinate system [34], shown in Fig. 3.6(a). The z-axis follows the beam axis in the direction toward the forward region, the y-axis points

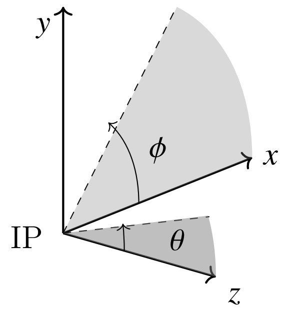

(a)

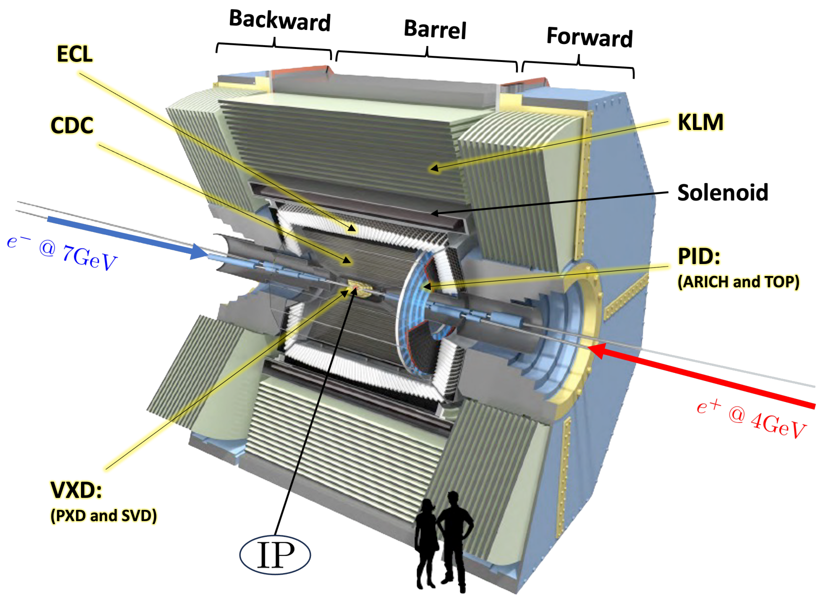

(b)

Figure 3.6.: (a) Belle II detector coordinate system. (b) Cross-sectional view of the Belle II detector [33]. Highlighted in yellow are the main sub-detector components.

upwards, and the x-axis points away from the accelerator rings and is perpendicular to the $y-z$ plane. The azimuthal angle ϕ is measured in the $x-y$ plane and starts parallel to the x-axis. Lastly, the polar (zenith) angle θ is measured in the $y-z$ plane and starts parallel to the z-axis. Note that a distance from the IP in the $x-y$ plane, and distances with respect to the beamline, are given with $r=\sqrt{x^2+y^2}$.

In Fig. 3.6(b), we show a cross-sectional view of the Belle II detector. Due to the asymmetry of the e^+e^- collision, the detector itself is asymmetric, thus some sub-detectors only cover the barrel and forward regions. A superconducting solenoid magnet in the barrel region provides a 1.5 T homogeneous magnetic field to the inner sub-detectors; the field lines point in the z-direction.

The information gathered from the innermost to the outermost sub-detectors enables the reconstruction of particle tracks, their energies, and masses. The detected charged particles involve electrons ($e^\pm$), muons ($\mu^\pm$), pions ($\pi^\pm$), kaons ($K^\pm$), protons ($p^\pm$), and deuterons ($d^\pm$), while the detected neutral particles involve photons (γ) and K-long particles (K_L). Other particles are detected through their decay into the aforementioned particles. The relative abundance of the final-state charged particles at Belle II from $\Upsilon(4S)$ events is shown in Fig. 3.7.

Each sub-detector serves multiple purposes for the detection of particles, these can be summarized in primary tasks. Starting with the innermost sub-detectors, their overarching tasks can be classified in three incremental steps: Tracking, Charged Particle Identification, Neutrals and Lepton Identification.

(The following list serves as a bird's-eye view of the basic capabilities of the Belle II detector.)

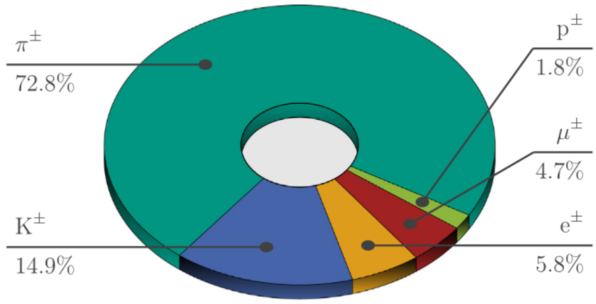

Figure 3.7.: Relative abundance of charged particles from $\Upsilon(4S)$ events. Illustration from [35].

- **Tracking:** Tracking information is collected in the Vertex Detector (VXD) and the Central Drift Chamber (CDC). The VXD consists of a Pixel Detector (PXD) and a Silicon Vertex Detector (SVD).
  The VXD system is positioned closest to the IP and determines the point of origin or intersection of particle products, i.e., their vertex. Tracks that make it into the CDC leave a traceable path as they ionize a gas comprising it. The CDC is the main tracking device at Belle II.
  The vertex and track information from the VXD and the CDC is combined to determine a particle's origin, charge and momentum.

- **Charged Particle Identification:** The Particle Identification (PID) system consists of the Time of Propagation counter (TOP) and the Aerogel Ring-Imaging Cherenkov detector (ARICH). Both detectors are Ring-Imaging Cherenkov (RICH) detectors. The PID system is a powerful discriminator of charged hadrons. Particularly useful is the separation of kaons from pions. The PID system also aids in the distinction between pions, electrons and muons.
  Together with the tracking detectors, the PID information can be used to assign a mass hypothesis to the recorded tracks.

- **Neutrals and Lepton Identification:** The outermost layers of the Belle II detector consist of the Electromagnetic Calorimeter (ECL) and the K_L and Muon detector (KLM).
  Together with the tracking detectors, the ECL can distinguish between electrons, positrons and photons. Likewise, with tracking information, the KLM is used for identifying muons and distinguish K_L mesons from other hadrons.

We follow this categorization with a more detailed discussion of the individual sub-detectors. The characterization of physical properties associated with the trajectory of particles across the entire volume of the detector is discussed in more detail in Chapter 4.

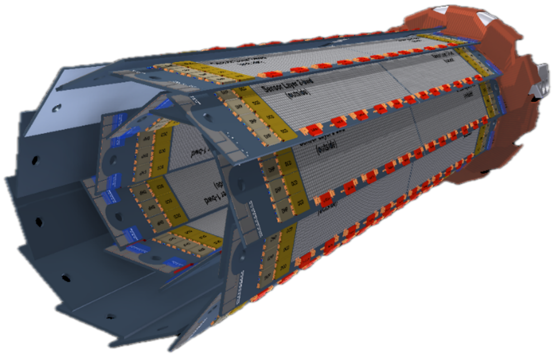

Figure 3.8.: The PXD detector with its inner L1 and outer L2 layers. The gray surfaces contain the pixels. Illustration adapted from [38] CC BY 4.0.

3.2.2. Tracking Detectors

The tracking detectors, VXD (PXD+SVD) and the CDC, all cover a polar angle of $\theta \in [17°, 150°]$.

PXD: The PXD is a silicon pixelated sensor detector[2]. It is the closest detector to the IP. It is organized in two layers, the inner layer (L1, containing 8 ladders) sits at 14 mm radius from the IP, while the outer layer (L2, containing 12 ladders[3]) sits at 22 mm from the IP. An illustration of the PXD is given in Fig. 3.8. The active part of the ladders is approximately 50 μm thick. The PXD consists of a total of 8 million pixels, with each pixel size as small as $55 \times 50\ \mu\text{m}^2$ [27, 33].
The main benefits of the PXD is that it can deal with the extremely high hit rates of SuperKEKB. At its closeness to the IP, the PXD maintains a low occupancy which would not be possible with a strip detector [26, p. 76].

SVD: The SVD is a silicon strip sensor detector located on the outer layers of the VXD at a radius of 38 mm and up to 140 mm from the IP. It consists of 4 double-sided silicon strip detector layers (L3, L4, L5, and L6)[4], the layers' thickness ranges from 300 μm to 320 μm [39]. As a double-sided strip detector, the SVD can measure two 1D coordinates, as opposed to one 2D coordinates in the PXD.
To accommodate readout electronics and adapt to the forward boost, the three outer layers of the SVD are mounted asymmetrically [26, p. 142]. An illustration of the VXD layers is given in Fig. 3.9.

The primary task of the VXD is to collect decay vertex information. However, the VXD is also used for measuring charged tracks with low momentum, as their trajectory is sufficiently curved due to the magnetic field induced by the solenoid.

CDC: The CDC is a large sense wire chamber filled with a gas mixture of 50% Helium and 50% C_2H_6. It surrounds the VXD and consists of 56 layers, the inner layer at a radius

[2]It uses pixelated sensors of Depleted Field Effect Transistor (DEPFET) type [27, 36, 37].

[3]Before LS1, from March 2019 to June 2022, Belle II operated with only 2 ladders in L2.

[4]The layer count starts with the PXD layers.

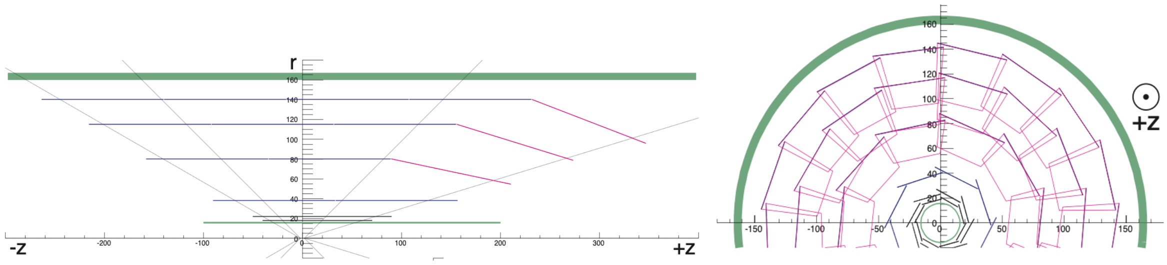

(a) (b)

Figure 3.9.: (a) Side view of the VXD layers. The innermost 2 layers (in black) correspond to the 2 PXD layers, the remaining layers (in blue and magenta) correspond to the 4 SVD layers. (b) Front view of the VXD layers. The axes dimensions are given in mm. Illustrations adapted from [26].

of 160 mm and the outer layer at 1130 mm. A cross-sectional view of the CDC is shown in Fig. 3.10(a).
The CDC involves a total of 14,336 Tungsten sense wires. The sense wires are approximately 30 μm in diameter. Each sense wire is surrounded by 8 aluminium field wires. The field wires generate the electric field needed to drift the electrons exerted by the gas ionization, which occurs when a charged particle traverses the chamber. The field and sense wires form cells, which are smaller for the inner layers of the CDC and can handle the higher event rates at their closer distance to the IP. A depiction of the cells is shown in Fig. 3.10(b).
The CDC has the capability to determine the z-direction of the traversing charged particles, this is achieved through the application of 'stereo' ordered wires (skewed at an angle to the beam axis). The stereo wires are placed in addition to the axial wires, which are oriented along the beam line. In this configuration, the CDC can provide 3D tracking coordinates.
The path that charged particles trace in the CDC allows for the determination of their momentum and charge, i.e., through the Lorentz force that induces a centripetal force,

$$|\vec{p}_T| = RB|q|, \tag{3.3}$$

where R is the radius of curvature, B is the magnetic field strength, and q is the charge of the particle. An example of the trajectories of particles through the CDC is shown in Fig. 3.10(c); for $q > 0$ the track leaves a clockwise curve signature, and for $q < 0$ a counter-clockwise signature.

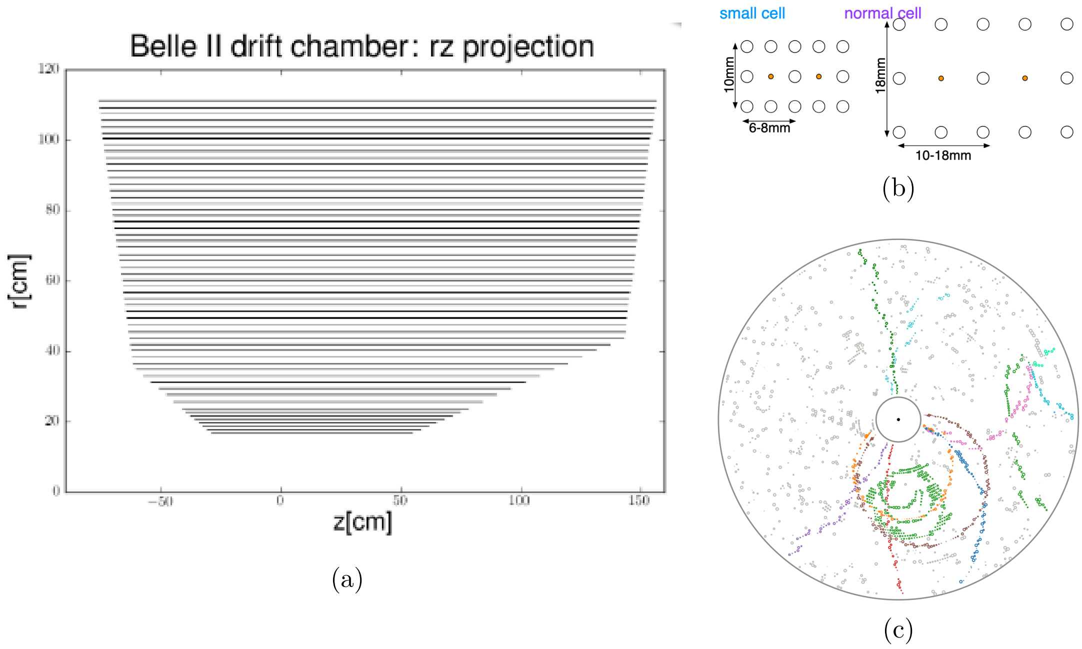

Figure 3.10.: (a) Cross-sectional view of the CDC detector layers, adapted from [40]. (b) CDC cell sizes, adapted from [41]. The orange dots represent the sensing wires, while the unfilled circles represent the aluminium field wires. (c) Example of track signatures left in the CDC ($x-y$ plane, the magnetic field lines point toward the viewer). The colored trajectories display (reconstructed[5]) charged tracks, while the gray spots are background events. Illustration adapted from [33].

The capabilities of the CDC extend beyond tracking, it also serves to provide information of particle types (PID information) through their deposited energy in the gas chamber, $\mathrm{d}E/\mathrm{d}x$. This is especially useful for identifying particles that do not reach the dedicated PID detectors (discussed in the next subsection). An example of the energy loss signature of charged tracks is shown in Fig. 3.11. Moreover, the CDC offers fast trigger[6] information for charged particles, $\mathcal{O}(\mu s)$ [42, p. 13].

[5] The topic of reconstruction is covered in the next chapter, Chapter 4.

[6] The trigger system is discussed in Sec. 3.3.

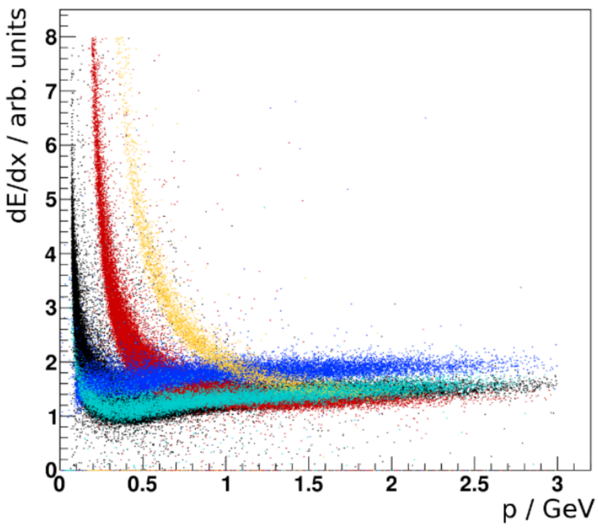

Figure 3.11.: Typical energy loss signatures as functions of momentum for charged particles: electrons, muons, pions, kaons, protons. Illustration adapted from [40].

3.2.3. Charged Particle Identification Systems

The PID system consists of the TOP (in the barrel region) and the ARICH (in the forward endcap region). An illustration is shown in Fig. 3.12. They both make use of the Cherenkov effect.

The Cherenkov effect applies to charged particles traversing a dielectric medium with a velocity v which is faster than the speed of light inside that medium, $v > c/n$, where c is the speed of light and n is the refractive index of the dielectric medium. The charged particles polarize the medium thereby emitting (Cherenkov) photons. The photons build a wave-front, where the angle between the perpendicular vector to the wave-front and the direction of travel of the charged particle is denoted as θ_c, such that

$$\cos\theta_\mathrm{c} = \frac{(ct/n)}{\beta ct} = \frac{1}{n\beta}. \tag{3.4}$$

A depiction of the Cherenkov effect is shown in Fig. 3.13.

TOP: The TOP is a ring imaging Cherenkov detector that reflects (Cherenkov) photons inside quartz radiator bars. The TOP measures both the time it takes for photons to travel and their positions in the $x-y$ plane when they reach the photon detectors located at the ends of the radiators. A depiction of reflected photons inside a quartz radiator bar is shown in Fig. 3.14.

The TOP surrounds the CDC in the barrel region at a radius of 120 cm from the IP. It consists of a total of 16 modules, each module consists of 2 quartz radiators (glued together along the z-axis) for a total length of 275 cm. The quartz bar width is 45 cm and the thickness is 2 cm. The TOP covers a polar angle of $\theta \in [31°, 128°]$.

The 3D information (time of propagation, x and y coordinate) allows for the reconstruction of the Cherenkov angle, which in turn gives information about the velocity of the traversing

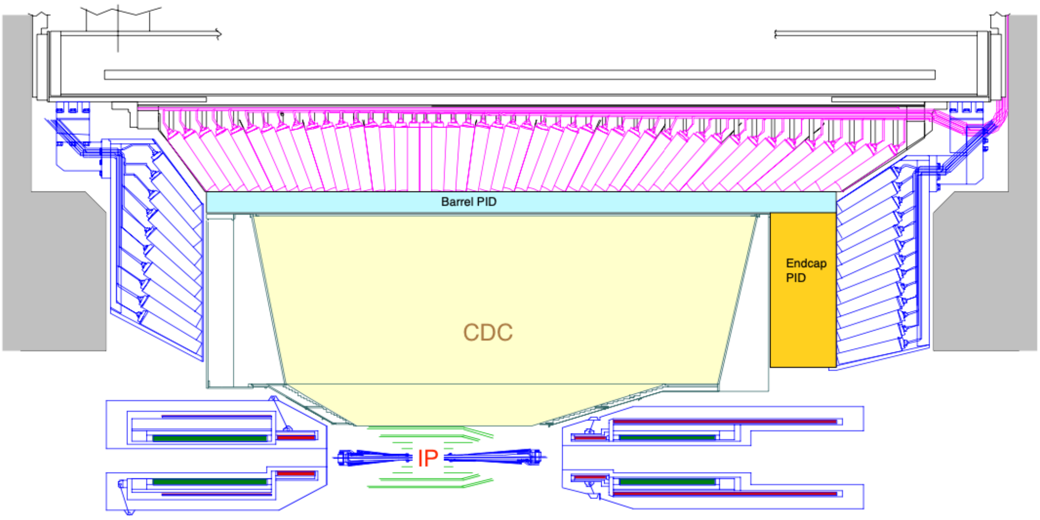

Figure 3.12.: TOP (Barrel PID) and ARICH (Endcap PID) positions in the Belle II detector (close-up look). For reference, the CDC and the IP are also labeled. Illustration adapted from [42].

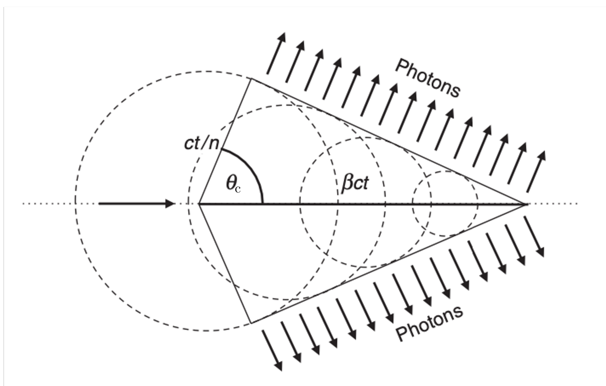

Figure 3.13.: Cherenkov radiation for charged particles traversing a dielectric medium with $v > c/n$. Illustration adapted from [9].

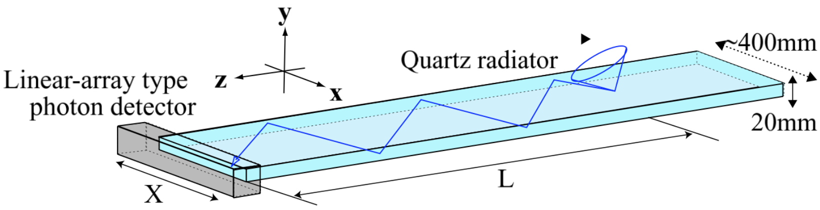

(a)

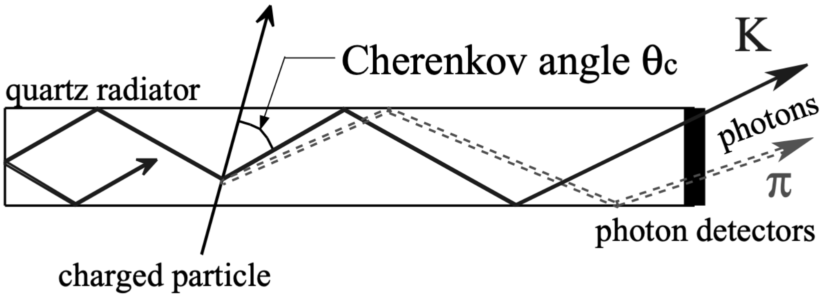

(b)

Figure 3.14.: (a) Schematic of the TOP quartz radiator bar. (b) Side view of the quartz bar (along the z direction). Illustrations adapted from [42].

particle (using Eq. (3.4)). Therefore, using the momentum information retrieved from the tracking detectors, one can assess a mass hypothesis.

ARICH: The ARICH is a ring-imaging Cherenkov detector that uses aerogel radiator disks to focus Cherenkov photons. It is located in the forward endcap, covering the forward $x-y$ plane of the CDC with a polar angle of $\theta \in [14°, 30°]$.
The ARICH uses two stacked radiator disks, each 2 cm wide and with differing refractive indices, $n_1 = 1.045$ and $n_2 = 1.055$. When charged particles enter the aerogel radiators, they emit Cherenkov photons that produce a ring image in the photon detectors, called Hybrid Avalanche Photo Diodes (HAPDs), which are located approximately 16 cm apart from the aerogel. The difference in refractive indices is what focuses the Cherenkov photons to a common ring. An illustration of this principle is shown in Fig. 3.15(a). In order to mitigate the loss of Cherenkov photons, planar mirrors are positioned coaxially to the beam axis that reflect the photons back to the HAPDs [43], as shown in Fig. 3.15(b). Like the TOP, ARICH can be used to determine the mass of the charged particle. It is a powerful particle identifier capable of distinguishing between hadron types, especially kaons from pions. Together with the tracking detectors, it also aids in the separation between pions, muons and electrons in the low momentum range (below 1 GeV/s) [26, p. 250], [43].

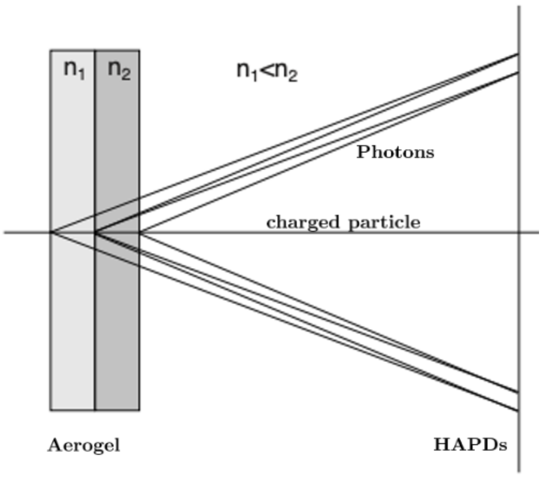

(a)

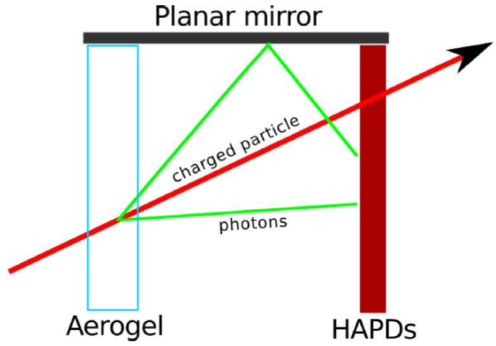

(b)

Figure 3.15.: (a) Focusing of Cherenkov photons using different refractive indices, adapted from [26]. (b) Use of planar mirrors to mitigate the loss of Cherenkov photons, adapted from [43].

3.2.4. Neutrals and Lepton Identification Systems

The outermost layers of the Belle II detector consist of the Electromagnetic Calorimeter (ECL) and the K_L and Muon detector (KLM). The solenoid is located between the ECL and the KLM.

ECL: The ECL is a scintillation crystal detector that surrounds the inner detectors discussed so far. It covers the forward, barrel, and backward regions of the Belle II detector with a polar angle θ in segments of $[12.4°, 31.4°]$, $[32.2°, 128.7°]$, and $[130.7°, 155.1°]$, respectively. The gaps accommodate readout electronics and related components. A figure displaying the ECL was shown earlier in Fig. 3.12, the magenta colored region (above the barrel PID) denotes the barrel part of the ECL, while the blue colored regions on the sides denote the (forward and backward) endcaps.
The ECL consists of a total of 8736 crystals, where the barrel consists of 6624 CsI(Tl) crystals, and the endcaps consist together of 2112 pure CsI crystals. The difference in crystal material is chosen as such to deal with the higher background rates in the endcaps [42, p. 57]. The crystals are shaped as truncated pyramids with a cross-sectional area of $6 \times 6\ \text{cm}^2$ and length of 30 cm [44].
Photons, electrons and positrons inside the ECL create electromagnetic showers, i.e., electrons create successive photons via Bremsstrahlung and photons (with enough energy) create e^+e^- pairs which leads to a cascade of photons, electrons and positrons. This continues until a maximum number of radiation lengths, or a critical energy, is reached that depends on the initial energy of the incoming particle and the material which the particle traverses. Due to the higher rates of interaction, a high-Z material leads to shorter radiation lengths. With $\mathrm{d}E/\mathrm{d}x = E/X_0$, for each radiation length X_0, the particle retains $1/e$ of its energy while the number of shower particles approximately doubles [9]. A depiction of an electromagnetic shower is shown in Fig. 3.16. The ECL crystals accommodate approximately $16.2X_0$ in their 30 cm length [44].

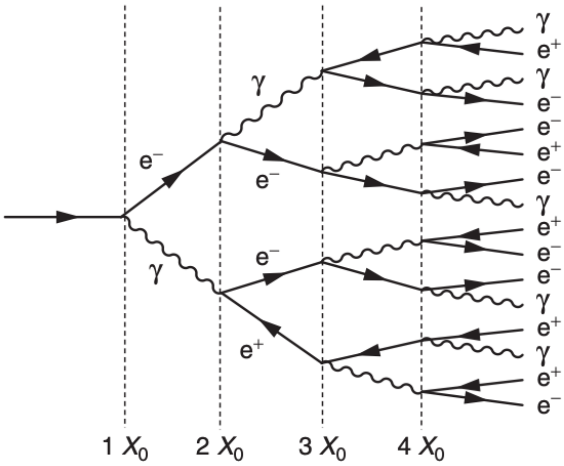

Figure 3.16.: Example of an electromagnetic shower. Illustration adapted from [9].

The ECL accomplishes several tasks. It is devoted to the identification of neutrals, especially those that decay into photons (e.g. $\pi^0 \to \gamma\gamma$). It provides precise information about the energy and position of photons that shower in the crystals. Together with the tracking detectors, it identifies electrons/positrons and separates them from hadrons. Together with the KLM, it aids in the identification of muons and K_L particles. It serves as a reliable signal trigger which is also used for luminosity studies (e.g. by identifying Bhabha and $\gamma\gamma$ events) [26, p. 369].

KLM: The KLM consists of alternating iron plates with active materials. It is positioned outside the solenoid (barrel), and around the ECL (endcaps), covering a total polar angle of $\theta \in [25°, 155°]$. The iron plates are 4.7 cm thick and serve as the path-way for the magnetic flux return of the solenoid. In addition, the iron plates offer $3.9\lambda_I$ (nuclear interaction lengths[7]) for K_L (hadronic) showers; this comes in addition to the $0.8\lambda_I$ from the ECL.

The KLM comprises of 14 layers in the barrel region and 12 layers (each) in the backward and forward endcaps [27, p. 45]. The active material in the barrel region is based on glass-electrode resistive plate chambers (RPCs [26, p. 315]) for the outer 12 layers, the 2 innermost layers in the barrel and the ones in the endcaps comprise of scintillator strip layers. The use of scintillators instead of RPCs for the inner layers is necessary due to the high background rates at SuperKEKB [46].

As the KLM is positioned outside the solenoid, charged particles that make their way into the KLM (above 600 MeV) traverse almost in straight lines. While the K_L is identified by hadronic showers, the identification of muons and non-showering hadrons is possible in conjunction with the tracking and PID detectors.

[7] $\lambda_I = A/(N_A\sigma_{\text{tot}})$, where A is the atomic number of the material, N_A is the Avogadro's number, and σ_{tot} is the total cross section of the hadron interaction with the material. [45]

3.3. Trigger System

As it is impossible to store every detector signal, Belle II implements a trigger system (also referred to as the *online* system). The trigger system consists of a hardware-based low-level trigger (L1 trigger) used in the initial phase of data-taking, and a software-based high-level trigger (HLT) that greatly reduces the data size by removing misidentified events (fakes).

L1 trigger: Generally, the trigger system is limited by the data acquisition (DAQ) system. In order to keep the deadtime of the DAQ system at a minimum, the L1 trigger is tuned to a set of sub-detectors that offers fast ($\sim 5\mu$s) and reliable (low fake rate) trigger information: At a maximum rate of 30 KHz, the L1 trigger merges the sub-trigger information collected by the CDC, the ECL, the TOP[8], and the KLM. This sub-trigger information is sent to a Global Decision Logic (GDL) system for a final decision on whether to trigger over all the other sub-detectors (and eventually store the full event information), or reject it entirely.

HLT: The HLT further classifies the event data by performing a fast reconstruction[9] of interesting events (e.g., hadron events). It removes residual backgrounds caught by the L1 trigger and brings the online event rates down to 10 KHz. If the HLT criteria are fulfilled, the classified events are stored to an *offline* storage (this is the data used for *offline* analyses). The stored data is typically only 40% of the original L1 triggered data.

A schematic of the trigger system is shown in Fig. 3.17. Due to the high hit rates near the IP, the HLT algorithms use the L1 triggered data from all the sub-detectors except the PXD. The L1 triggered data is processed in the Event Builder 1. The PXD hit information is sent to the Event Builder 2 to extrapolate down from the other tracking detectors (SVD+CDC) based on the HLT outcome.
Although the trigger system records events that satisfy given criteria for certain interesting physics events, it also intentionally triggers on a few background events such as Bhabha scattering for calibration purposes (so-called prescaling [33]).

3.4. Belle II Data

Data-taking runs[10]—which are based on similar hardware and software configuration—are grouped into sets called "experiments", often abbreviated as "exp#", where "#" stands for a classifying number given to the set.
The processing of collected data is split into prompt processing and reprocessing [33]. The prompt processing involves the calibration of data taken in run periods of about two weeks, referred to as a "bucket". Reprocessing is the (re-)calibration of a collection of buckets, spanning one to two years of data collection; it is referred to as "proc#", where "#" is a designating number that differentiates it from previous collections.[11]

[8] The TOP is only used indirectly in the L1 trigger [33, Sec. 3.2.2.].

[9] The topic of reconstruction is covered in Sec. 4.1.1.

[10] Not to be confused with the long SuperKEKB run periods RUN1 and RUN2.

[11] A proc-collection may be expressed as a sum of "chunk" groups, which are groups of experiments. For

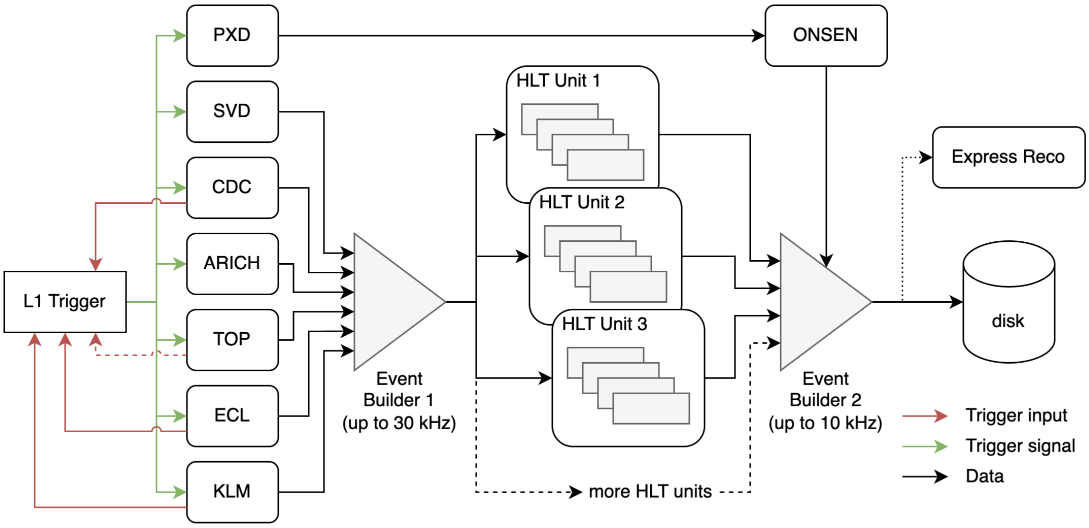

Figure 3.17.: Belle II trigger system overview [33]. The main sub-trigger systems of the L1 trigger are denoted with red arrows (trigger input). The green arrows (trigger signal) denote a positive decision by the GDL.

The amount of data collected over a period of operation is quantified in terms of the integrated luminosity $\mathcal{L}_{\text{int}}$,

$$\mathcal{L}_{\text{int}} = \int_{t_i}^{t_f} \mathcal{L}(t)\,\mathrm{d}t, \tag{3.5}$$

where t_i denotes the initial time of data-taking and t_f denotes the last recorded time. As of 2024, Belle II has recorded $\mathcal{L}_{\text{int}} = 575\,\text{fb}^{-1}$ of data (for collisions at, above, and below the $\Upsilon(4S)$ energy). This is a little over half of the recorded data at Belle ($\sim 1\,\text{ab}^{-1}$). In Fig. 3.18 we show the progress of the data recorded since the start in 2019.
As discussed at the end of Sec. 3.1.2, much of 2024 was dedicated to solving the sudden beam loss (SBL) problem. In RUN 2 (January 2024 until the present day) only $148\,\text{fb}^{-1}$ of data has been collected; in RUN 1 (March 2019 to June 2022) $427\,\text{fb}^{-1}$ were collected. In order for the Belle II program to achieve an instantaneous luminosity of 6×10^{35} cm^{-2} s^{-1} and reach the integrated luminosity goal of $50\,\text{ab}^{-1}$, several upgrades to the Belle II detector and the SuperKEKB collider are planned [31], some of which will be implemented in the next shutdown phase (LS2).

example, proc13 stands for data collected in the years 2019 to 2021, and it is composed of 5 chunks: chunk1 contains exp7-10, chunk2 contains exp12, chunk3 contains exp14, chunk4 contains exp16-17, and chunk5 contains exp18.

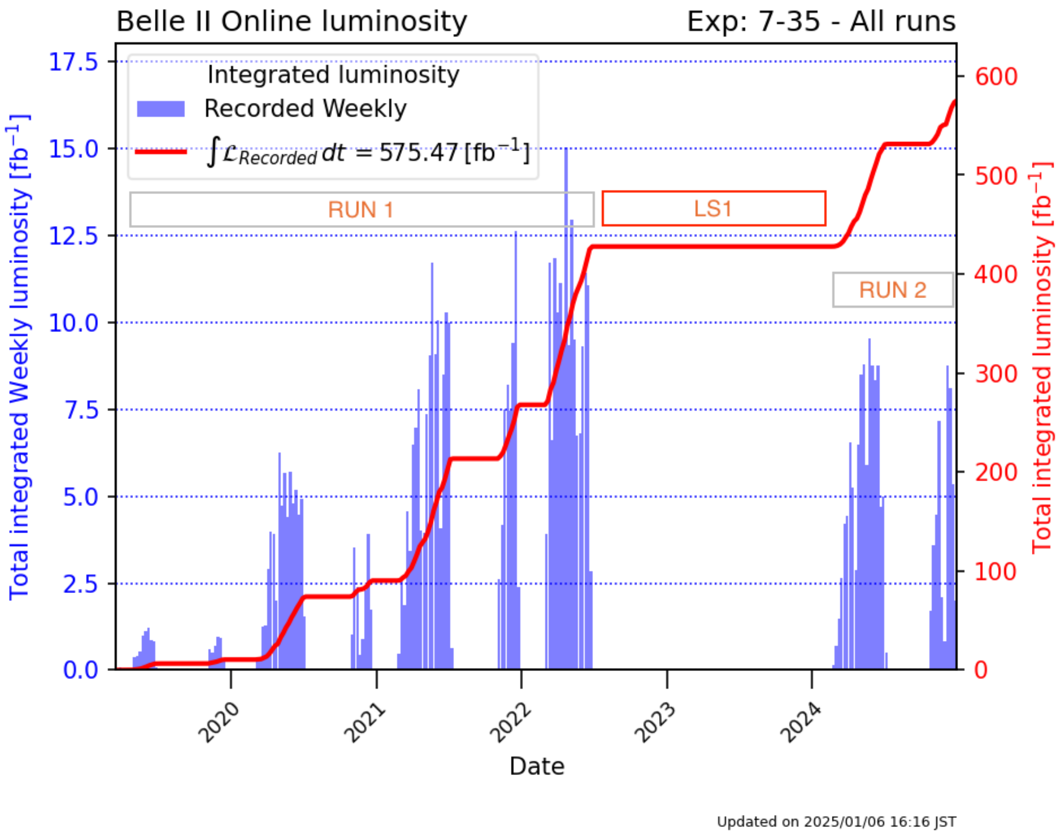

Figure 3.18.: Integrated luminosity evolution since 2019. ©Belle II Collaboration.

Physics process	cross section [nb]
$\Upsilon(4S)$	1.11
$u\bar{u}(\gamma)$	1.61
$d\bar{d}(\gamma)$	0.40
$s\bar{s}(\gamma)$	0.38
$c\bar{c}(\gamma)$	1.30

Table 3.1.: Cross sections of hadronic events at 10.58 GeV [27].

3.5. Belle II Simulation

The simulation of events is essential to physics analyses at Belle II. Especially important is the reconciliation between the expectation of physics events and the detector response. Naturally, a simulation is model dependent. For the present thesis, the event generation from e^+e^- collisions at the $\Upsilon(4S)$ energy is based on the SM. These events are generated using the Monte Carlo method (MC) through several generator packages [27]. `EVTGEN` [47] is used for the generation of $B\overline{B}$ events and subsequent decay chains into exclusive[12] final states. The generation of continuum events ($e^+e^- \to q\overline{q}$ with $q = u, d, s, c$) is done with `KKMC`[48]. Both packages are interfaced with `PYTHIA`[49] for the generation of inclusive[13] final states. Other physics generators, e.g., for leptonic events, beam backgrounds and radiative effects, are listed in [50].
Relevant production cross-sections for the generation of hadronic MC events from collisions at 10.58 GeV are shown in table 3.1. The cross section σ of a given process relates to the number of generated interactions N by the equation $\sigma\mathcal{L} = \mathrm{d}N/\mathrm{d}t$, thus $N = \sigma\mathcal{L}_{\mathrm{int}}$. The cross section is given in units of area, where $1\,\mathrm{b} = 10^{-28}\mathrm{m}^2$.
To simulate the observed physics, the generated particles must travel through the detector material. The detector response is simulated using `GEANT4` [51].

Samples made up of MC simulated events are referred to as MC samples. One major benefit of using MC samples is that the *truth* information is retrievable, i.e., the origin and the decay chain of the generated particles is known. Therefore, the truth information helps to separate MC signal events from MC background events.

[12] A decay mode with specified final state particles.

[13] A decay mode with unspecified final state particles.

4. Reconstruction and Analysis Methodology

In this chapter, we introduce the *reconstruction* and *analysis* methodologies employed at Belle II for characterizing particle tracks and particle decays. We follow the introduction with a general overview of the reconstruction and analysis procedure applied to our study of Λ_c^+ and Ξ_c.

4.1. Belle II Analysis Software Framework

The Belle II Analysis Software Framework (`basf2` [52]) is the main software used for the processing of data and simulation at Belle II. Its application spans from the early stages of (online) data handling to the later stages in the (offline) analyses. One of the primary uses of `basf2` is in the reconstruction of events, i.e., the association of physical properties of particles to the tracking and hit information gathered by the detectors. The reconstruction of simulated events undergoes the same procedure as done for data.
`basf2` is based on independent (`c++` and `python`) modules configured in a *steering* script. The modules are loaded to a `path` within the script and executed linearly. Each module dynamically reads (writes) information from (to) a `dataStore` which is allocated to an input file called in the script. Input files are `ROOT` [53, 54] files that contain a collection of events with related beam and detector information. The exchanged information with the `dataStore` is passed as objects, e.g., objects that associate particle types to the tracking information provided in the input file. An essential discriminator in the input files is the `eventMetaData` which provides information about each processed event (event number, run, experiment number) and whether the event is simulated [52].
The output is itself provided in `ROOT` file format, where `dataStore` objects are saved as branches within the `TTree` structure of the `ROOT` file system.
In a physics analysis, one is interested in the reconstruction results for variables defined in the steering file (such as mass, energy, momentum, etc.). The results are stored in an `Ntuple`. An `Ntuple` is a `TTree` limited to float variables, with each variable allocated to its own branch [54]. Moreover, an `Ntuple` is candidate-based [33], i.e., the variable results are arranged in rows corresponding to each reconstructed event, and only events that meet the criteria specified in the steering file are included in the output.

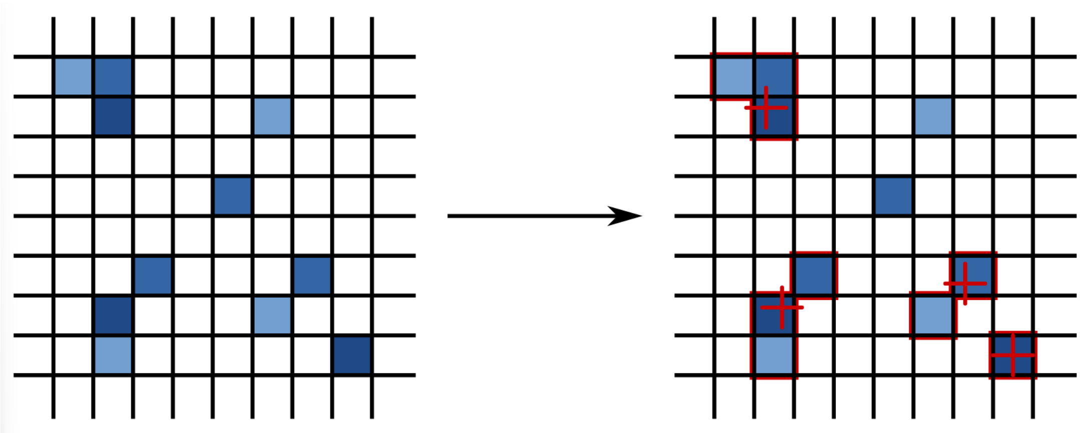

Figure 4.1.: Example of grouping 2D hits with analog information (e.g. ionisation amount) into clusters [33]. The red crosses represent the weighted means of each cluster.

4.1.1. Track Reconstruction

We discuss the primary methods used in `basf2` for the reconstruction of particle tracks, and clarify what is meant by hits and tracks within the framework.

Clustering

Due to the finite resolution in the detection of particles that enter the detector sublayers, neighboring hits (and related detector responses) are grouped together to form clusters. An example of cluster building is shown in Fig. 4.1. This example applies well to the clustering of PXD hits. A similar procedure is taken for neighboring hits found in the layers of the other sub-detectors. Notably, for the ECL, the situation is a bit more complex as particles may cause showers across multiple crystals. The clusters in the ECL are based on the position and the deposited energy of the traversing particles; they are formed around one crystal with an energy deposit of at least 10 MeV [27, p. 65] and only neighboring crystals that touch each other in a 5×5 arrangement are added to the cluster. Per convention, clusters are often simply referred to as hits.

Track Parametrization

The trajectory of a charged particle traversing through the tracking detectors forms a helix shape—the trajectory is curved due to the magnetic field induced by the solenoid. Thus, the position $\vec{x} = (x, y, z)$ and the momentum $\vec{p} = (p_x, p_y, p_z)$ of a charged track can be parametrized as a *Perigee helix* composed of 5 parameters [27, p. 58][55]. The helix is defined at the Perigee, which is the point of closest approach (POCA) of the charged track to the origin of the coordinate system. Using Fig. 4.2 for reference, the helix parameters are defined as follows:

- d_0 is the signed distance of the POCA to the z-axis (projected onto the $x - y$ plane). The sign is taken from the sign of the z-component of the momentum vector $\vec{p}$ (with respect to the origin).

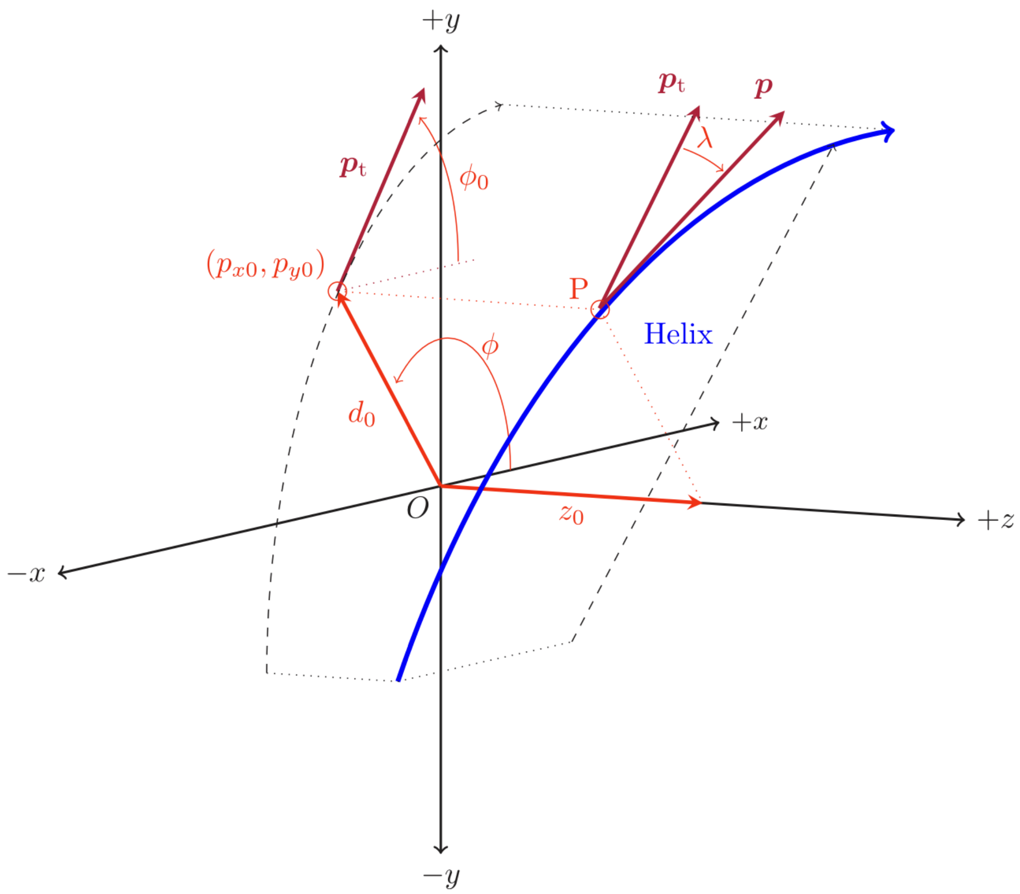

Figure 4.2.: Belle II helix parametrization. The POCA is denoted by **P**. Illustration adapted from [55].

- ϕ_0 is the angle between the transverse momentum vector $\vec{p}_t = (p_x, p_y)$ and the x-axis.
- ω is the signed curvature (i.e., the reciprocal transverse momentum Q/p_t). The sign corresponds to the charge Q of the particle.
- z_0 denotes the z-component of the POCA.
- $\tan\lambda$ is the last component parametrizing the helix, where λ is the angle between $\vec{p}_t$ and $\vec{p}$, i.e., with respect to the $x-y$ plane.

Track Finding[1]

Track candidates are found by relating hits to other hits in each tracking detector. Different pattern recognition algorithms are implemented for finding tracks in the CDC and the VXD.

[1]This subsection is substantially based on the Belle II Track Finding publication [35].

CDC Track Finding: The CDC track finding consists of two algorithms.

- A global track finding algorithm: It involves a Legendre transformation of the helix parametrisation where peaks of binned hits are identified for particles that are assumed to originate at the IP. The transformed helix also accounts for missing hits in the CDC layers. The algorithm starts by approximating the 2D position information of the CDC hits (only axial wires) as drift circles (which are also circles in the Legendre space). These are combined with the z-directional information provided by the stereo wires for a 3D positional account, where the stereo wire hits are approximated as straight lines in the Legendre space. The most populated intersections in the Legendre space are selected for the formation of tracks.

- A local track finding algorithm: This algorithm involves the Cellular Automaton concept (CA) which identifies neighboring tracks and accounts for displaced vertices, i.e., it identifies extensions of tracks that do not necessarily have their origin at the IP. The CA groups hits into segments (based on groups of axial and stereo layer cells) and extrapolates the trajectory of tracks from one segment to the other—even if hit information is missing from the CDC layers. Different segments are then combined and weighted to form longer tracks.

The two algorithms are merged to form the tracks found in the CDC. The global track finding algorithm builds the baseline for finding the best track, while the local algorithm results are added to the global one based on a multivariate approach—where the most optimal tracks are found using MC simulations.

VXD Track Finding: The main tracking algorithm employed in the VXD is based on the CA, which functions in a similar manner as the local tracking algorithm of the CDC. VXD tracking is essential for reconstructing tracks of particles that do not reach or only leave a few hits in the CDC, e.g., particles where the transverse momentum is less than 100 MeV [35, p. 9].
Finding SVD tracks involves creating graphs of related space points. The space points are determined by dividing the SVD detector geometry into sensor sections (sectors). Tracks found in different sectors are related to form a path and the best path becomes an SVD track candidate. An illustration of this principle is shown in Fig. 4.3.

Merging Tracks: The main algorithm used at Belle II for merging the tracks from the SVD, the CDC, and eventually the PXD, is the Combinatorial Kalman Filter (CKF). The CKF is an iterative local algorithm that is equivalent to a least square fit. Candidate hits are added to the extrapolated track one by one across the volume of the detector. The algorithm accommodates parameter inputs that encapsulate the deviations from an idealized track (e.g. that account for the non-uniform magnetic field, multiple scatterings and other losses).
The extrapolation starts with tracks found in the CDC, to which SVD hits are then attached, resulting in the merging of candidate tracks from the CDC with those from the SVD. The merged tracks are used to determine interesting hit regions in the PXD. Lastly, the CKF is repeated to attach the selected PXD clusters to the merged CDC+SVD tracks. This approach is fast and efficient against the high background level at SuperKEKB, and improves the track resolution quantified by the helix parameters d_0 and z_0 by a factor of two or more [35, p. 12].

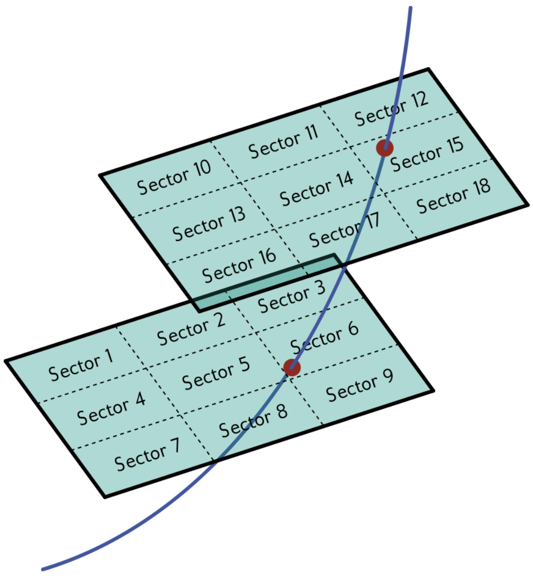

Figure 4.3.: SVD track finding by relating sector graphs. Illustration adapted from [35].

Track Fitting

The trajectory of the tracks is built by fitting them across all the tracking detectors. The main algorithm used for track fitting is the Deterministic Annealing Filter (DAF) provided by the `GENFIT2` package [56]. For the fit, a particle hypothesis is given to the tracks to account for their interactions with the detector material and their energy losses. The tracks are fitted with three hypotheses (p, K and π), then stored offline for subsequent physics analyses [35].
The best estimates of the track fitting procedure are used for the determination of the position and the momentum of charged particles.

4.1.2. Likelihood Ratios

Using MC simulations, a likelihood can be determined for every final-state particle hypothesis (p, K, π, d, e, μ). That is, a likelihood can be assigned to a track based on the expectations of a given hit signature in the sub-detectors. As briefly mentioned in Sec. 3.2.2, besides providing momentum information, the CDC can assign a particle hypothesis to a track by the amount of deposited energy in its volume. Fast tracks that make it into the vicinity of the PID detectors (TOP+ARICH, Sec. 3.2.3) are given a particle hypothesis based on hit signatures associated with the track. In this manner, the velocity of the hypothesized particle is determined through the Cherenkov angle, and a mass hypothesis can be assigned to the track. Similarly, hits in the ECL and the KLM, discussed in Sec. 3.2.4, are associated with trajectories given a particle hypothesis. Details about the individual sub-detector likelihood functions are discussed in [27].
For a physics analysis, one often wishes to reconstruct tracks associated with a certain particle type. The reconstruction of a track identified as being of particle type i, is expressed as the ratio between the combined likelihood $\mathcal{L}_i$ (from all the sub-detectors) and the sum of all the combined likelihoods assuming different particle hypotheses. The

identification (ID) of a particle i reads,

$$i_{ID} = \mathcal{L}_i/(\mathcal{L}_e + \mathcal{L}_\mu + \mathcal{L}_\pi + \mathcal{L}_K + \mathcal{L}_p + \mathcal{L}_d), \qquad i = p, K, \pi, d, e, \mu. \tag{4.1}$$

This is the standard PID definition used in analyses with `basf2`. It is also referred to as a *global* PID to differentiate it from a *binary* PID. Compared to the global PID, the binary PID is a more flexible condition on the ratio of particle likelihoods as its main application is to distinguish the relative identification of a given track from another track. For example, in the decay $\Lambda^0 \to p\pi^-$, the ID of a proton track w.r.t. the pion track, reads

$$\text{binaryID}(p:\pi) = \mathcal{L}_p/(\mathcal{L}_p + \mathcal{L}_\pi), \tag{4.2}$$

and similarly, we can express the binary ID of a pion track w.r.t. the proton track,

$$\text{binaryID}(\pi:p) = \mathcal{L}_\pi/(\mathcal{L}_p + \mathcal{L}_\pi). \tag{4.3}$$

4.2. Systematic Corrections Framework

In general, MC simulations do not perfectly model the efficiencies from particle ID selections in the measured data [57]. The discrepancy can be lessened by applying correction weights to the MC candidates based on deviations of control modes in the data.
The identification performance of the proton, pion, and kaon have been studied at Belle II using the following control modes:

$$\Lambda^0 \to p\pi^- \tag{4.4}$$

for identifying protons [58],

$$D^{*+} \to [D^0 \to K^-\pi^+]\pi^+ \tag{4.5}$$

for identifying kaons [59], and

$$K_S^0 \to \pi^+\pi^- \tag{4.6}$$

for identifying pions [60]. The benefit of using these modes is that a good selection can be achieved without applying any PID constraints [57].
The estimation of the data/MC efficiency corrections and application of weights can be carried out offline using the Belle II Systematic Corrections Framework. For the application of weights, the package `PIDvar` can be used in a Jupyter notebook. The Systematic Correction Framework also allows for a direct computation of efficiencies on online data during the reconstruction process. However, the offline treatment generally offers better visualization for a single mode analysis.
The data/MC efficiency estimation and generation of weights is based on a given selection criteria, involving PID thresholds (commonly referred to as PID cuts). The weights are generated for each selected charged track in bins of their momentum p (in the laboratory frame of reference), their polar angle θ, and their charge sign (+1 or −1).
To obtain the overall correction weight factor for a given mode that involves several tracks, the individual charged particle weights are multiplied together. For example, in the decay $\Lambda_c^+ \to pK^-\pi^+$, the weight contributions from p, K, and π, give the overall factor that corrects the PID selection efficiency in MC, for reconstructed $\Lambda_c^+ \to pK^-\pi^+$ candidates.

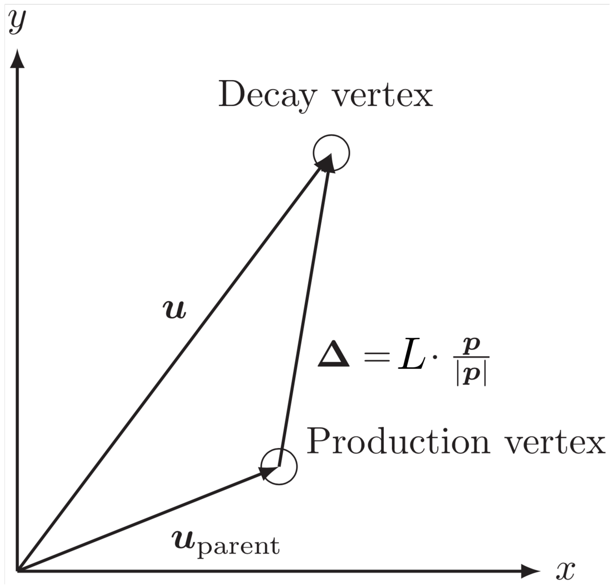

Figure 4.4.: Simplified 2D illustration of the flight length $\boldsymbol{L}$ in `TreeFit`. $\boldsymbol{u}$ represents the coordinate vector of the decay vertex of an intermediate particle, $\boldsymbol{u}_{\text{parent}}$ represents the coordinate vector of the decay vertex of the parent particle (the point at which the intermediate particle was produced). Δ is the vector quantifying the flight distance of the intermediate particle in the direction of its momentum. Illustration adapted from [55].

4.3. Vertex Fit

Vertex reconstruction algorithms are essential for determining the location where related tracks intersect. They provide information about the presence of intermediate states, i.e., composite particles which are formed by a combination of final state particles. By rejecting unwanted tracks, vertex fit algorithms can also drastically improve the resolution of particle kinematics.

Of special utility to the analysis presented in this thesis is the `TreeFit` algorithm [55]. It is one of three vertex fit implementations at Belle II [27, p. 89]. `TreeFit` executes a global fit over the entire specified decay chain. It finds a best fit to the vertex positions, 4-momenta, flight lengths and covariance matrices of all the intermediate particles involved in the chain—the determination of these parameters is discussed below. Final state particles are determined alone by their PDG masses and (3-)momenta.

The flight length $\boldsymbol{L}$ is defined as the distance between the production vertex of a particle and its decay vertex. The production vertex of a particle is synonymous with the decay vertex of its *parent* (the composite particle from which the particle originates, also referred to as the *mother*). An illustration is provided in Fig. 4.4.

Intermediate particles that decay via the strong force (with a lifetime of less than 10^{-14} s, i.e., $\boldsymbol{L} \sim 1\,\mu$m) are assumed to have the same decay vertex position as the decay vertex of the parent.

Particle	Parameters	Constraints
track	$p_x,\ p_y,\ p_z$	5 (from helix parametrization)
photon	$p_x,\ p_y,\ p_z$	3 (the highest momentum is vetoed [55, p. 6])
intermediate	$p_x, p_y, p_z,$ E, x, y, z, L	4 (kinematic) + 3 (geometric) + 1 (mass)

Table 4.1.: Parameters determined by `TreeFit` and associated number of constraints [33]. For clarity, the geometric constraints refer to the condition $0 = u_{\text{parent}} + \Delta - u$ which is illustrated in Fig. 4.4, see also [55, p. 7].

Determination of Best Parameters

The initial vertex positions are chosen at the POCA of a track; If the track originates from a composite particle (a parent), the initial vertex positions are set to the POCA of the parent; If it is undetermined, the IP is assumed as the origin.
The algorithm uses an extended Kalman filter, i.e., a least square estimator. It iteratively associates constraints (parameter equations based on knowledge from measurements and expectations) to a set of hypothesized track parameters. Each constraint reduces the dimension of the parameter space used for the fit. In table 4.1, we list the parameters and constraints corresponding to a track, photon, and intermediate particle. Note that the total number of constraints must be greater than the number of parameters extracted. The number of degrees of freedom used in the fit result from the number of constraints minus the number of extracted parameters [33].
The χ^2 of the fit is determined for every iteration α as a weighted sum of k sets of equations (i.e., the constraints), [55]

$$\chi^2_\alpha = \sum_k \underbrace{(x_k - x_{k-1})^T C_{k-1}^{-1} (x_k - x_{k-1}) + (m_k - h_k(x_k))^T V_k^{-1} (m_k - h_k(x_k))}_{\chi^2_k}, \tag{4.7}$$

where

- x_k is the state vector containing the set of parameters to be retrieved from the fit, $(x, y, z, p_x, p_y, p_z, E, L, ...)$, for each constraint,
- m_k is the vector obtained from the measurement $(d_{0,m}, \phi_{0,m}, \omega_m, z_{0,m}, \tan\lambda_m)$,
- $h_k(x_k)$ is the vector of the hypothesis $(d_0, \phi_0, \omega, z_0, \tan\lambda)$,
- V_k is the covariance matrix of the measurement, and
- C_k is the covariance matrix of the hypothesis.

The minimization of χ^2_k defines the rule by which a state vector x_k is obtained,

$$x_k^\alpha = x_{k-1}^\alpha - K_k^\alpha \cdot (m_k - h_k(x_{k-1}^\alpha)), \tag{4.8}$$

where K is a gain matrix used by the Kalman Filter, its derivation is outline in [55].

Thus, each new state vector is updated based on the outcome of the previous state, and the hypothesis used for each constraint is based on the outcome of a state vector corresponding to the previous constraint.
The last iterated state vector gives the best hypothesis for the parameter values. This applies as long as the change in the χ^2 remains below 2% [55, p. 4].

4.4. $V0$ Objects

Complementary to the standard reconstruction of tracks (using the track finding algorithms), is the reconstruction of $V0$ objects [27, p. 61]. $V0$ objects are combined tracks of opposite charge (they form a V-shape), where the hit information in the detector layers is exploited and extrapolated down to a common vertex where the tracks meet. This is primarily used for the reconstruction of long-lived neutral particles (like Λ^0), where the decay vertex is significantly displaced from the IP. If the hit extrapolation succeeds and a common vertex is found, a vertex fit is performed and the results are stored for offline analyses.
`basf2` implements a `V0Finder` module, which can be used to collect a list of candidate $V0$ objects that pass certain selection criteria, e.g., the invariant mass of the oppositely charged tracks falls within a region of interest.
Relevant to this thesis is the reconstruction of Λ^0 particles. The *standard* collection of Λ^0 particles, for analyses, involves merging the results from the `V0Finder` module with those from the default `basf2` particle combiner module (which uses the track finding algorithms discussed earlier). These standard Λ^0 particles are reconstructed from the combination of oppositely charged proton and pion tracks that pass a vertex fit (`TreeFit`) with $\chi^2 > 0$. The invariant mass range is required to be within $1.10\,\mathrm{GeV/c^2} < M < 1.13\,\mathrm{GeV/c^2}$.

4.5. Mode Reconstruction

The reconstruction of a mode, i.e., a decay channel, follows a bottom-up approach where the last particles in the decay chain are collected first: tracks with a given final-state particle hypothesis are stored in a list, this list is called a particle list. The particle lists are then combined by the particle combiner module of `basf2` to form the parent particle. The charge conjugates of each track are also saved to the list, thus the anti-particle parent is implied throughout the entire reconstruction.
To illustrate this, in the case of $\Lambda_c^+ \to pK^-\pi^+$, the combinations of protons, kaons, and pions are selected such that the kaon list has an opposite charged track to that of the proton and pion lists. Before the protons, kaons, and pions are combined, they may be required to fulfill a set of impact parameter conditions (i.e. track parameter conditions and limits on the number of hits in the detector layers) and/or pass a minimal threshold in their identification likelihood ratios (PID cuts). Only those combinations that pass the selection criteria—which may furthermore be constrained by kinematic cuts and vertex-fits of the mother—are saved to a candidate list for further analysis.
Naturally, not every combination corresponds to a signal event. In the case of reconstructed MC events, combinations that pass the selection criteria and are not matched to a generated signal event are referred to as combinatorial background events.

A selection criterion or cut that is too tight may bias the results of the analysis, and a cut that is too wide may lead to an overwhelming amount of unwanted events. Thus, it is instructive to undergo the reconstruction with loose[2] cuts that are based on some level of knowledge of the particle (chain) being reconstructed. For example, a suitable reference for the mass selection window for $\Lambda_c^+ \to pK^-\pi^+$ is the world average documented by the PDG, $M(\Lambda_c)_{\mathrm{PDG}} = 2286.46\,\mathrm{MeV}$ [6]. However, as the resolution of the Belle II detector is limited, we require that the total invariant mass of the combination of the *daughters* (products of the mother particle) is large enough to accommodate the tails of the reconstructed signal distribution. In practice, the mass window is chosen even wider to include *sideband* regions, defined as regions neighboring the signal distribution, allowing us to model the background behavior.

4.6. From MC to Data

For each MC sample used in our analysis, there exists a corresponding (real) data set. The analysis leading up to our final candidate selection is carried out on MC samples; a comparison to data (and measurement) is done only as a final step in the analysis process. Each MC sample has about 4× as much integrated luminosity as its data equivalent, which means that for a comparison to data, the MC distributions must be scaled by a factor

$$l_{\mathrm{scale}} = \frac{\mathcal{L}_{\mathrm{int,\ data}}}{\mathcal{L}_{\mathrm{int,\ MC}}}. \tag{4.9}$$

In addition to the scaling factor, other corrections may be employed (on MC) that are related to the signal generation and the particle identification of the daughters.

4.7. Performance Metrics

Using the MC-truth information of the MC sample, the discriminating variables (e.g. kinematic variables and PID information) can be optimized to select a signal region with high statistical significance. A powerful metric for the evaluation of a selection performance is the figure of merit (FOM), which we define as the significance of the signal, [61]

$$\mathrm{FOM} = \frac{N_{\mathrm{sig}}}{\sigma(N_{\mathrm{sig}})} = \frac{N_{\mathrm{sig}}}{\sqrt{N_{\mathrm{sig}} + N_{\mathrm{bkg}} + \sigma^2(N_{\mathrm{bkg}})}} = \frac{N_{\mathrm{sig}}}{\sqrt{N_{\mathrm{sig}} + N_{\mathrm{bkg}}}}, \tag{4.10}$$

where N_{sig} stands for the number of correctly reconstructed signal events (true-matched events), N_{bkg} stands for the number of background events (unmatched events), and σ represents the standard deviation. In principle, the FOM measures the number of standard deviations away from zero assuming a Poisson error ($\sqrt{N_{\mathrm{sig}} + N_{\mathrm{bkg}}}$). This measure is taken on candidates found in a given selection window in the specified MC sample. Note that in the final step of Eq. (4.10), we assume a large enough MC sample to neglect the uncertainty in the expected number of MC background events.[3]

[2] A cut that retains most of the signal events while excluding unwanted regions.

[3] In general, the analytic form of the figure of merit may vary for different types of analyses.

In practice, a cut is chosen at or near the maximum FOM value for a variable of interest. Other useful metrics that relate to the FOM analysis are the purity, the signal efficiency, the background rejection, and the MC efficiency.
The purity signifies the ratio between the signal and the number of candidates in the sample selection,

$$\text{purity} = \frac{N_{\text{sig}}}{N_{\text{sig}} + N_{\text{bkg}}}. \tag{4.11}$$

The signal efficiency captures the retention of the number of true-matched events in the sample for every new selective cut,

$$\text{signal efficiency} = \frac{\#\text{ true-matched events AFTER new selection}}{\#\text{ true-matched events BEFORE new selection}}. \tag{4.12}$$

Complementary to the signal efficiency is the background rejection,

$$\text{background rejection} = 1 - \frac{\#\text{ unmatched events AFTER new selection}}{\#\text{ unmatched events BEFORE new selection}}. \tag{4.13}$$

Lastly, the MC efficiency expresses the total efficiency in the MC sample, it is defined as the ratio between the correctly reconstructed signal (true-matched events) and the total number of generated signal MC particles (true MC events),

$$\text{MC efficiency} = \frac{\#\text{ true-matched events}}{\#\text{ true MC events}}. \tag{4.14}$$

4.8. Fits and Signal Extraction

Beyond maximizing the signal significance by tightening a selection window, we can more precisely extract the signal yield from data by fitting an adequate model to its distributions. The fit model may involve one or more Probability Distribution Functions (PDFs) that depend on unknown parameters for which *estimator* functions provide an estimate of their best values.
A *good* estimator is one which performs in accordance with the following properties [62].

- It is consistent, i.e., it converges to the true parameter values of the model as the number of measurements go to infinity.
- The variance of the (consistent) estimator has a lower bound (the Cramer and Rao variance [62, p. 86]).
- The bias, i.e., the expectation value of the difference between the estimate and its true value, goes to zero as the number of measurements go to infinity.

A *maximum likelihood* estimator has these properties. The maximum likelihood method involves the extraction of best parameter values from the maximum of a likelihood function.

4.8.1. Likelihood Function

A likelihood function is composed of the PDFs that model the distribution of observables in a sample. Given a PDF with m unknown parameters $\mathbf{a} = (a^1, a^2, ..., a^m)$ and a sample composed of N independent experiments, where each experiment involves the measurement of l random variables $x^i = (x^i_1, x^i_2, ..., x^i_l)$ distributed according to the same PDF, the likelihood function reads

$$L(\mathbf{x}|\mathbf{a}) = \prod_{i=1}^{N} \mathrm{PDF}(x^i|\mathbf{a}), \qquad \mathbf{x} = \{x^1, x^2, ..., x^N\}. \tag{4.15}$$

The maximization of the likelihood function is more easily tractable by minimizing its negative logarithm,

$$-\ln L(\mathbf{x}|\mathbf{a}) = -\sum_{i=1}^{N} \ln \mathrm{PDF}(x^i|\mathbf{a}) \tag{4.16}$$

such that the maximum likelihood parameter estimates $\hat{\mathbf{a}}$ are retrieved by solving the set of equations given by

$$\frac{\partial(-\ln L(\mathbf{x}|\mathbf{a}))}{\partial a^i} = 0 \quad \forall i. \tag{4.17}$$

Due to the high complexity of these equations, they are often solved using computational algorithms such as those implemented in the `RooFit` toolkit [63] of the CERN's ROOT environment.

4.8.2. Extended Likelihood Function

The extended likelihood function is a likelihood function like Eq. (4.15) but is normalized by a Poisson distributed term with average $\mu(\mathbf{a})$, where the total number of events N is itself to be estimated,

$$L(\mathbf{x}|\mu, \mathbf{a}) = \underbrace{\frac{\mu(\mathbf{a})^N e^{-\mu(\mathbf{a})}}{N!}}_{\text{Poisson Norm.}} \prod_{i=1}^{N} \mathrm{PDF}(x^i|\mathbf{a}). \tag{4.18}$$

Thus, the maximization of this extended likelihood function not only determines the shape of the sample distribution but also its size [64].
For example, given a PDF with signal and background components, as is the case when fitting over MC distributions with truth information, the number of yield events can be expressed as $\mu = n_s + n_b$, where n_s is the number of signal yields and n_b is the number of background yields. The (normalized) PDF takes the form

$$\mathrm{PDF} = \frac{n_s}{n_s + n_b}\mathrm{PDF}_s + \frac{n_b}{n_s + n_b}\mathrm{PDF}_b, \tag{4.19}$$

where PDF_s models the signal distribution and PDF_b models the background distribution. Thus, the extended likelihood function becomes [62]

$$L(\mathbf{x}|n_s, n_b, \mathbf{a}) = \frac{e^{-(n_s+n_b)}}{N!} \prod_{i=1}^{N} \left(n_s \mathrm{PDF}_s(x^i|\mathbf{a}) + n_b \mathrm{PDF}_b(x^i|\mathbf{a})\right). \tag{4.20}$$

As previously indicated, the maximum likelihood parameters $\hat{\mathbf{a}}$ are in practice extracted from the minimization of the negative logarithm,

$$-\ln L(\mathbf{x}|n_s, n_b, \mathbf{a}) = n_s + n_b + \sum_{i=1}^{N} \ln\left(n_s \mathrm{PDF}_s(x^i|\mathbf{a}) + n_b \mathrm{PDF}_b(x^i|\mathbf{a})\right) - \ln N!, \tag{4.21}$$

where the last term $(-\ln N!)$ becomes irrelevant to the minimization process as it is a constant w.r.t. infinitesimal changes of the PDF parameters $\mathbf{a}$.

In this thesis, we employ an extended maximum likelihood fit using `RooFit` to simultaneously retrieve the PDF parameters and the signal (and background) yields for each of our fitted sample distributions.
The performance of the fit is visually inspected in reference to `RooFit`'s χ^2 value. This value is measured between the plotted PDF and the distributed data[4]. A value of χ^2/ndf that is near the value of 1, where ndf stands for the number of degrees of freedom[5], serves as an indicator of a good fit in our analysis.
For a general discussion of the χ^2-statistic in reference to the (ratio of) maximum likelihood estimators, see [65] and [62, p. 99].

[4]See the ROOT Reference Guide documentation for its modular definition.

[5]The number of degrees of freedom is the number of measured events minus the number of fitted parameters.

5. Analysis of Λ_c^+

In this chapter, we extract signal candidates of $\Lambda_c^+ \to pK^-\pi^+$ in bins of the scaled momentum x_p, defined as

$$x_p = \frac{p^* c}{\sqrt{\frac{s}{4} - c^2 M^2}}, \tag{5.1}$$

where M is the invariant mass of the mother particle Λ_c^+, p^* is its momentum in the e^+e^- rest frame and s is the Mandelstam variable denoting the square of the total available energy from the e^+e^- collision, such that $\sqrt{s} = 10.58\,\mathrm{GeV}$.

5.1. Data and MC Samples

For the study of $\Lambda_c^+ \to pK^-\pi^+$, we use two run-dependent[1] MC samples, one with an integrated luminosity of $14.96\,\mathrm{fb}^{-1}$ (exp20) and the other with $65.52\,\mathrm{fb}^{-1}$ (exp14). Each MC sample corresponds to data collected from the year 2019 to 2021 at the $\Upsilon(4S)$ energy, see table 5.1. The candidate events are reconstructed using the `basf2` release version `light-2311-nebelung`.

5.2. Strategy

We first reconstruct $\Lambda_c^+ \to pK^-\pi^+$ candidates found in $c\overline{c}$ and $B\overline{B}$ events using the $14.96\,\mathrm{fb}^{-1}$ MC sample. This small sample serves to illustrate the mass distribution of $\Lambda_c^+ \to pK^-\pi^+$ using only impact parameters and a vertex fit. For this type of reconstruction, where no PID cuts are applied, the small MC sample is used (instead of the large MC sample) to illustrate the significance of the following optimizations. We apply PID cuts on the daughter tracks (p, K, π) and outline the signal efficiency of each selection. Using the selection criteria obtained from the small sample, we continue the analysis on the larger $65.52\,\mathrm{fb}^{-1}$ MC sample, which is the main sample studied. In this sample, we include $\Lambda_c^+ \to pK^-\pi^+$ candidates from $u\overline{u}$, $d\overline{d}$, $s\overline{s}$, $c\overline{c}$, and $B\overline{B}$ events, and work on other tight selections. After determining the final cuts, which are summarized in table 5.4, we extract the signal yields from data in bins of x_p. Finally, the shape of the x_p distribution in MC is compared to data and a few critical observations are made, which are considered in the study of the $\Xi_c^{0,+}$ particles in chapter 6.

[1] Calibrated to the run dependence of the corresponding collection of data, i.e., with luminosity and beam background adjustments for the runs. The run-dependent MC samples used here are internally denoted as "MC15rd".

MC sample (MC15rd)	MC event type	data equivalent	exp#
$14.96\,\mathrm{fb}^{-1}$	$c\bar{c}$, $B\bar{B}$	$3.79\,\mathrm{fb}^{-1}$ (bucket26)	20
$65.52\,\mathrm{fb}^{-1}$	$u\bar{u}$, $d\bar{d}$, $s\bar{s}$, $c\bar{c}$, $B\bar{B}$	$16.50\,\mathrm{fb}^{-1}$ (proc13-chunk3)	14

Table 5.1.: Data and MC samples used for the analysis of $\Lambda_c^+ \to pK^-\pi^+$. The event types are the primary on-resonance channels, e.g., $e^+e^- \to c\bar{c}$ at the $\Upsilon(4S)$ energy, from which we reconstruct Λ_c^+ candidates.

	PXD hits	1st SVD layer hits	CDC hits	dr	$\lvert dz\rvert$
p,K,π	≥ 1	≥ 1	≥ 20	< 0.5 cm	< 2 cm

Table 5.2.: Impact parameter conditions used in the reconstruction of Λ_c^+.

As mentioned in Sec. 4.5, the charge conjugates are considered simultaneously. Since we do not differentiate between the charge states of $\Lambda_c^\pm$, we simply refer to it as Λ_c^+. Thus, our candidate selection for Λ_c^+ applies equally to the charge conjugate candidates Λ_c^-.

5.3. Candidate Selection

Our goal is to prepare a sample of candidates with optimal signal significance. The first step to achieve this, is to reconstruct $\Lambda_c^+ \to pK^-\pi^+$ events with loose cuts, by which we retain as many interesting events as possible while simultaneously rejecting unrelated events.

5.3.1. Reconstruction with Loose Cuts

Given that the lifetime of Λ_c^+ is short (203 fs [6, 66]) and its production from heavy quark fragmentations is favorable, we require the charged tracks (p, K and π) to originate from a common production vertex found near the IP. The selected tracks have a transverse distance $dr := |d_0| < 0.5\,\mathrm{cm}$ and have a beam-parallel component $|dz| < 2\,\mathrm{cm}$ with respect to the IP. In agreement with the impact parameter conditions applied in [66], we avoid beam-related background events and refine the track reconstruction by requiring at least a hit in the PXD, at least a hit in the first layer of the SVD, and at least 20 hits in the CDC. These impact parameter conditions are summarized in table 5.2. Moreover, the production vertex of the mother is fitted with `TreeFit` where a minimal χ^2 confidence level of 1% is required.
Using the small MC sample ($14.96\,\mathrm{fb}^{-1}$), we reconstruct $\Lambda_c^+ \to pK^-\pi^+$ candidates from $c\bar{c}$ and $B\bar{B}$ events in the invariant mass range $2.24\,\mathrm{GeV} < M(pK^-\pi^+) < 2.34\,\mathrm{GeV}$, with all the previously mentioned conditions applied. The MC efficiency of this candidate sample is 30% and corresponds to 48 thousand signal events. As seen in the mass distribution shown in Fig. 5.1(a), this candidate sample is dominated by background events. In the next step, we improve our selection by optimizing the FOM, $N_{\mathrm{sig}}/\sqrt{N_{\mathrm{sig}} + N_{\mathrm{bkg}}}$, to the

Selection	N_{sig}	sig eff. [%]	bkg rej. [%]	FOM
impact parameters (table 5.2), vertex fit ($\chi^2 > 0.01$), $2.24\,\text{GeV} < M(pK^-\pi^+) < 2.34\,\text{GeV}$	47818	100	-	5
$\text{proton}_{ID} > 0.7$	42328	89	98	34
$\text{kaon}_{ID} > 0.1$	39131	92	86	78
$\text{pion}_{ID} > 0.1$	35298	90	24	80

Table 5.3.: Number of signal events (N_{sig}), signal efficiency (sig eff.), background rejection (bkg rej.) and FOM for each consecutive selection of candidates from the small MC sample ($14.96\,\text{fb}^{-1}$). Note that the starting point of the signal efficiency is defined as 100% for the number of reconstructed signal candidates.

PIDs associated with the selected tracks.

5.3.2. PID Optimizations

Due to the low relative abundance of protons produced at Belle II with respect to other charged particles, optimizing the FOM for the proton global PID of the proton track[2], which we refer to as proton_{ID}, can have an immense impact on background rejection. As portrayed in Fig. 5.1(b), a maximum FOM value for the proton_{ID} is found above 0.7. Requiring

$$\boxed{\text{proton}_{ID} > 0.7} \tag{5.2}$$

retains 89% of the reconstructed signal while rejecting 98% of the combined $c\bar{c}$ and $B\bar{B}$ background. This effect is shown in Fig. 5.1(c), where in comparison to Fig. 5.1(a), the background falls to an almost flat level.
Similarly, from the optimization of the FOM for the kaon global PID of the kaon track, we require

$$\boxed{\text{kaon}_{ID} > 0.1\ .} \tag{5.3}$$

With this subsequent cut, we retain 92% of the remaining signal and remove another 86% of the combined $c\bar{c}$ and $B\bar{B}$ background. In the case of the pion track, we simply apply the loose cut

$$\boxed{\text{pion}_{ID} > 0.1\ ,} \tag{5.4}$$

where we retain 90% of the remaining signal and remove another 24% of the combined $c\bar{c}$ and $B\bar{B}$ background.
The number of signal candidates, the signal efficiency, the background rejection and the FOM value for each consecutive PID cut are summarized in table 5.3.

[2] As defined in Sec. 4.1.2, the global identification of a particle X is defined as the ratio of the likelihood for a track to be of particle type X and the sum of all the charged particle likelihoods.

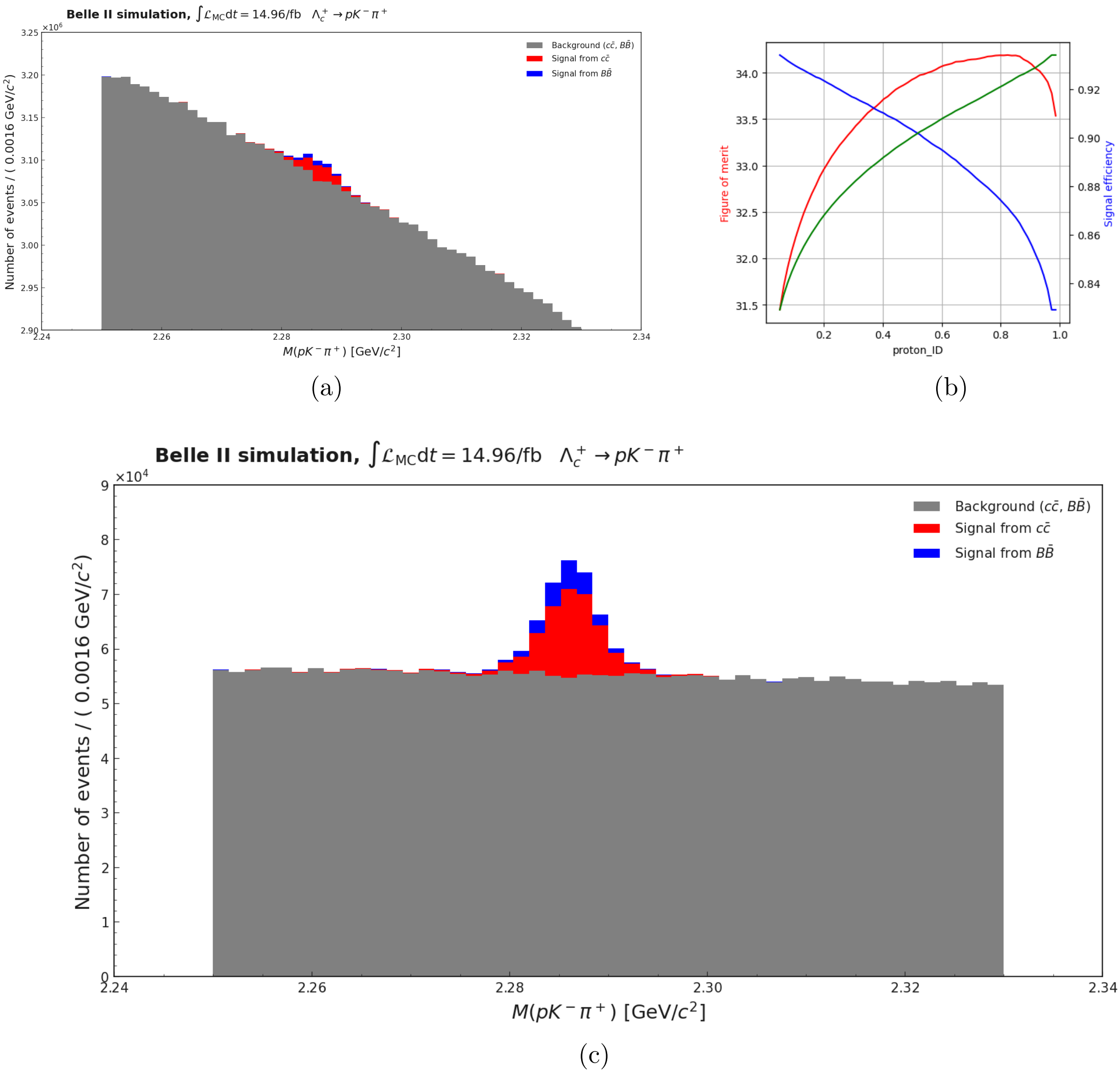

Figure 5.1.: Shown in (a) is the mass distribution of reconstructed Λ_c^+ events with the conditions discussed in Sec. 5.3.1. Note that the displayed y-axis starts at 2.9 million events per bin. In (b), the behavior of the FOM, signal efficiency and purity in the signal region are shown as functions of the proton$_{ID}$. Shown in (c) is the mass distribution of Λ_c^+ after applying the PID cut, proton$_{ID} > 0.7$.

We now continue the analysis on the larger MC sample (65.52 fb^{-1}), where we also include events from $u\bar{u}$, $d\bar{d}$, and $s\bar{s}$ fragmentations. We study candidates in the large MC sample starting with the same selection criteria as shown in table 5.3 except for a tighter Λ_c^+ mass region, 2.273 GeV < $M(pK^-\pi^+)$ < 2.297 GeV. The MC efficiency of this refined candidate sample is 23%, corresponding to 159782 signal candidates.

5.3.3. Vetoed Events

Pions coming from D-meson decays can pass our selection criteria as misidentified protons. We identify this background by giving the proton track in $\Lambda_c^+ \to pK^-\pi^+$ a pion mass hypothesis. As shown in Fig. 5.2, the mass distribution $M(\pi^+K^-\pi^+)$ contains peaks mostly originating from the $c\bar{c}$ background. On the more massive region (right shaded interval), the peak formation corresponds to decays from (excited) D^* mesons [66].
Events in the range

$$\boxed{1.86\,\mathrm{GeV/c^2} < M(\pi^+K^-\pi^+) < 1.88\,\mathrm{GeV/c^2}} \tag{5.5}$$

and those in the range

$$\boxed{2.00\,\mathrm{GeV/c^2} < M(\pi^+K^-\pi^+) < 2.02\,\mathrm{GeV/c^2}} \tag{5.6}$$

corresponding to roughly 3× the width of each peak are removed from our list of candidates. The veto retains 93% of the signal candidates corresponding to the 65.52 fb^{-1} MC sample and rejects 7% of the background. The MC efficiency falls to 21%.

5.3.4. Transverse Momentum Cut on the Proton Track

A cut on kinematic variables associated with the proton track is another useful approach that can aid in suppressing background events from $\Lambda_c^+ \to pK^-\pi^+$ candidates. In Fig. 5.3, we show the FOM behavior of proton_{p_T}, which stands for the transverse momentum of the proton track in the laboratory frame. An optimal FOM value is found for $\mathrm{proton}_{p_T} > 0.3$ GeV/c. With this consecutive cut, we retain 99% of the signal candidates and reject 5% of the background; the MC efficiency remains near 21%.

5.3.5. Pion Momentum Cut

As we strive to reduce the discrepancies in the distribution shapes seen in MC versus those seen in data, we use the Belle II Systematic Corrections Framework, introduced in Sec. 4.2. Using the framework, we apply PID efficiency correction weights to each charged track of $\Lambda_c^+ \to pK^-\pi^+$. The (θ, p) parameter regime covered by these systematic corrections—applied to our 65.52 fb^{-1} MC sample under the conditions established up to this point—is shown in Appendix B.1.
The PID efficiency correction factors are well suited for the proton and the kaon candidates, but not the pion. Thus, in addition to the previous cuts, we require a cut on the

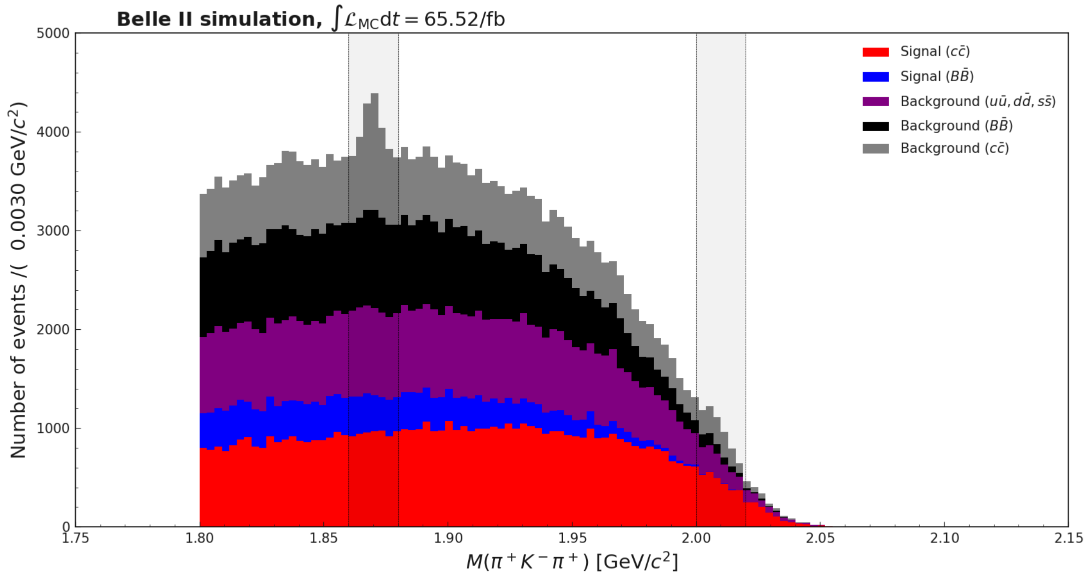

Figure 5.2.: Plot of the $M(\pi^+K^-\pi^+)$ distribution, where the proton has been given a pion mass hypothesis. The shaded intervals indicate the vetoed regions. Note that the signal and background distributions are stacked per event type, where the background from the light-quark pairs is combined.

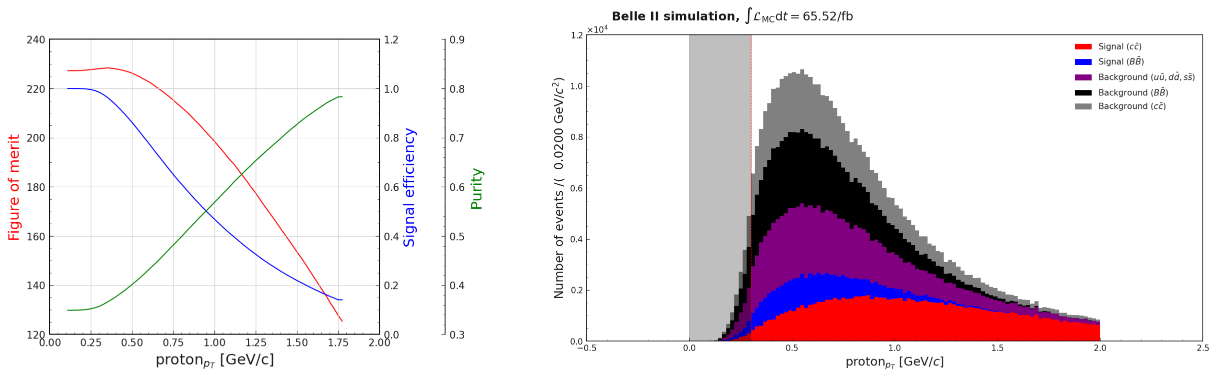

(a) (b)

Figure 5.3.: In (a), the FOM, signal efficiency and purity plot of the Λ_c^+ candidates as functions of the proton transverse momentum. In (b), the distribution of transverse momentum of the proton. The red vertical line indicates the start of the region for which proton$_{p_T} > 0.3$, such that every candidate in the grayed out region is removed from the candidate sample.

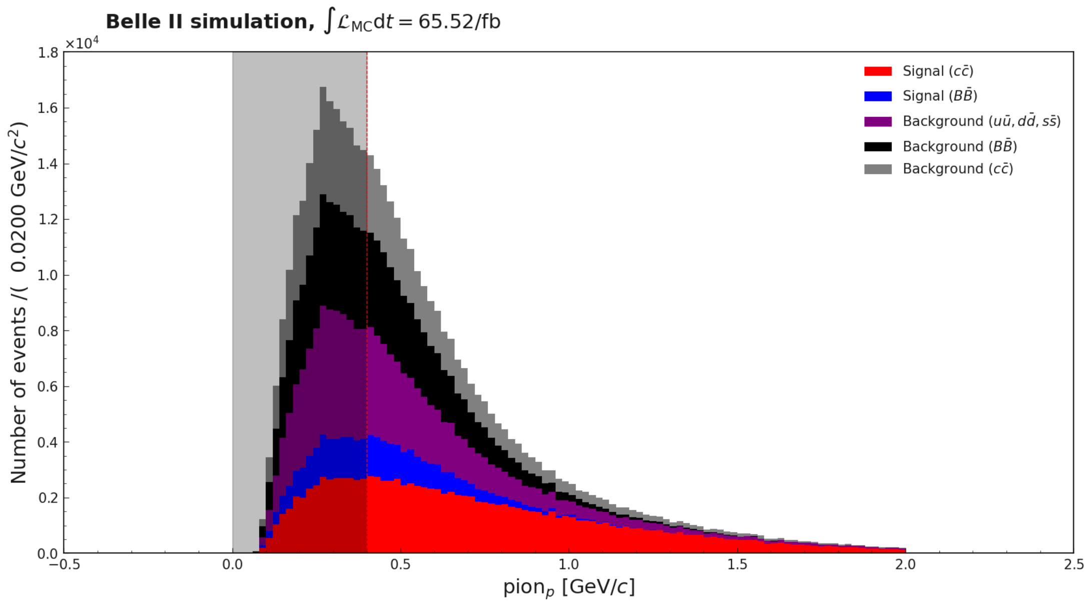

Figure 5.4.: Pion momentum distribution. The grayed out region indicates the cut spectrum motivated by the PID correction weights analysis, only candidates where $pion_p > 0.4$ GeV/c are kept.

momentum of the pion, such that $pion_p > 0.4$ GeV/c. The pion momentum distribution including the cut spectrum is shown in Fig. 5.4.
With this significant cut, we retain 70% of the signal candidates and reject 48% of the background; the MC efficiency falls to 15%.

5.3.6. Final Selection Summary

In table 5.4, we summarize our final selection criteria for $\Lambda_c^+ \to pK^-\pi^+$ candidates.[3]

Selection	N_{sig}	sig eff. [%]	bkg rej. [%]	MC eff. [%]
impact parameters (table 5.2), vertex fit ($\chi^2 > 0.01$), $2.273\,\text{GeV} < M(pK^-\pi^+) < 2.297\,\text{GeV}$ $\text{proton}_{ID} > 0.7$ $\text{kaon}_{ID} > 0.1$ $\text{pion}_{ID} > 0.1$	159782	100	-	23.0
$M(\pi^+K^-\pi^+)$ vetos	147873	92.5	7.2	21.3
$\text{proton}_{pT} > 0.3\,\text{GeV/c}$	145699	98.5	4.8	21.0
$\text{pion}_{p} > 0.4\,\text{GeV/c}$	101820	69.9	48.1	14.7

Table 5.4.: Summary of the final criteria for selecting $\Lambda_c^+ \to pK^-\pi^+$ candidates. The number of signal events (N_{sig}), signal efficiency (sig eff.), background rejection (bkg rej.) and MC efficiency (MC eff.) are given for each consecutive selection made for candidates in the large MC sample ($65.52\,\text{fb}^{-1}$). Note that the starting point of the signal efficiency is defined as 100% for the number of reconstructed signal candidates.

[3] A general check on our selection criteria are "N-1" plots, where the distribution of candidates are plotted for each cut variable with all the cuts applied except for the one plotted. These plots are provided in Appendix B.2.

5.4. x_p Distribution

Having determined our final selection of candidates using the MC samples, we draw our attention to the x_p distribution of Λ_c^+ events in data. We first discuss the extraction of signal yields in the data, then discuss the MC efficiency corrections. Finally, we compare the shapes of the generated signal MC to the obtained data yields.
In a similar approach as done for Belle data [67], we extract the yield in bins of x_p by performing a mass fit in each bin. The size of each bin is chosen to be 0.05, i.e., we study 20 x_p-dependent bins in the total range $x_p \in (0, 1]$.

5.4.1. x_p-independent mass fit

Before mass-fitting the individual x_p-dependent bins, an x_p-independent mass fit is performed over the optimized data using a double Gaussian PDF (to model the signal peak)[4] and an exponential PDF (to model the background). The combination of both PDFs forms the total PDF which is used to fit over the mass distribution in data.
The analytic form of the double Gaussian $\mathrm{PDF}_{\mathrm{signal}}(m)$, as a function of the mass value m, reads

$$\mathrm{PDF}_{\mathrm{signal}}(m) = w_{\mathrm{tail}} \times \frac{1}{\sqrt{2\pi\sigma_1^2}} e^{-\frac{(m-\mu)^2}{2\sigma_1^2}} + w_{\mathrm{core}} \times \frac{1}{\sqrt{2\pi\sigma_2^2}} e^{-\frac{(m-\mu)^2}{2\sigma_2^2}} \tag{5.7}$$

where μ is the mean value of the distribution and $\sigma_{1,2}$ its width. w_{tail} and w_{core} are weight factors for each Gaussian component and act as the normalization factors of the double Gaussian PDF. Here, $w_{\mathrm{tail}} + w_{\mathrm{core}} = 1$. The exponential function reads

$$\mathrm{PDF}_{\mathrm{background}}(m) = N \times e^{\tau \cdot m}, \tag{5.8}$$

where N is a normalization constant and τ represents the slope parameter of the exponential function.
The total PDF fit over the mass distribution in data performs well, as seen in Fig. 5.5, where $\chi^2_{/\mathrm{ndf}} = 1.16$. In this fit, all the fit parameters are floated. The extracted width values are

$$\sigma_1 = (5.43 \pm 0.36)\mathrm{MeV/c^2} \tag{5.9}$$

and

$$\sigma_2 = (2.28 \pm 0.05)\mathrm{MeV/c^2}, \tag{5.10}$$

where the former accounts for the tails of the Gaussian distribution and the latter represents the core width.
Notably, prior to the fit of the mass distribution in data, a fit was performed on the mass distribution in MC, similarly, with all fit parameters floated. The PDF shape chosen for the fit to data thus originates directly from the behavior observed in MC. The widths obtained from the fit to MC are $\sigma_1 = (5.97 \pm 0.15)\mathrm{MeV/c^2}$ and $\sigma_2 = (2.43 \pm 0.02)\mathrm{MeV/c^2}$,

[4] We use a double Gaussian PDF to account for the tails of the peaking structure.

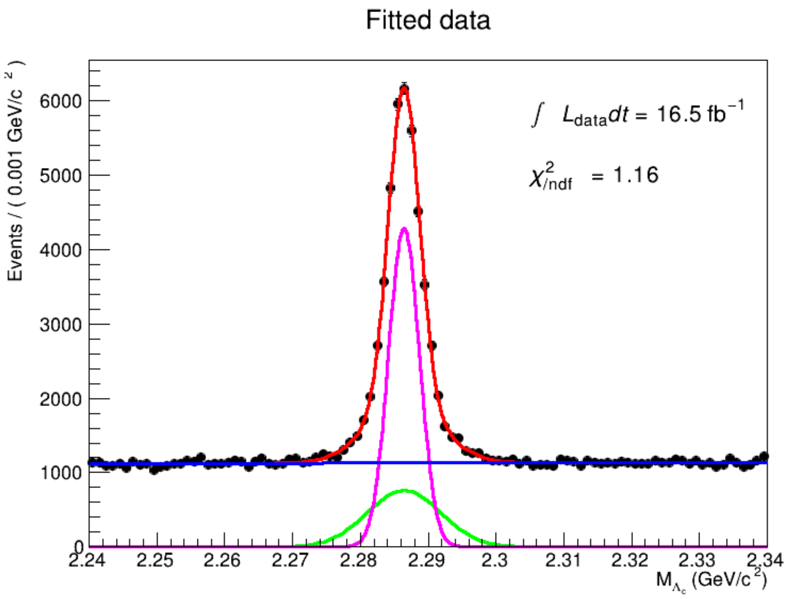

(a)

Figure 5.5.: A double Gaussian PDF fitted over the x_p-independent mass distribution in data. The green curve and the magenta curve represent the two Gaussians composing the double Gaussian PDF with the widths σ_1 and σ_2, respectively. The blue curve represents the fit to the background distribution using the exponential function. The red curve represents the total fit to the mass distribution.

which are marginally consistent with the widths obtained in data at 1.6σ agreement, where σ represents the combined uncertainties of both width results[5]. However, aside from the PDF choice, no direct inputs from MC were used in the fit to the data.
Moreover, to identify any strong dependencies of the widths (σ_1 and σ_2) on the type of fragmentation, the MC fit was performed separately on $B\overline{B}$ events and continuum ($u\overline{u}$, $d\overline{d}$, $s\overline{s}$, $c\overline{c}$) events. In the continuum case, only $c\overline{c}$ contributes to the signal distribution. The width results are found to agree within 1.4σ, thus no strong dependence of the Gaussian distribution width as a function of x_p is seen; as elaborated next, $B\overline{B}$ events and $c\overline{c}$ events separate in the x_p spectrum.

5.4.2. x_p-dependent mass fits

We fix the widths in Eq. (5.9) and Eq. (5.10) to their nominal values and use them as inputs for the likewise double Gaussian PDF used for the mass fits of each x_p-dependent bin. The backgrounds are, as before, fitted with the exponential PDF (no fixed parameters). The mass fits, number of events, and the χ^2/ndf values, are illustrated in Fig. 5.6 for each of the 20 x_p-dependent bins.
From Fig. 5.6(i) to Fig. 5.6(t) corresponding to $0.4 < x_p \leq 1$, we see that the background level is greatly diminished in comparison to bins for which $x_p \leq 0.4$. This overall behavior

[5]To compare the widths, σ_1 and σ_2 are combined such that $\sigma_{\mathrm{total}} = \sqrt{\sigma_1^2 + \sigma_2^2}$.

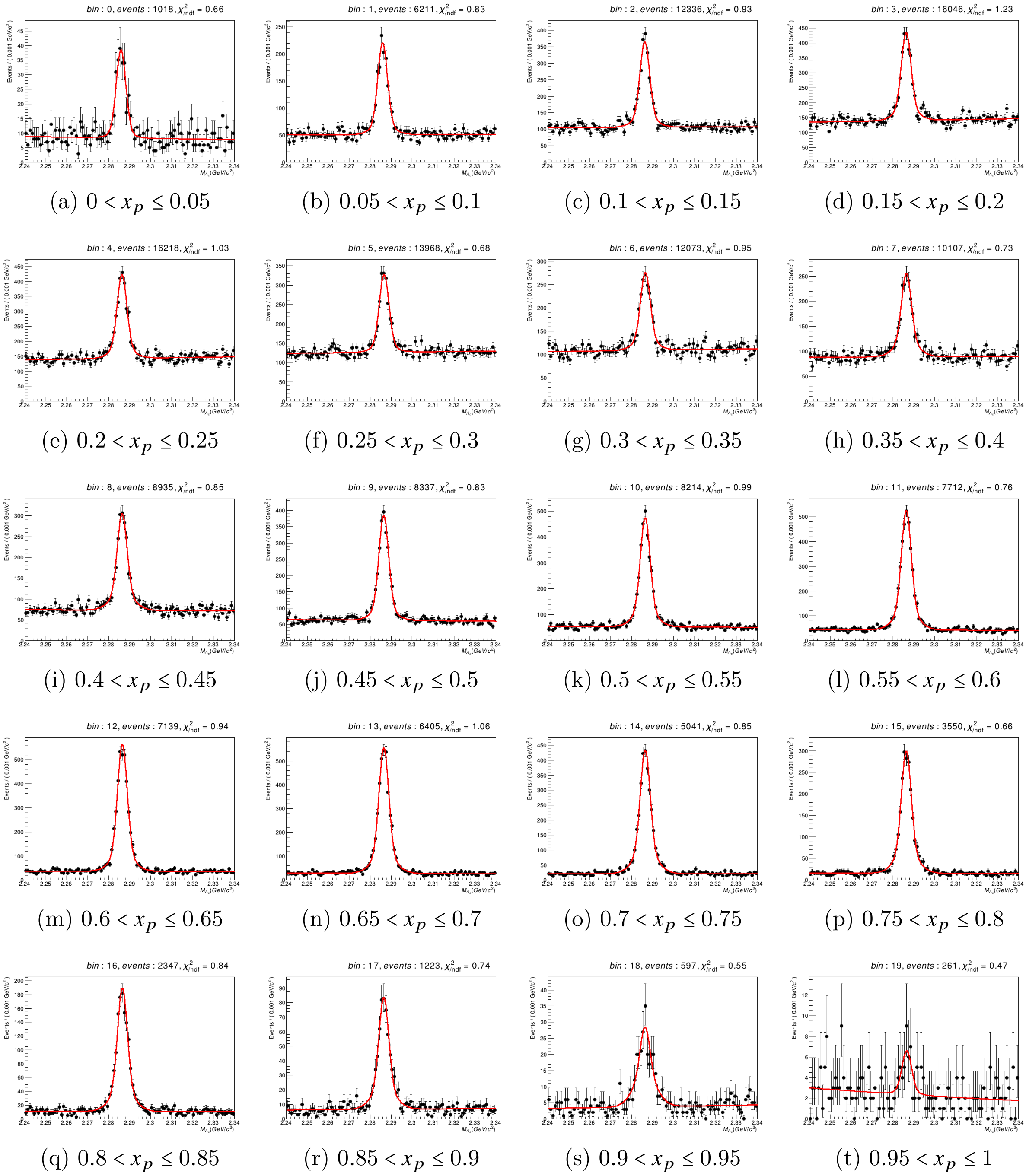

(a) $0 < x_p \leq 0.05$ (b) $0.05 < x_p \leq 0.1$ (c) $0.1 < x_p \leq 0.15$ (d) $0.15 < x_p \leq 0.2$

(e) $0.2 < x_p \leq 0.25$ (f) $0.25 < x_p \leq 0.3$ (g) $0.3 < x_p \leq 0.35$ (h) $0.35 < x_p \leq 0.4$

(i) $0.4 < x_p \leq 0.45$ (j) $0.45 < x_p \leq 0.5$ (k) $0.5 < x_p \leq 0.55$ (l) $0.55 < x_p \leq 0.6$

(m) $0.6 < x_p \leq 0.65$ (n) $0.65 < x_p \leq 0.7$ (o) $0.7 < x_p \leq 0.75$ (p) $0.75 < x_p \leq 0.8$

(q) $0.8 < x_p \leq 0.85$ (r) $0.85 < x_p \leq 0.9$ (s) $0.9 < x_p \leq 0.95$ (t) $0.95 < x_p \leq 1$

Figure 5.6.: Λ_c^+ mass fits per x_p-bin in data.

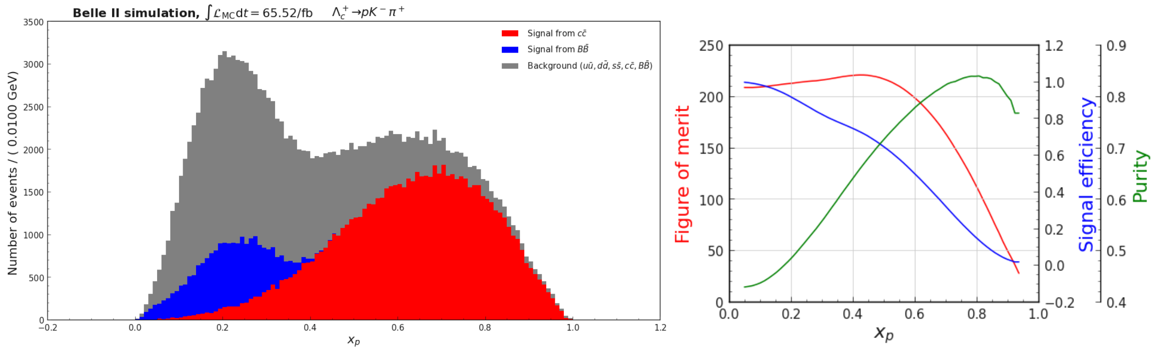

(a) (b)

Figure 5.7.: In (a), an overview of the x_p distribution in the MC sample. In (b), the signal efficiency, purity and FOM over x_p. We see that for $x_p > 0.4$, the signal to background ratio increases, as similarly seen in the overall behavior of the x_p-dependent mass fits of the data in Fig. 5.6.

is seen in the MC sample distribution of x_p. In Fig. 5.7, we show the x_p distribution of $\Lambda_c^+ \to pK^-\pi^+$ candidates within the signal region, $2.279\,\mathrm{GeV} < M(\Lambda_c^+) < 2.294\,\mathrm{GeV}$, defined as three standard deviations of the mean of the true-matched Gaussian distribution.
Notably, the same procedure was applied to the mass distribution of MC, where the widths from the x_p-independent mass fit were fixed and used in the fits to the 20 x_p-bins. The signal yield was found to be consistent with the number of true-matched events per respective x_p-bin.

5.4.3. Efficiency corrected yields

Having fitted the x_p-dependent mass distributions, we compare the shape of the generated signal MC to the shape formed by the data yields, in bins of x_p. To this end, we scale down the MC events by the data luminosity,

$$l_{\mathrm{scale}} = \frac{16.50\,\mathrm{fb}^{-1}}{65.52\,\mathrm{fb}^{-1}} = 0.252, \tag{5.11}$$

and correct the data yields by the MC efficiency bin by bin.
For an x_p-bin with index i, where $0 \le i \le 19$ and $i \in \mathbb{Z}$, the efficiency-corrected data yield can be expressed as

$$(\text{data yield})^i = \frac{N^i_{\mathrm{fit}}}{\epsilon^i}. \tag{5.12}$$

N^i_{fit} is the number of yield events per bin captured by the fit to data and ϵ^i is the MC efficiency per bin,

$$\epsilon^i = \frac{\#\text{true-matched events per i-th bin}}{\#\text{true MC events generated in the i-th bin}}. \tag{5.13}$$

5.5. Data/MC shape comparison

In Fig. 5.8, we compare the efficiency-corrected data yields to the luminosity-scaled MC signal generation in bins of x_p. The bin indices and $\chi^2_{/\mathrm{ndf}}$ values shown in Fig. 5.8 refer to the fits shown in Fig. 5.6. Although all known corrections have been applied to candidates in our samples, it is evident that the overall shape of the generated signal MC and the data yields do not overlap well. Not only is there a tendency for a lower signal count per bin in the generated signal distribution but it also appears to be shifted rightwards. This discrepancy has been recently noted by *Longke Li et al.* [68, 69] in internal publications of Belle II. In Appendix C, we present a shape correction method that circumvents the data/MC disagreement in the high x_p spectrum. However, a detailed MC correction is beyond the scope of this thesis, and it is not strictly necessary for the upcoming conclusion. An important observation is that the double peak formation seen in MC is also seen in data, where the left peak corresponds to $B\overline{B}$ signal and the right peak corresponds to $c\overline{c}$ signal. Another interesting observation is that the MC efficiency increases by more than 10% from the low x_p bin ($0 < x_p \leq 0.05$) to the high x_p bin ($0.95 < x_p \leq 1$). In contrast, using Belle data, the MC efficiency of Λ_c^+ events was stated to be constant throughout the entire x_p spectrum [67].

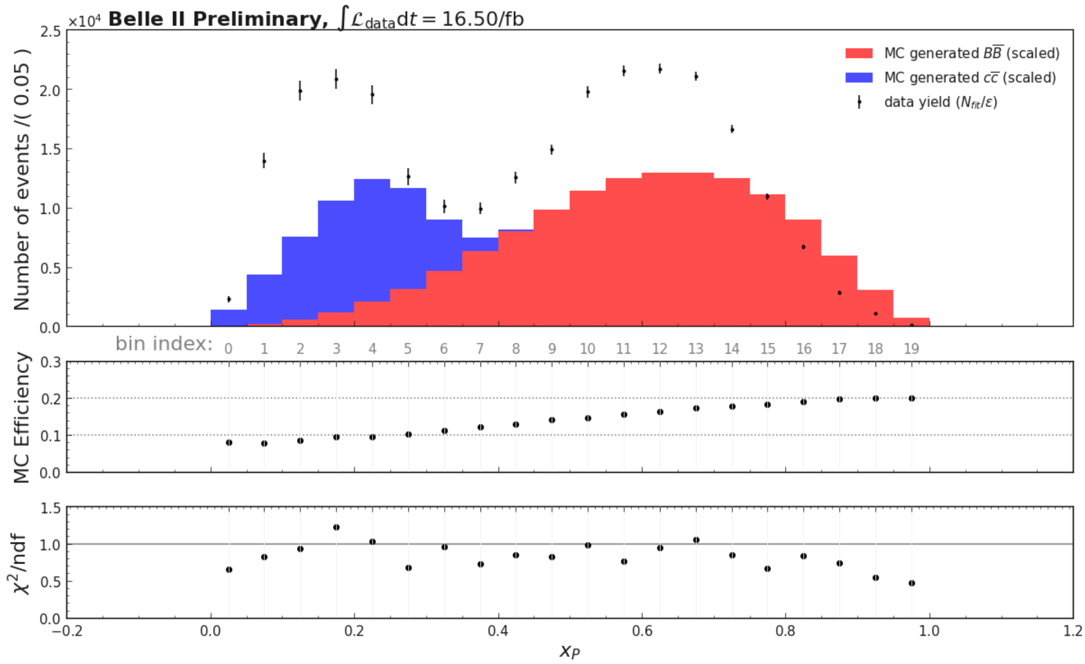

Figure 5.8.: The top plot presents the luminosity-scaled true MC count vs. the efficiency-corrected data yield in bins of x_p. The error bars denote the statistical uncertainty of the fit (scaled for the shape comparison). The middle plot presents the MC efficiency per bin and displays its overall increasing behavior for higher x_p values. The bottom plot presents the $\chi^2_{/\mathrm{ndf}}$ value of the fit to the data.

In summary, building on the 2005 Belle study [67], we have shown that using Belle II data, it is instructive to study Λ_c^+ in the x_p spectrum with $x_p > 0.4$. This regime amplifies the MC efficiency and purity of Λ_c^+ candidates from $c\overline{c}$ fragmentations. Signal events from $B\overline{B}$ decays are rejected, as they are mostly prevalent in the $x_p \leq 0.4$ regime. Indeed, a high x_p cut, or similarly, a high momentum cut, is common practice in the study of charmed baryons. Here, we have re-derived this quality and have illustrated the limitations of the data/MC agreement in the x_p-spectrum using Belle II data. This result is seen in the other weakly decaying charmed baryons, $\Xi_c^{0,+}$, which have similar kinematic properties to that of Λ_c^+.

6. Analysis of $\Xi_c^{0,+}$

In this chapter, we study $\Xi_c^{0,+}$ events found in modes involving hyperons and mesons,

$$\Xi_c^0 \to \Xi^-\pi^+,\ \Lambda^0 K^-\pi^+ \tag{6.1}$$

and

$$\Xi_c^+ \to \Xi^-\pi^+\pi^+,\ \Lambda^0 K^-\pi^+\pi^+, \tag{6.2}$$

with hyperon subdecays, $\Xi^- \to \Lambda^0\pi^-$ and $\Lambda^0 \to p\pi^-$. These modes and their PDG masses are summarized in table 6.1. Since they have similar characteristics, we will discuss them collectively, where applicable. To keep matters simple, we refer to the above collection of $\Xi_c^{0,+}$ modes simply as Ξ_c. Similarly, we refer to the first hyperon daughters of Ξ_c (either Ξ^- or Λ^0) as *primary* hyperons, and the secondary Λ^0 (subdecay of Ξ^-) as the *secondary* hyperon. The kaon and pion tracks, which represent the primary mesons produced in the Ξ_c decays, are referred to as prompt charged tracks.
The specific channels will be explicitly stated when non-overlapping conditions apply.

6.1. Strategy and Overview

Our primary goal is to extract the width and yield from a fit to the mass distribution of Ξ_c signal candidates in data. The yield information forms the basis for the determination of the ratio of branching fractions,

$$\frac{\mathcal{B}(\Xi_c^0 \to \Lambda K^-\pi^+)}{\mathcal{B}(\Xi_c^0 \to \Xi^-\pi^+)} \tag{6.3}$$

and

$$\frac{\mathcal{B}(\Xi_c^+ \to \Lambda K^-\pi^+\pi^+)}{\mathcal{B}(\Xi_c^+ \to \Xi^-\pi^+\pi^+)}, \tag{6.4}$$

which are determined at the end of this chapter.
Motivated by the results of the previous chapter, we limit the reconstruction of Ξ_c to candidates that originate from $c\overline{c}$ fragmentations by requiring $x_p(\Xi_c) > 0.4$. In contrast to the previously studied $\Lambda_c^+ \to pK^-\pi^+$ mode, the multilevel decays in Ξ_c require several optimization iterations before a final selection is achieved.
In Sec. 6.3, we discuss the choice of loose selections on prompt charged tracks and hyperons. The loose selections are summarized in table 6.3. In Sec. 6.4, we optimize the signal significance of the sample candidates by maximizing the FOM of the PID of hyperon daughter tracks and applying cuts to the flight significance L/σ of the hyperons. L denotes the flight length of the hyperon from its production vertex to its decay vertex, as introduced in Sec. 4.3, and σ denotes the uncertainty in the determination of L. At

Mother channels	Charmed baryon PDG mass [MeV/c^2]	Lifetime [fs]
$\Xi_c^0 \to \Xi^-\pi^+$, $\Lambda^0 K^-\pi^+$	2470.44	150
$\Xi_c^+ \to \Xi^-\pi^+\pi^+$, $\Lambda^0 K^-\pi^+\pi^+$	2467.71	453

Hyperon channels	Primary hyperon PDG mass [MeV/c^2]	Lifetime [ps]
$\Xi^- \to [\Lambda^0 \to p\pi^-]\pi^-$	1321.71	164
$\Lambda^0 \to p\pi^-$	1115.68	262

Table 6.1.: List of the Ξ_c channels and their subdecays studied in this chapter. The charge conjugate of each of these modes is implied in the analysis. The (nominal) PDG mass and lifetime values represent the current (2024) world average [6]. Note that the hyperons have a lifetime approximately 1000× longer than the charmed baryons.

the end of the section we establish the final selection criteria for Ξ_c candidates. The final selections are summarized in table 6.6 for Ξ_c^0 candidates and in table 6.7 for Ξ_c^+ candidates. In Sec. 6.5, we fit the mass distributions of the optimized Ξ_c candidates and gain insights into the type of PDF shape used for the fit to the data. The selection of data candidates is done using the same final selection criteria obtained from the MC sample. From the fit to the mass distribution in data we obtain the widths and signal yields of each Ξ_c mode. In Sec. 6.6, we discuss the strategy for the measurement of the ratios of branching fractions and correct for PID selection inefficiencies in MC. After establishing the related uncertainties in the measurement of branching fractions, we provide the final results.

6.2. Data and MC Samples

For the study of Ξ_c, we use a run-dependent MC sample with an integrated luminosity of 356.70 fb^{-1} (exp18, proc13-chunk5), corresponding to 90.17 fb^{-1} of data collected at the $\Upsilon(4S)$ energy. The candidate events are reconstructed using the `basf2` release version `light-2409-toyger`.

	PXD hits	1st SVD layer hits	CDC hits	dr	$\lvert dz \rvert$
K,π	≥ 1	≥ 1	≥ 20	< 0.5 cm	< 2 cm

Table 6.2.: Impact parameter conditions used for prompt charged tracks in Ξ_c decays.

6.3. Reconstruction with Loose Cuts

Since the lifetimes of Ξ_c^0 and Ξ_c^+ are in the same order as that of Λ_c^+ (203 fs [6, 66]), we require the production vertex of the Ξ_c mothers to be consistent with the IP. For every Ξ_c mode, the entire decay chain is fitted using `TreeFit`, where a loose confidence level of the fit is required, $\chi^2 > 0.001$. The reconstructed invariant mass range for Ξ_c modes involving a primary hyperon Λ^0 is $2.425\,\text{GeV/c}^2 < M(\Xi_c) < 2.520\,\text{GeV/c}^2$, while Ξ_c modes involving a primary hyperon Ξ^- is $2.330\,\text{GeV/c}^2 < M(\Xi_c) < 2.620\,\text{GeV/c}^2$. In general, Ξ_c modes containing a primary hyperon Λ^0 share a common set of loose requirements, and similarly, modes containing a Ξ^- have a common set of loose requirements.
Next, we elaborate on the loose criteria imposed on the charged tracks and hyperons participating in the Ξ_c decays.

6.3.1. Prompt Charged Tracks

The prompt charged tracks are required to originate from a common vertex found near the IP, i.e., we impose the same impact parameter conditions as used in the previous chapter (reiterated in table 6.2).
To reduce the number of misidentified tracks, we require prompt kaons to be identified with

$$\text{binaryID}(K:\pi) := \mathcal{L}_K/(\mathcal{L}_K + \mathcal{L}_\pi) > 0.5 \tag{6.5}$$

and prompt pions to be identified with

$$\text{binaryID}(\pi:K) := \mathcal{L}_\pi/(\mathcal{L}_\pi + \mathcal{L}_K) > 0.5. \tag{6.6}$$

6.3.2. Loose Selection of Primary $\boldsymbol{\Lambda^0}$

Given that Λ^0 is the last composite particle in every decay chain of Ξ_c, we first define a list of standard Λ^0 particles, where oppositely charged protons and pions are combined. The selection of standard Λ^0 particles was introduced in Sec. 4.4, where a vertex fit is performed ($\chi^2 > 0$) and the invariant mass from proton and pion combinations is required to be within $1.100\,\text{GeV/c}^2 < M(p\pi^-) < 1.130\,\text{GeV/c}^2$.

6.3.3. Loose Selection of Primary $\boldsymbol{\Xi^-}$

Similarly, we define a selection of standard Ξ^- particles [70] with $\Xi^- \to \Lambda^0\pi^-$, where the standard Λ^0 particles must meet stricter criteria.

Secondary $\boldsymbol{\Lambda^0}$: A critical parameter for selecting Λ^0 from Ξ^- decays is the angle α between the momentum vector of Λ^0, $\vec{p}_{\Lambda^0}$, and the 3D distance vector of the Λ^0 decay vertex from the IP, $d\vec{R}_{\Lambda^0}$. This is illustrated in Fig. 6.1. The requirement $\cos\alpha^{\Lambda^0} > 0$ implies that Λ^0

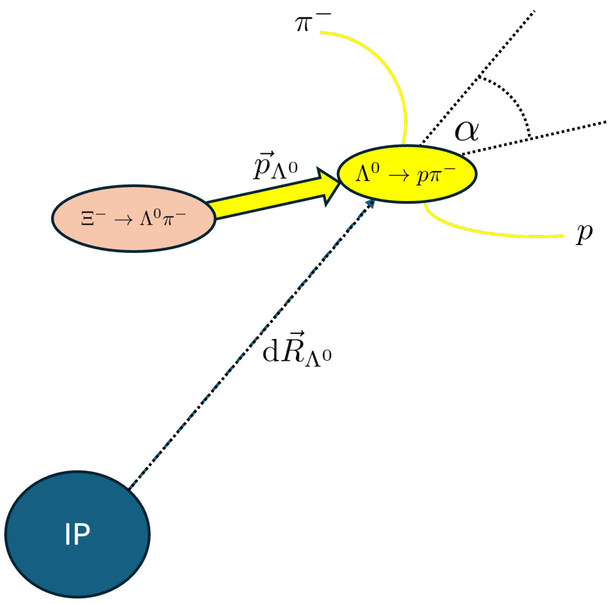

Figure 6.1.: Illustration of the angle α between the momentum of Λ^0, $\vec{p}_{\Lambda^0}$, and its distance vector from the IP, $d\vec{R}_{\Lambda^0}$.

originates from a displaced vertex away from the IP. Naturally, the fact that Λ^0 originates from an already long-lived Ξ^- should also be accounted for. From a study conducted in [70] (see also [71]), the decay vertex position of Λ^0 w.r.t. the IP is chosen such that $dR_{\Lambda^0} = \sqrt{dr^2_{\Lambda^0} + dz^2_{\Lambda^0}} > 0.35\,\mathrm{cm}$, where protons are loosely identified with $\mathrm{binaryID}_{\Lambda^0}(p:\pi) > 0.2$ and $\mathrm{binaryID}_{\Lambda^0}(p:K) > 0.2$.

Primary Ξ^-: The resolution of Ξ^- candidates can be enhanced by performing a vertex fit that constrains the mass of the secondary Λ^0 to its PDG value. The vertex fit is performed with `TreeFit`, requiring $\chi^2 > 0$ for fitted candidates in the mass window $1.295\,\mathrm{GeV/c^2} < M(\Lambda^0\pi^-) < 1.350\,\mathrm{GeV/c^2}$.
Building on previous arguments, we require that $dR_{\Lambda^0} > dR_{\Xi^-} > 0.1\,\mathrm{cm}$, with the displaced vertex characterized by the condition, $\cos\alpha^{\Xi^-} > 0$.
Finally, a very loose cut is imposed on the transverse momentum of pions that combine with the secondary Λ^0 to form Ξ^- candidates, specifically we require $\mathrm{pion}_{pT} > 50\,\mathrm{MeV/c}$. This limit accounts for the detector's limitations and helps mitigate unnecessary background events.

The loose selection criteria for the Ξ_c modes (and subdecays) are summarized in table 6.3. The MC efficiency (MC eff.) and number of reconstructed events (true-matched signal and background) are also provided.

<table>
<tr><th>Mother channels</th><th>Loose selection</th><th>MC eff. [%]</th><th>Events</th></tr>
<tr><td>$\Xi_c^0 \to \Lambda^0 K^- \pi^+$</td><td rowspan="2">$\Xi_c^{0,+}$:
$x_p > 0.4$,
$2.425\,\mathrm{GeV/c^2} < M(\Xi_c) < 2.520\,\mathrm{GeV/c^2}$,
IP constrained $\Xi_c^{0,+}$, TreeFit $\chi^2 > 0.001$
Λ^0 :
Standard Λ^0, introduced in 4.4:
$1.100\,\mathrm{GeV/c^2} < M(p\pi^-) < 1.130\,\mathrm{GeV/c^2}$
Vertex fit with TreeFit, $\chi^2 > 0$,
K^- :
binaryID$(K : \pi) > 0.5$
impact parameters of table 6.2
π^+ :
binaryID$(\pi : K) > 0.5$
impact parameters of table 6.2</td><td>18.04</td><td>signal:
21390
background:
4171418</td></tr>
<tr><td>$\Xi_c^+ \to \Lambda^0 K^- \pi^+ \pi^+$</td><td>11.05</td><td>signal:
6777
background:
1367628</td></tr>
<tr><td>$\Xi_c^0 \to \Xi^- \pi^+$</td><td rowspan="2">$\Xi_c^{0,+}$:
$x_p > 0.4$,
$2.330\,\mathrm{GeV/c^2} < M(\Xi_c) < 2.620\,\mathrm{GeV/c^2}$,
IP constrained $\Xi_c^{0,+}$, TreeFit $\chi^2 > 0.001$
Ξ^- :
Standard Ξ^-, where:
$1.295\,\mathrm{GeV/c^2} < M(\Lambda^0\pi^-) < 1.350\,\mathrm{GeV/c^2}$,
$dR_{\Lambda^0} > 0.35\,\mathrm{cm}$ and $\cos\alpha^{\Lambda^0} > 0$,
binaryID$_{\Lambda^0}(p : \pi) > 0.2$,
binaryID$_{\Lambda^0}(p : K) > 0.2$
$dR_{\Lambda^0} > dR_{\Xi^-} > 0.1\,\mathrm{cm}$ and $\cos\alpha^{\Xi^-} > 0$,
Λ^0-mass constrained Ξ^-, TreeFit $\chi^2 > 0$,
pion$_{pT}(\Xi^- \to \Lambda^0\pi^-) > 50\,\mathrm{MeV}$
π^+ :
binaryID$(\pi : K) > 0.5$,
impact parameters of table 6.2</td><td>11.81</td><td>signal:
3889
background:
20085</td></tr>
<tr><td>$\Xi_c^+ \to \Xi^- \pi^+ \pi^+$</td><td>7.55</td><td>signal:
13975
background:
34879</td></tr>
</table>

Table 6.3.: Loose selection criteria for the Ξ_c modes. The middle column of the table specifies the loose selection for the mothers (Ξ_c), the primary hyperons (Λ^0 or Ξ^-), and the prompt charged tracks (K^- or π^+). The signal and background events are based on MC truth-matching.

6.4. Optimizations

The optimizations are carried out in the signal region of every Ξ_c mode. Concretely, the width σ, attributed to a fitted Gaussian over the invariant mass distribution of true-matched Ξ_c candidates, is used for the definition of the signal region. For simplicity, we express the signal region in terms of the difference between the reconstructed invariant mass of Ξ_c and its PDG mass value, $|M_{\Xi_c} - m_{\Xi_c}| < 3\sigma$, where m denotes the PDG value. The signal region used for the optimization of the signal significance in each Ξ_c mode reads,

$$\begin{aligned}
\Xi_c^0 \to \Lambda^0 K^- \pi^+ : &\quad |M_{\Xi_c^0} - m_{\Xi_c^0}| < 11.2\,\mathrm{MeV/c^2}, \\
\Xi_c^+ \to \Lambda^0 K^- \pi^+ \pi^+ : &\quad |M_{\Xi_c^+} - m_{\Xi_c^+}| < 9.5\,\mathrm{MeV/c^2}, \\
\Xi_c^0 \to \Xi^- \pi^+ : &\quad |M_{\Xi_c^0} - m_{\Xi_c^0}| < 22.5\,\mathrm{MeV/c^2}, \\
\Xi_c^+ \to \Xi^- \pi^+ \pi^+ : &\quad |M_{\Xi_c^+} - m_{\Xi_c^+}| < 18.1\,\mathrm{MeV/c^2}.
\end{aligned}$$

The signal regions are shown between vertical red lines in Fig. 6.2 (left). Note that this is not a cut we make on the selection of Ξ_c candidates but simply a means of optimization. For clarity, the number of events and efficiency of each cut (signal efficiency, MC efficiency, background rejection, etc.) expressed in summary tables, are in terms of the reconstructed Ξ_c mass regions listed in table 6.3.[1]

In contrast, an actual cut is applied that limits the selection of primary hyperons to their signal region. We select

$$|M_{\Lambda^0} - m_{\Lambda^0}| < 3\,\mathrm{MeV/c^2} \tag{6.7}$$

and

$$|M_{\Xi^-} - m_{\Xi^-}| < 6.5\,\mathrm{MeV/c^2} \tag{6.8}$$

for all modes involving these primary hyperons. The signal regions are shown between vertical red lines in Fig. 6.2 (right). The selected signal region of each primary hyperon retains approximately 95% of the hyperon signal.

[1] This is to ensure a clear comparison to the eventual yield from a fit to the MC mass distributions, where sideband regions are included.

Ξ_c modes with a primary Λ^0:

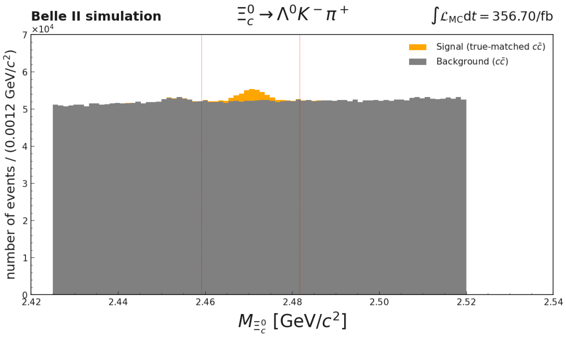

(a)

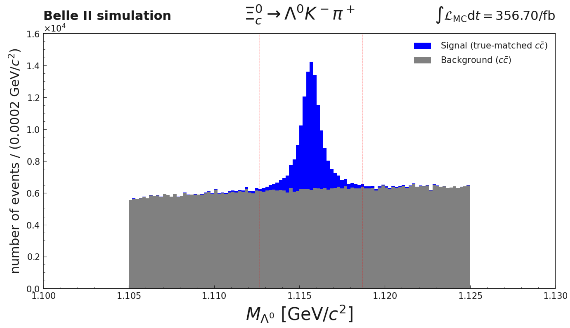

(b)

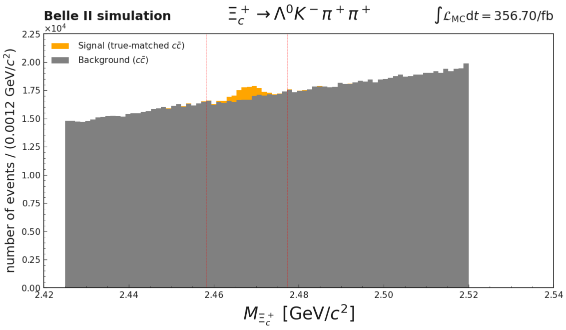

(c)

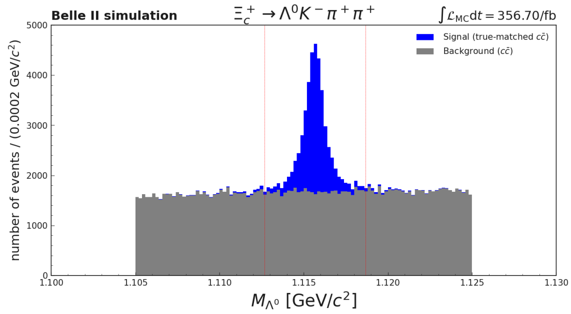

(d)

Ξ_c modes with a primary Ξ^-:

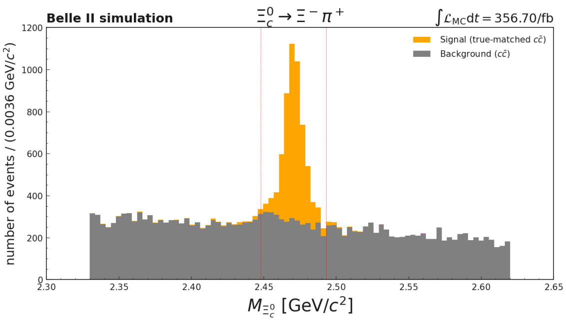

(e)

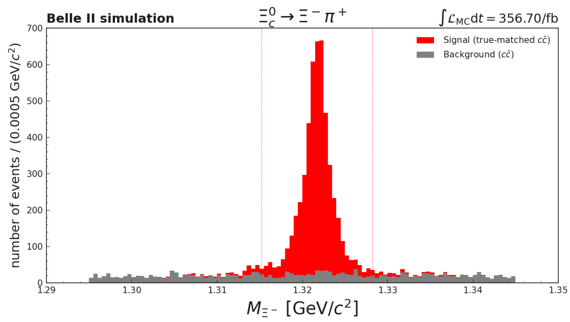

(f)

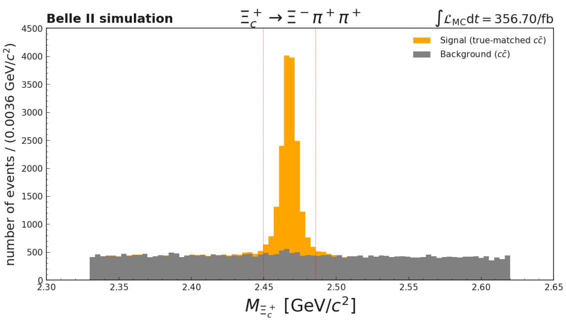

(g)

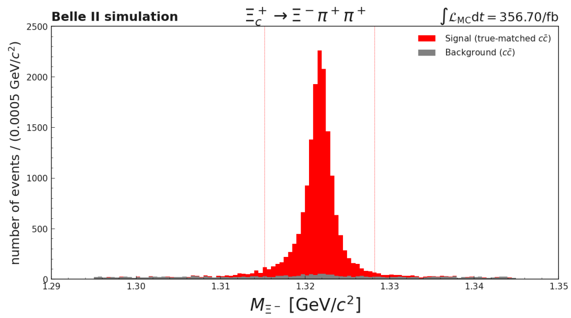

(h)

Figure 6.2.: Invariant mass distribution of the reconstructed Ξ_c modes (left) and corresponding primary hyperon (right) in Ξ_c signal region. The vertical red lines simply indicate the region where most of the true-matched events are found (signal region), discussed in the main text.

Mother channel	Selection	FOM	sig. eff. [%]	bkg. rej. [%]
$\Xi_c^0 \to \Lambda^0 K^- \pi^+$	$\lvert M_{\Lambda^0} - m_{\Lambda^0}\rvert < 3\,\mathrm{MeV/c^2}$	20.6	95.8	76.9
	$\mathrm{binaryID}_{\Lambda^0}(p : \pi) > 0.6$	36.4	88.5	94.0
	$\mathrm{binaryID}_{\Lambda^0}(p : K) > 0.6$	39.7	86.6	95.2
$\Xi_c^+ \to \Lambda^0 K^- \pi^+ \pi^+$	$\lvert M_{\Lambda^0} - m_{\Lambda^0}\rvert < 3\,\mathrm{MeV/c^2}$	11.1	95.9	75.3
	$\mathrm{binaryID}_{\Lambda^0}(p : \pi) > 0.5$	17.9	88.0	92.3
	$\mathrm{binaryID}_{\Lambda^0}(p : K) > 0.5$	19.0	85.9	93.6
$\Xi_c^0 \to \Xi^- \pi^+$	$\lvert M_{\Xi^-} - m_{\Xi^-}\rvert < 6.5\,\mathrm{MeV/c^2}$	31.4	95.0	49.6
$\Xi_c^+ \to \Xi^- \pi^+ \pi^+$	$\lvert M_{\Xi^-} - m_{\Xi^-}\rvert < 6.5\,\mathrm{MeV/c^2}$	72.5	94.8	42.3

Table 6.4.: Selection of Ξ_c candidates from optimized PID cuts of the hyperon daughter tracks. Each cut is accumulated and compared to the loose selection, i.e., the Ξ_c signal efficiency (sig. eff.) and background rejection (bkg. rej.) are in reference to the total number of reconstructed signal candidates using the loose selections listed in table 6.3.

6.4.1. PID Cuts on Daughter Tracks

Within the selected signal region of the primary hyperons, we optimize the binary IDs of the charged tracks constituting the primary hyperon decays. In principle, the binary IDs for the prompt charged tracks could also be optimized further; however, the maximum FOM is often only slightly higher for tighter cuts compared to the loose selection, so they are left unchanged. The focus is then set on the optimization of binary IDs for the hyperon daughter tracks.

For $\Xi_c^0 \to \Lambda^0 K^- \pi^+$, we search for a maximum FOM in the binary ID for proton tracks which combine with pions to form the primary Λ^0. The binary IDs of the proton track, $\mathrm{binaryID}_{\Lambda^0}(p : \pi)$ and $\mathrm{binaryID}_{\Lambda^0}(p : K)$, are optimized. The pion track in Λ^0 is left unchanged, as no higher FOM is found for tighter binary IDs. The procedure is analogous for $\Xi_c^+ \to \Lambda^0 K^- \pi^+ \pi^+$. In the case of $\Xi_c^0 \to \Xi^- \pi^+$ and $\Xi_c^+ \to \Xi^- \pi^+ \pi^+$, the binary IDs of the pion associated with Ξ^- do not exhibit an optimum threshold above zero. The PID cuts and the Ξ_c selection performance are summarized in table 6.4.

Channel	Hyperon	L/σ cut	After selections of table 6.4		
			FOM	sig. eff. [%]	bkg. rej. [%]
$\Xi_c^0 \to \Lambda^0 K^- \pi^+$	Λ^0	> 3	43.1	85.4	96.1
$\Xi_c^+ \to \Lambda^0 K^- \pi^+ \pi^+$	Λ^0	> 4	20.3	84.6	94.6
$\Xi_c^0 \to \Xi^- \pi^+$	Ξ^-	> 4	34.2	93.5	61.9
$\Xi_c^+ \to \Xi^- \pi^+ \pi^+$	Ξ^-	> 3	76.4	94.2	52.5

Table 6.5.: Application of cuts on the flight significance of primary hyperons. The FOM, signal efficiency and background rejection are given w.r.t. the loose selection, and after applying the selections in table 6.4.

6.4.2. Flight Significance Cuts

Another useful discriminator is the flight significance, L/σ, where L is the flight distance (flight length) of the primary hyperon w.r.t. the fitted decay vertex of the mother Ξ_c, and σ is the uncertainty of L. These parameters are determined by `TreeFit` in the vertex fit, as discussed in Sec. 4.3.
The optimization of the flight significance of Λ^0 are shown in Fig. 6.3(a)-(b) for $\Xi_c^0 \to \Lambda^0 K^- \pi^+$ and in Fig. 6.3(c)-(d) for $\Xi_c^+ \to \Lambda^0 K^- \pi^+ \pi^+$. Similarly, the optimizations of Ξ^- are shown in Fig. 6.3(e)-(f) for $\Xi_c^0 \to \Xi^- \pi^+$ and in Fig. 6.3(g)-(h) for $\Xi_c^+ \to \Xi^- \pi^+ \pi^+$. The results of the optimization are summarized in table 6.5.

6.4.3. Final Selection Summary

The final selection criteria for $\Xi_c^0 \to \Lambda^0 K^- \pi^+$ and $\Xi_c^0 \to \Xi^- \pi^+$ candidates are summarized in table 6.6, while the final selection criteria for the $\Xi_c^+ \to \Lambda^0 K^- \pi^+ \pi^+$ and $\Xi_c^+ \to \Xi^- \pi^+ \pi^+$ candidates are summarized in table 6.7. With respect to the loose selections, for Ξ_c modes containing a primary Λ^0 hyperon, approximately 85% of the signal candidates have been retained in the final selection, while approximately 95% of the background has been removed. For Ξ_c modes containing a primary Ξ^- hyperon, over 93% of the signal candidates have been retained and over 52% of the background has been removed.

In the next section, we apply this final selection criteria and fit over the invariant mass distributions of the Ξ_c modes.

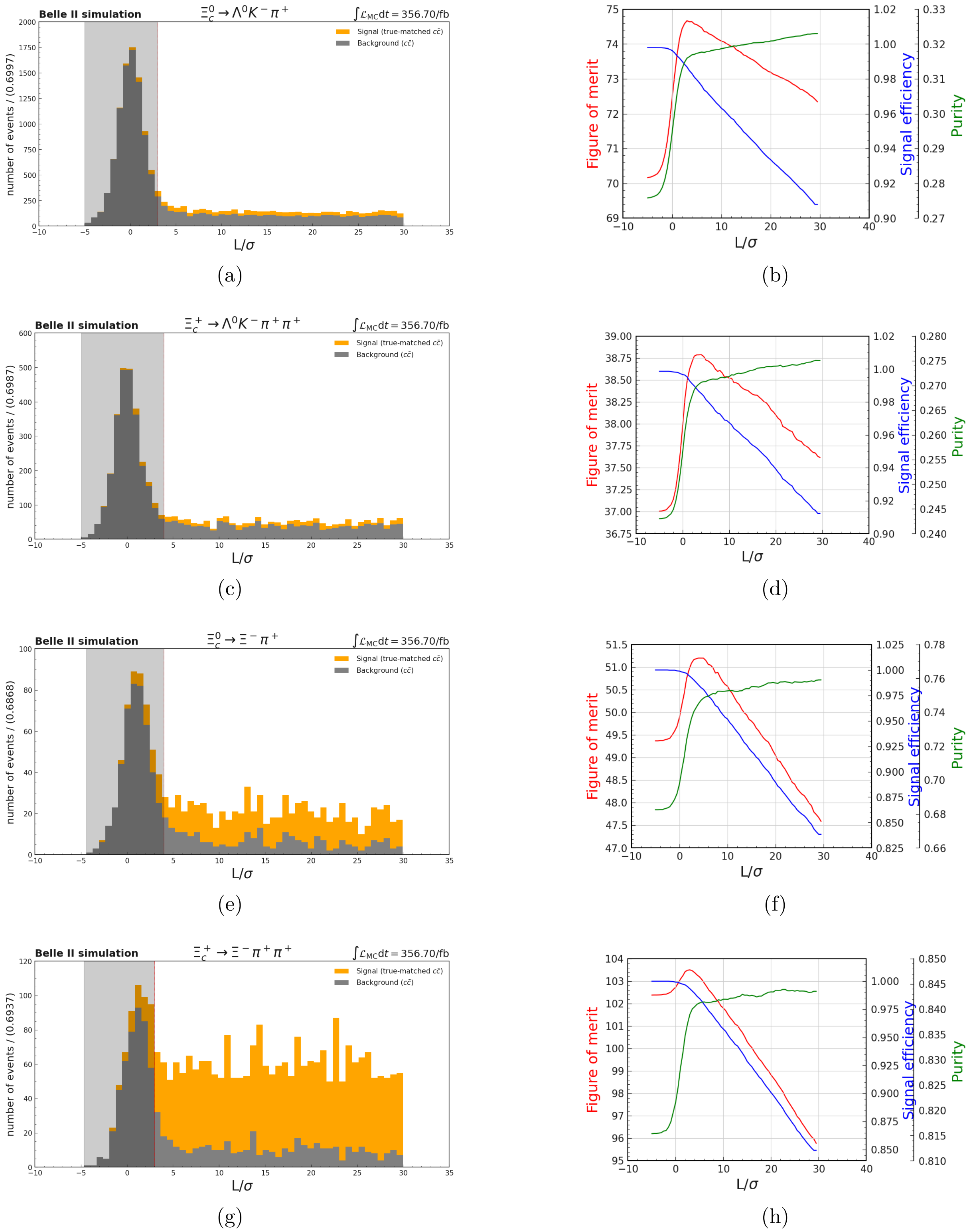

Figure 6.3.: Flight significance L/σ distributions (left) and flight significance FOM optimizations (right), for each Ξ_c mode from top to bottom. The shaded region in the flight significance distributions indicate the part of the distribution that is removed from the selection.

Mother channels	Final selection	MC eff. [%]	Events
$\Xi_c^0 \to \Lambda^0 K^- \pi^+$	Ξ_c^0 : $x_p > 0.4$, $2.425\,\mathrm{GeV/c^2} < M(\Xi_c) < 2.520\,\mathrm{GeV/c^2}$, IP constrained Ξ_c^0, `TreeFit` $\chi^2 > 0.001$ Λ^0 : Standard Λ^0 (loose selection), and: $\lvert M_{\Lambda^0} - m_{\Lambda^0}\rvert < 3\,\mathrm{MeV/c^2}$ $\mathrm{binaryID}_{\Lambda^0}(p:\pi) > 0.6$ $\mathrm{binaryID}_{\Lambda^0}(p:K) > 0.6$ $L/\sigma > 3$ K^- : $\mathrm{binaryID}(K:\pi) > 0.5$ impact parameters of table 6.2 π^+ : $\mathrm{binaryID}(\pi:K) > 0.5$ impact parameters of table 6.2	15.41	signal: 18273 (85.4% retained) background: 161344 (96.1% rejected)
$\Xi_c^0 \to \Xi^- \pi^+$	Ξ_c^0 : $x_p > 0.4$, $2.330\,\mathrm{GeV/c^2} < M(\Xi_c) < 2.620\,\mathrm{GeV/c^2}$, IP constrained Ξ_c^0, `TreeFit` $\chi^2 > 0.001$ Ξ^- : Standard Ξ^- (loose selection), and: $\lvert M_{\Xi^-} - m_{\Xi^-}\rvert < 6.5\,\mathrm{MeV/c^2}$ $L/\sigma > 4$ π^+ : $\mathrm{binaryID}(\pi:K) > 0.5$, impact parameters of table 6.2	11.05	signal: 3638 (93.5% retained) background: 7646 (61.9% rejected)

Table 6.6.: Final selection criteria for the Ξ_c^0 modes. The middle column of the table specifies the final selection for the mothers (Ξ_c^0), the primary hyperons (Λ^0 or Ξ^-), and the prompt charged tracks (K^- or π^+). The signal and background events are based on MC truth-matching. The retained signal and rejected background percentages are given in reference to the loose selection.

Mother channels	Final selection	MC eff. [%]	Events
$\Xi_c^+ \to \Lambda^0 K^- \pi^+ \pi^+$	Ξ_c^+ : $x_p > 0.4$, $2.425\,\mathrm{GeV/c^2} < M(\Xi_c) < 2.520\,\mathrm{GeV/c^2}$, IP constrained Ξ_c^+, `TreeFit` $\chi^2 > 0.001$ Λ^0 : Standard Λ^0 (loose selection), and: $\lvert M_{\Lambda^0} - m_{\Lambda^0}\rvert < 3\,\mathrm{MeV/c^2}$ $\mathrm{binaryID}_{\Lambda^0}(p : \pi) > 0.5$ $\mathrm{binaryID}_{\Lambda^0}(p : K) > 0.5$ $L/\sigma > 4$ K^- : $\mathrm{binaryID}(K : \pi) > 0.5$ impact parameters of table 6.2 π^+ : $\mathrm{binaryID}(\pi : K) > 0.5$ impact parameters of table 6.2	9.35	signal: 5733 (84.6% retained) background: 74395 (94.6% rejected)
$\Xi_c^+ \to \Xi^- \pi^+ \pi^+$	Ξ_c^+ : $x_p > 0.4$, $2.330\,\mathrm{GeV/c^2} < M(\Xi_c) < 2.620\,\mathrm{GeV/c^2}$, IP constrained Ξ_c^+, `TreeFit` $\chi^2 > 0.001$ Ξ^- : Standard Ξ^- (loose selection), and: $\lvert M_{\Xi^-} - m_{\Xi^-}\rvert < 6.5\,\mathrm{MeV/c^2}$ $L/\sigma > 3$ π^+ : $\mathrm{binaryID}(\pi : K) > 0.5$, impact parameters of table 6.2	7.11	signal: 13166 (94.2% retained) background: 16556 (52.5% rejected)

Table 6.7.: Final selection criteria for the Ξ_c^+ modes. The middle column of the table specifies the loose selection for the mothers (Ξ_c^+), the primary hyperons (Λ^0 or Ξ^-), and the prompt charged tracks (K^- or π^+). The signal and background events are based on MC truth-matching. The retained signal and rejected background percentages are given in reference to the loose selection.

6.5. Mass Distribution Fits

In this section, we fit the mass distributions of the final Ξ_c candidates of the MC sample. The general shape of the model retrieved from the fit to MC will serve as an Ansatz for the choice of PDFs used in the fit to the data.

6.5.1. Fit to MC

The mass distribution of the final Ξ_c candidates in the MC sample are shown on the left plots of Fig. 6.4. The plots on the right side of Fig. 6.4 present the fits to the mass distributions. Similar to the PDF shape used for fitting the $\Lambda_c^+ \to pK^-\pi^+$ mode (discussed in Chapter 5), we find that the signal in the mass distribution of Ξ_c modes can be generally parametrized by a double Gaussian PDF,

$$\mathrm{PDF}_{\mathrm{signal}}(M_{\Xi_c}) = w_{\mathrm{core}} \times \frac{1}{\sqrt{2\pi\sigma_1^2}} e^{-\frac{(M_{\Xi_c}-\mu)^2}{2\sigma_1^2}} + w_{\mathrm{tail}} \times \frac{1}{\sqrt{2\pi\sigma_2^2}} e^{-\frac{(M_{\Xi_c}-\mu)^2}{2\sigma_2^2}} \tag{6.9}$$

where μ is the mean value of the distribution and $\sigma_{1,2}$ their respective widths. w_{core} and w_{tail} are weight factors for each Gaussian component, acting as the normalization factors of the double Gaussian PDF. The relation between the weights, $w_{\mathrm{tail}} + w_{\mathrm{core}} = 1$, holds. In general, the introduction of a (subdominant) second Gaussian with a width of σ_2 helps us to account for the spread of the tails of the peaking distribution.
Since no peaking backgrounds are present in our selected mass regions, we parametrize the background shape with an exponential PDF,

$$\mathrm{PDF}_{\mathrm{background}}(M_{\Xi_c}) = N \times e^{\tau \cdot M_{\Xi_c}} \tag{6.10}$$

where N is a normalization constant and τ represents the slope parameter of the exponential function. Note that in the case of $\Xi_c^0 \to \Lambda^0 K^-\pi^+$, the fit yielded better results with a single Gaussian, in such case the second Gaussian is omitted. For all fits, all the fit parameters are floated.
The results of the fits are summarized in table 6.8, where the signal yields from the fit are compared to the number of true-matched candidates in the sample. To represent the performance of the fit, the χ^2/ndf value of the fit and the residual, are provided. The residual expresses the difference between the fitted yield (N_{fit}) and the number of true-matched candidates (N_{sig}) in units of the uncertainty of the fit yield. The fraction result in table 6.8 expresses a ratio and encodes how much of the signal is captured by the Gaussian with width σ_1 with respect to the second Gaussian with width σ_2.
Generally, the fit yields good results in all Ξ_c modes. We thus use these PDF shapes to fit over the mass distributions in data, which we present next.

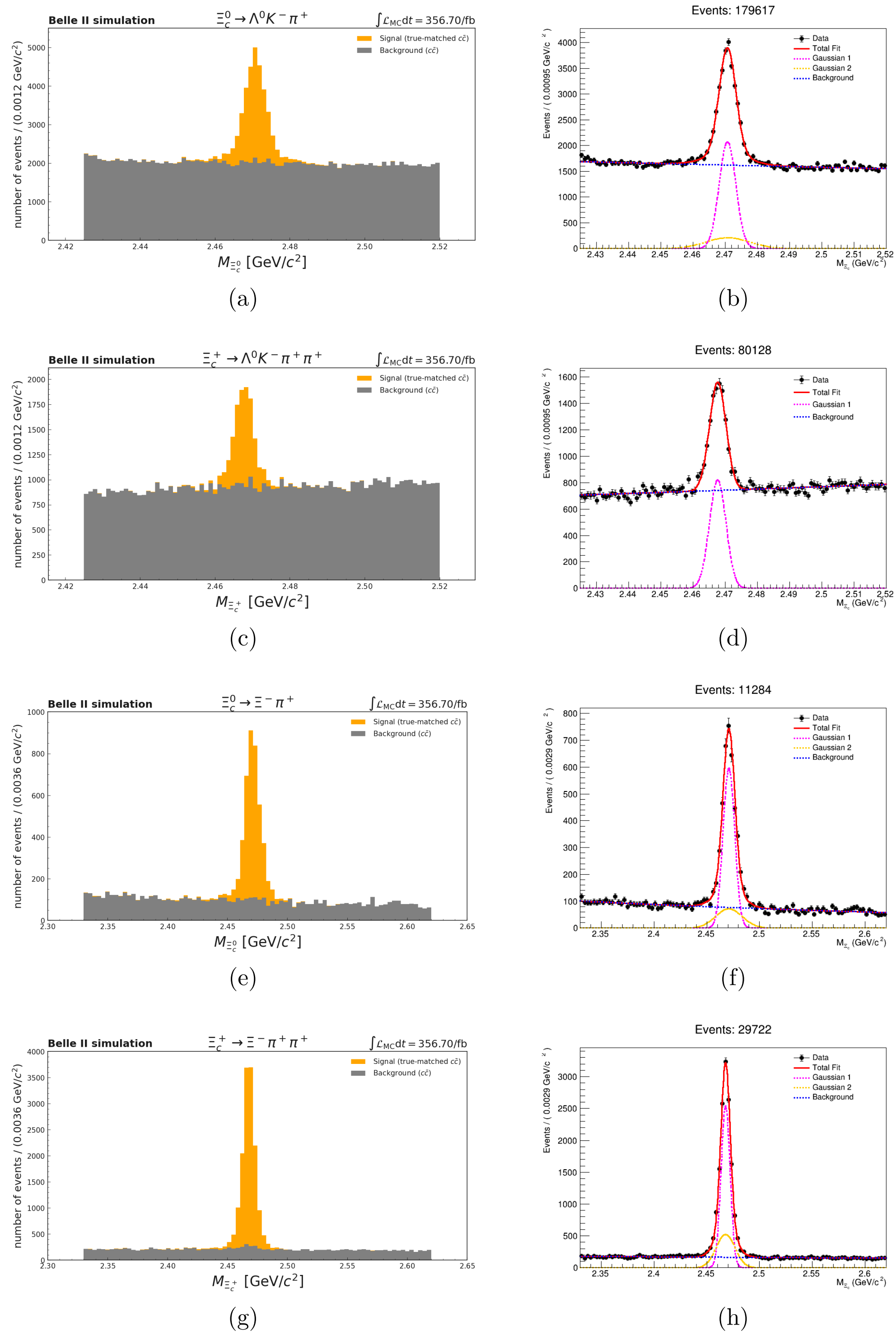

Figure 6.4.: Left: Invariant mass distribution of the optimized Ξ_c modes where the signal distribution is stacked on top of the background. Right: Fit to the MC mass distributions shown on the left side. Except for the mode $\Xi_c^+ \to \Lambda^0 K^- \pi^+ \pi^+$ in (d), the total PDF fit (represented by the red curve) involves a double Gaussian PDF for the signal (purple and yellow) and an exponential function for the background (blue). The mass distributions are represented by black data points with Poisson errors. For $\Xi_c^+ \to \Lambda^0 K^- \pi^+ \pi^+$, the fit is done using a single Gaussian PDF for the signal (purple) and an exponential function for the background (blue).

	$\Xi_c^0 \to \Lambda^0 K^- \pi^+$	$\Xi_c^+ \to \Lambda^0 K^- \pi^+ \pi^+$	$\Xi_c^0 \to \Xi^- \pi^+$	$\Xi_c^+ \to \Xi^- \pi^+ \pi^+$
N_{sig}	18273	5733	3638	13166
N_{fit}	17817 ± 340	5549 ± 137	3591 ± 78	13327 ± 135
Residual	-1.3σ	-1.3σ	-0.6σ	$+1.2\sigma$
σ_1 [MeV/c^2]	2.6 ± 0.1	2.6 ± 0.1	5.5 ± 0.3	4.2 ± 0.2
σ_2 [MeV/c^2]	6.7 ± 1.0	-	12.5 ± 2.3	8.9 ± 0.9
Fraction [%]	79.2 ± 4.1	-	78.5 ± 7.3	70.1 ± 6.5
τ [GeV/c^2]$^{-1}$	-0.9 ± 0.1	1.1 ± 0.1	-1.9 ± 0.1	-0.6 ± 0.1
N_{bkg}	161802 ± 510	74582 ± 297	7693 ± 101	16395 ± 146
χ^2/ndf	1.2	1.1	1.1	0.9

Table 6.8.: Fit results of the fit to the MC mass distributions of each Ξ_c mode. N_{sig} (N_{fit}) represents the number of true-matched (fitted) signal events. The χ^2/ndf value indicates the goodness of the fit obtained using `RooFit` (discussed in Sec. 4.8.2).

6.5.2. Fit to the Data

After establishing the final selection criteria for optimal Ξ_c candidates and gaining insights into the general shapes of the signal and background distributions from MC, we direct our attention to data, where no further optimizations are made. Here, we fit the mass distribution of Ξ_c, assuming the peaking distribution to follow a Gaussian-like shape and the background to be modeled by an exponential shape, i.e., we apply PDF shapes motivated by our analysis of the MC mass distributions. We fit the data with all the PDF parameters floating.
In Fig. 6.5, Fig. 6.6, Fig. 6.7 and Fig. 6.8, the total PDF fit to the mass distributions of $\Xi_c^0 \to \Lambda^0 K^- \pi^+$, $\Xi_c^+ \to \Lambda^0 K^- \pi^+ \pi^+$, $\Xi_c^0 \to \Xi^- \pi^+$ and $\Xi_c^+ \to \Xi^- \pi^+ \pi^+$ are shown, respectively. The fit results are summarized in a table within each figure.
The bottom plot in each figure portrays a pull distribution, defined as,

$$\text{Pull}_i = \frac{N_{\text{data},_i} - N_{\text{fit},_i}}{\sqrt{N_{\text{data},i}}}, \tag{6.11}$$

where i represents each of the 100 bins used in the fit, $N_{\text{data},_i}$ is the number of data events in the bin i, $N_{\text{fit},_i}$ is the number of fitted events in bin i, and $\sqrt{N_{\text{data},i}}$ is the Poisson error of the data per bin i. Horizontal dashed lines are placed in the pull plot to represent the deviations of the model within $\pm 3\sigma$, where σ signifies units of $\sqrt{N_{\text{data},i}}$.

- Fig. 6.5, $\boldsymbol{\Xi_c^0 \to \Lambda^0 K^- \pi^+}$: The best fit for the mass distribution of this mode is obtained using a single Gaussian (as opposed to a double Gaussian in MC). The total PDF fit, composed of the single Gaussian and the exponential function, performs generally well ($\chi^2 = 0.92$). Slight deviations are seen on the sideband regions, however these fluctuations fall within $\pm 3\sigma$ of the pull distribution, therefore, no re-adjustments to the background PDF are made. The obtained width reads

  $$\sigma_1 = (3.0 \pm 0.2)\ \text{MeV}/c^2, \tag{6.12}$$

  with a signal yield of

  $$\boxed{N^{\text{fit}}_{\Lambda K \pi} = 2518 \pm 130_{\text{stat}}.} \tag{6.13}$$

  We refer to the uncertainty in the yield as the statistical uncertainty, as it is associated with the sample size.

- Fig. 6.6, $\boldsymbol{\Xi_c^+ \to \Lambda^0 K^- \pi^+ \pi^+}$: Like the previous mode, the fit to the signal mass distribution is performed using a single Gaussian PDF, where the width,

  $$\sigma_1 = (2.8 \pm 0.2)\ \text{MeV}/c^2, \tag{6.14}$$

  yields

  $$\boxed{N^{\text{fit}}_{\Lambda K \pi\pi} = 1044 \pm 78_{\text{stat}}.} \tag{6.15}$$

- Fig. 6.7, $\boldsymbol{\Xi_c^0 \to \Xi^-\pi^+}$: The best fit to the signal mass distribution in this mode is found using a double Gaussian PDF for the signal component, where

$$\sigma_1 = (3.2 \pm 0.6)\ \mathrm{MeV}/c^2 \qquad \text{and} \qquad \sigma_2 = (7.6 \pm 0.5)\ \mathrm{MeV}/c^2, \tag{6.16}$$

  yielding

$$\boxed{N^{\mathrm{fit}}_{\Xi\pi} = 2235 \pm 60_{\mathrm{stat}}.} \tag{6.17}$$

- Fig. 6.8, $\boldsymbol{\Xi_c^+ \to \Xi^-\pi^+\pi^+}$: For this mode, we find

$$\sigma_1 = (3.6 \pm 0.6)\ \mathrm{MeV}/c^2 \qquad \text{and} \qquad \sigma_2 = (7.6 \pm 1.5)\ \mathrm{MeV}/c^2, \tag{6.18}$$

  yielding

$$\boxed{N^{\mathrm{fit}}_{\Xi\pi\pi} = 2626 \pm 71_{\mathrm{stat}}.} \tag{6.19}$$

In the next section, we discuss how we use these results to retrieve the ratio of branching fractions,

$$\frac{\mathcal{B}(\Xi_c^0 \to \Lambda K^-\pi^+)}{\mathcal{B}(\Xi_c^0 \to \Xi^-\pi^+)} \tag{6.20}$$

and

$$\frac{\mathcal{B}(\Xi_c^+ \to \Lambda K^-\pi^+\pi^+)}{\mathcal{B}(\Xi_c^+ \to \Xi^-\pi^+\pi^+)}. \tag{6.21}$$

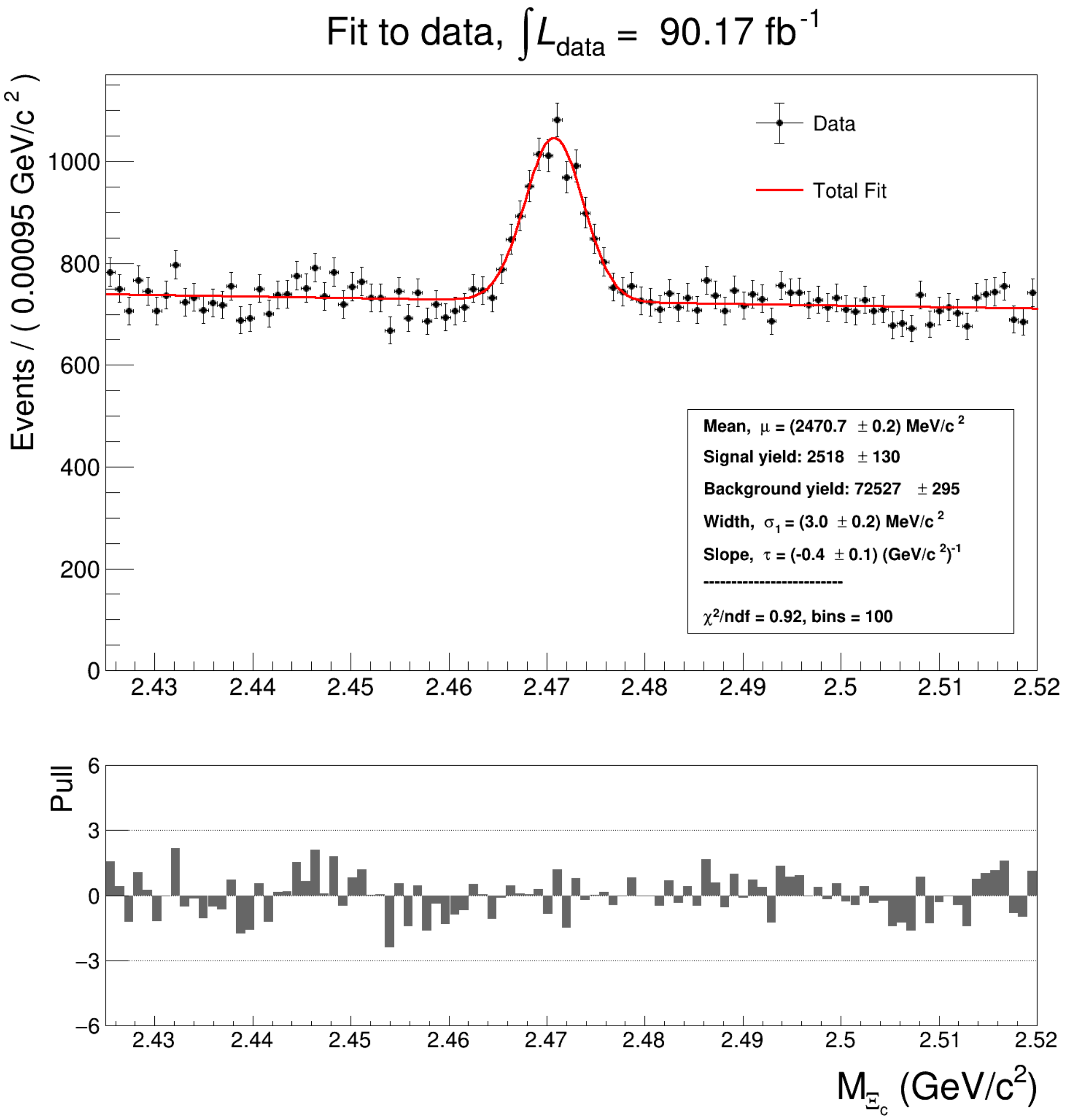

Figure 6.5.: Mass distribution fit of $\boxed{\Xi_c^0 \to \Lambda^0 K^- \pi^+}$.

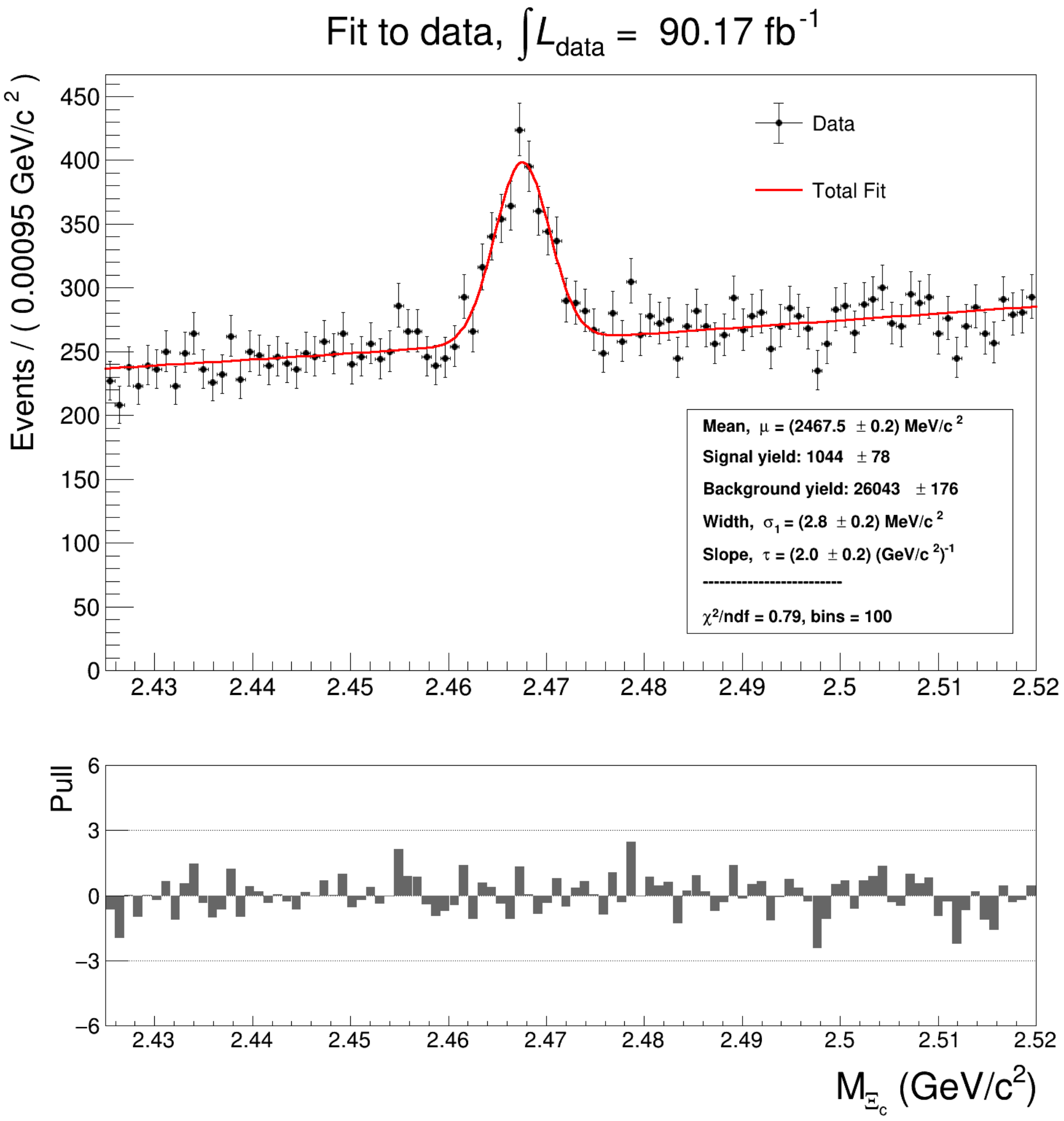

Figure 6.6.: Mass distribution fit of $\boxed{\Xi_c^+ \to \Lambda^0 K^- \pi^+ \pi^+}$.

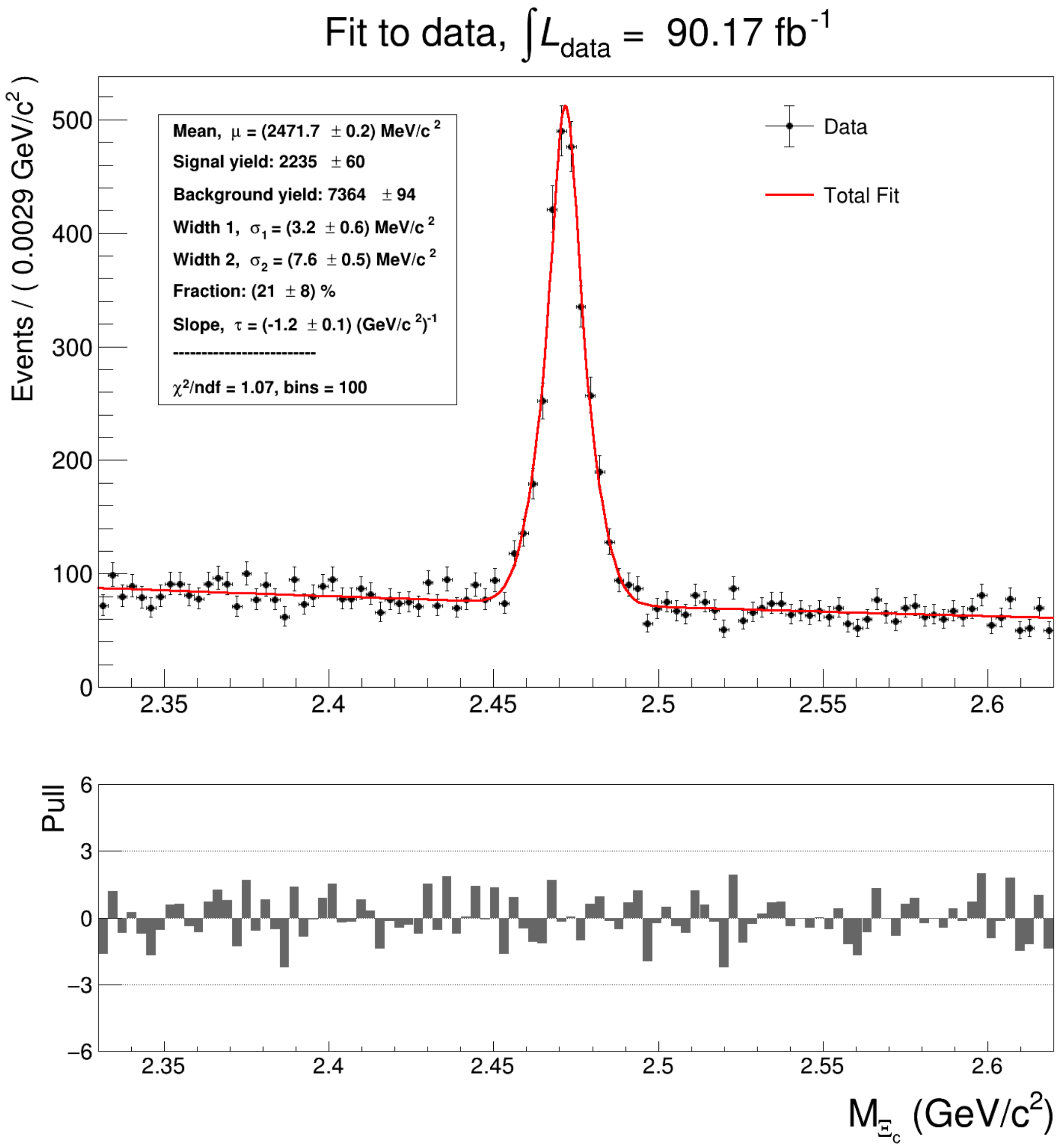

Figure 6.7.: Mass distribution fit of $\boxed{\Xi_c^0 \to \Xi^- \pi^+}$.

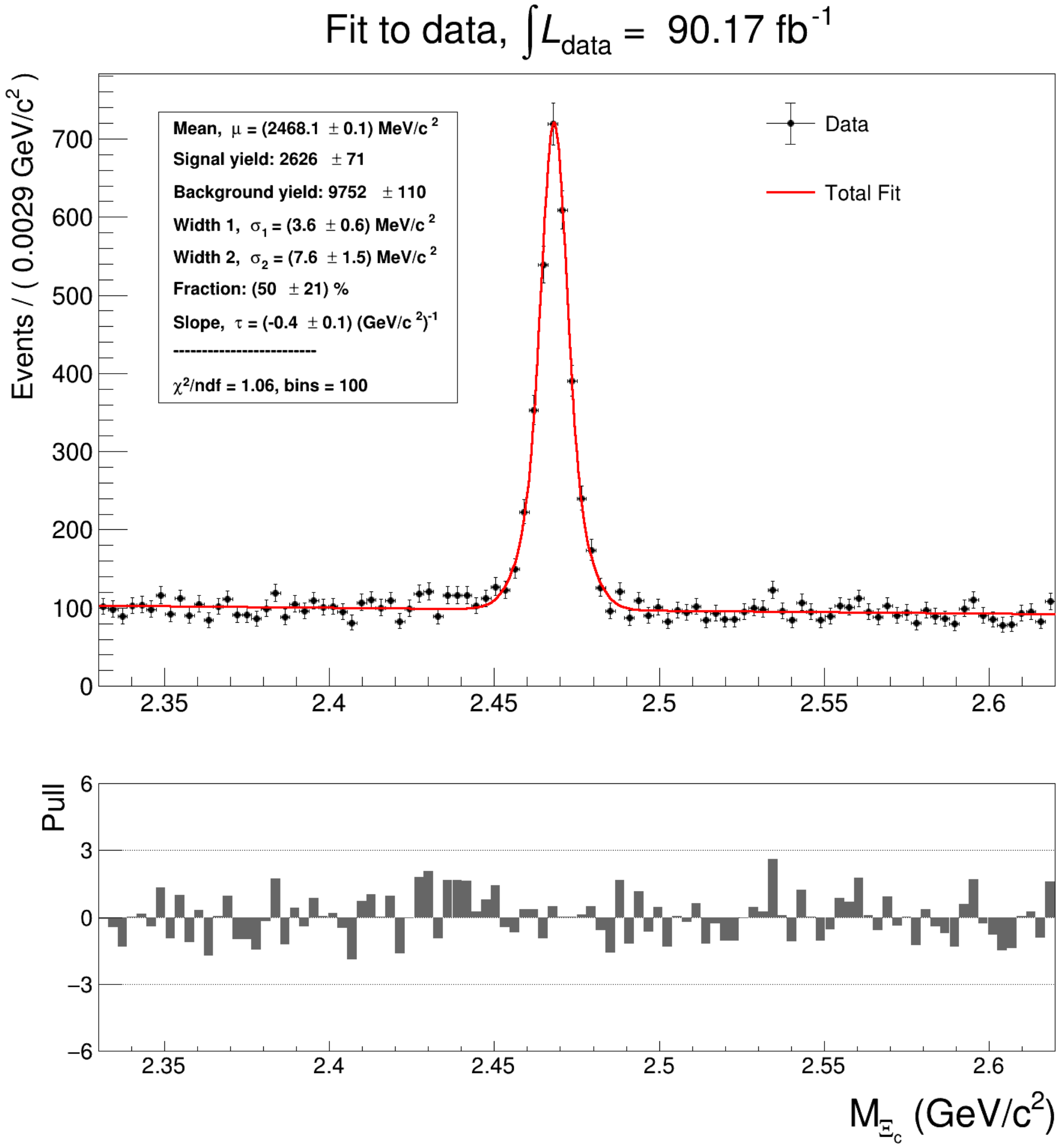

Figure 6.8.: Mass distribution fit of $\boxed{\Xi_c^+ \to \Xi^- \pi^+ \pi^+}$.

6.6. Ratio of Ξ_c Branching Fractions

In this section, we determine the ratio of the branching fractions for same-charge charmed baryons, where the decays involving a Ξ^- hyperon are used as the reference modes. In compact form, we can express the ratio of branching fractions as

$$r(\Xi_c^{0\{+\}}) := \frac{\mathcal{B}(\Xi_c^{0\{+\}} \to \Lambda K^-\pi^+\{\pi^+\})}{\mathcal{B}(\Xi_c^{0\{+\}} \to \Xi^-\pi^+\{\pi^+\})} = \frac{N^{\text{fit}}_{\Lambda K\pi\{\pi\}}\epsilon_{\Xi\pi\{\pi\}}}{N^{\text{fit}}_{\Xi\pi\{\pi\}}\epsilon_{\Lambda K\pi\{\pi\}}}\mathcal{B}(\Xi^- \to \Lambda\pi^-), \tag{6.22}$$

where the ratio $r(\Xi_c^0)$ implies the exclusion of the pions within curly brackets, and when the ratio $r(\Xi_c^+)$ is treated, the extra pions are included. Note that the branching fraction, $\mathcal{B}(\Lambda \to p\pi^-)$, cancels out from the ratio. In Eq. (6.22), ϵ represents the MC efficiency of our selection. The numerical definition of ϵ will be elaborated in more detail throughout this section.
In our calculations of $r(\Xi_c^{0\{+\}})$, we use the world average result for the hyperon branching fraction of Eq. (6.22), where $\mathcal{B}(\Xi^- \to \Lambda\pi^-) = (99.89 \pm 0.04)\%$ [6].
As for any measurement, there are always uncertainties associated with any determined value. Some common sources of uncertainty between the numerator mode and the reference mode in $r(\Xi_c^{0\{+\}})$ are expected to cancel. However, the systematic effects and the overall PID performance of our selection criteria in MC, compared to data, may differ strongly across modes. Therefore, we first consider the detection-efficiency corrections related to our PID selection criteria, per track and per mode, where the Belle II Systematic Corrections Framework [57], introduced in Sec. 4.2, is used. We then proceed with the introduction of other sources of uncertainty. Lastly, we provide the results for the ratio of branching fractions.

6.6.1. Efficiency Corrections and Related Uncertainties

The systematics correction framework provides correction factors in bins of the momentum p and the polar angle θ, along with statistical and systematic uncertainties related to the PID selection. To obtain the data/MC correction factors, we quantify the PID efficiency corrections per track that underwent a PID cut in our MC sample. We restrict our data/MC efficiency investigation to the subcollection `proc13-chunk5`, which represents the MC and corresponding data samples used in the present thesis. The control modes used by the Systematics Correction Framework for the calibration of the data/MC PID efficiency corrections were listed in Sec. 4.2.
The individual data/MC efficiency correction factors per PID cut track are multiplied together to give the overall correction factor r_ϵ,

$$r_\epsilon = \prod_i^{\text{PID cut tracks}} (\epsilon_{\text{data}}/\epsilon^*_{\text{MC}})_i\,. \tag{6.23}$$

The corrected MC efficiency for any mode is then given by $\epsilon_{\text{MC}} = \epsilon^*_{\text{MC}} \times r_\epsilon$, where ϵ^*_{MC} represents the MC efficiency before the correction weights are applied. In this regard, to ensure the independence of the modes, overlapping events between modes were vetoed and

		modes for $r(\Xi_c^0)$		modes for $r(\Xi_c^+)$	
		$\Xi_c^0 \to \Lambda^0 K^- \pi^+$	$\Xi_c^0 \to \Xi^- \pi^+$	$\Xi_c^+ \to \Lambda^0 K^- \pi^+ \pi^+$	$\Xi_c^+ \to \Xi^- \pi^+ \pi^+$
True-matched before correction		18273	3638	5733	13166
True-matched after correction		17457.13	3516.02	5456.94	12784.91
Corrected MC efficiency, ϵ_{MC} (%)		14.72	10.68	8.90	6.91
ϵ_{data} estimation on the MC sample per PID Cut (%)	**p of $\Lambda^0 \to p\pi$**	91.20 ± 0.73 (0.80)	92.73 ± 0.67 (0.72)	91.88 ± 0.72 (0.78)	92.42 ± 0.64 (0.69)
	prompt K	91.74 ± 1.80 $\boxed{(1.96)}$	-	93.35 ± 2.28 $\boxed{(2.44)}$	-
	1st prompt π	95.76 ± 0.13 (0.14)	94.49 ± 0.20 $\boxed{(0.21)}$	96.63 ± 0.12 (0.12)	94.71 ± 0.16 $\boxed{(0.17)}$
	2nd prompt π	-	-	97.14 ± 0.10 (0.10)	95.95 ± 0.13 (0.14)

Table 6.9.: Data/MC efficiency corrections and PID efficiency uncertainties. The related PID cuts per track were given in the final selection tables, table 6.6 for Ξ_c^0 modes and table 6.7 for Ξ_c^+ modes. The values in parentheses represent the corresponding relative uncertainties (in %), and the values boxed in cyan color correspond to the PID systematic uncertainties going into $r(\Xi_c^{0\{+\}})$, as discussed in the main text.

the correction weights were applied on the remaining events[2]. The corrected efficiencies of all Ξ_c modes are summarized in table 6.9 along with the number of true-matched events before and after the corrections. The estimated PID uncertainties in ϵ_{data} were obtained by calibrating the efficiency of the control modes in data to our final selection. As a conservative approach, both, the statistical and systematic uncertainties of each PID selection has been added in quadrature. The treatment of these uncertainties in the ratio $r(\Xi_c^{0\{+\}})$ is discussed in Sec. 6.6.3.

6.6.2. Statistical Uncertainty

Using the fit results of Eq. (6.13) and Eq. (6.17) in conjunction with the nominal value of the corrected MC efficiencies and the nominal value of $\mathcal{B}(\Xi^- \to \Lambda\pi^-)$, we obtain

$$r(\Xi_c^0) = 0.817 \pm 0.048_{\text{stat}} \tag{6.24}$$

and

$$r(\Xi_c^+) = 0.308 \pm 0.024_{\text{stat}}\,, \tag{6.25}$$

where the statistical uncertainties originate solely from the N_{fit} results. The uncertainty from $\mathcal{B}(\Xi^- \to \Lambda\pi^-)$ will be treated as a systematic uncertainty source. Before the ratio results can be written in full, we summarize the various sources of systematic uncertainties.

[2] The overlap was found to be between 60 to 70 signal events, i.e., 0.3% to 2% per mode. In data, only 2 to 7 events were found to overlap between modes.

6.6.3. Systematic Uncertainties

MC Statistics

Systematic uncertainties in ϵ_{MC} arise from the finite size of the MC sample and are represented by binomial statistics, such that,

$$\Delta\epsilon_{\mathrm{MC}} = \sqrt{\frac{\epsilon_{\mathrm{MC}}(1-\epsilon_{\mathrm{MC}})}{\#\ \text{True MC events}}}, \tag{6.26}$$

where the number of true MC events are 118598 for $\Xi_c^0 \to \Lambda^0 K^- \pi^+$, 32919 for $\Xi_c^0 \to \Xi^- \pi^+$, 61322 for $\Xi_c^+ \to \Lambda^0 K^- \pi^+ \pi^+$, and 185083 for $\Xi_c^+ \to \Xi^- \pi^+ \pi^+$. This results in a relative uncertainty, $\Delta\epsilon_{\mathrm{MC}}/\epsilon_{\mathrm{MC}}$, of 0.70%, 1.59%, 1.29% and 0.85%, respectively.

PID Uncertainties

The uncertainties in the estimate of ϵ_{data} per PID cut, shown in table 6.9, are fed into our calculation of $r(\Xi_c^{0\{+\}})$ as systematic uncertainties. Following a similar approach as done in a Belle analysis of these ratios [72], we assume the proton identification uncertainties to cancel out and take the highest uncertainties for the pions, adding them linearly with the uncertainties of the kaon PID for every ratio. The relevant relative uncertainties are boxed in cyan in table 6.9.

External Branching Fraction

As previously mentioned, the branching fraction $\mathcal{B}(\Xi^- \to \Lambda\pi^-) = (99.89 \pm 0.04)\%$ [6] is used as an external measure for $r(\Xi_c^{0\{+\}})$. Its relative uncertainty, 0.04%, flows into our calculations as a systematic uncertainty.

Fit Model Uncertainties

Background PDF: Given that all the fit parameters are floated in our fit to the data, to quantify the uncertainties from the choice of the PDF model shape, we replace the background PDF from an exponential function to a first or second order polynomial, $f(M_{\Xi_c}) = \mathcal{N} \cdot \sum_i a_i M_{\Xi_c}^i$, where i represents the order of the polynomial, a_i is a floating coefficient and $\mathcal{N}$ is the normalization constant of the PDF. The uncertainties in yield from signal and background with respect to the original yield values are taken as systematic uncertainties. The background PDF in the $\Xi_c^0 \to \Lambda^0 K^- \pi^+$ and $\Xi_c^+ \to \Lambda^0 K^- \pi^+ \pi^+$ modes is replaced with a second order polynomial, while the background PDF in $\Xi_c^0 \to \Xi^- \pi^+$ and $\Xi_c^+ \to \Xi^- \pi^+ \pi^+$ is replaced with a first order polynomial. The results are given in table 6.10 in the columns corresponding to "New background PDF".

Signal PDF: Similarly, we quantify the uncertainties due to the mass resolution in the signal yield by replacing the original Gaussian PDF for the signal distribution in data with a convolved Gaussian PDF with a fixed (core) width from MC. This is a similar approach as taken in [72] and [73]. The uncertainty in the yields with respect to the original yields are taken as systematic uncertainties associated with uncertainties in the mass resolution. The results are given in table 6.10 in the columns corresponding to "New Signal PDF".

	Original PDF		New Background PDF			New Signal PDF			Fit Range ±20 MeV/c²	Total rel. unc. (%)
	N_{sig}	N_{bkg}	N_{sig}	N_{bkg}	rel. unc. (%)	N_{sig}	N_{bkg}	rel. unc. (%)	rel. unc. (%)	
$r(\Xi_c^0)$:										
$\Xi_c^0 \to \Lambda^0 K^- \pi^+$	2518	72527	2514	72532	0.08	2342	72703	3.50	0.69	3.57
$\Xi_c^0 \to \Xi^- \pi^+$	2235	7364	2227	7371	0.19	2252	7347	0.40	1.01	1.10
$r(\Xi_c^+)$:										
$\Xi_c^+ \to \Lambda^0 K^- \pi^+ \pi^+$	1044	26043	1039	26046	0.24	1003	26084	1.97	2.76	3.40
$\Xi_c^+ \to \Xi^- \pi^+ \pi^+$	2626	9752	2625	9753	0.02	2663	9716	0.73	0.52	0.90

Table 6.10.: Systematic uncertainties from the fit model. The high systematic uncertainties in the fit model are attributed to the fixed (core) widths from MC, which are summarized in table 6.8.

Note that the highest systematic uncertainties due to the signal PDF model come from the fixed MC widths in the modes $\Xi_c^0 \to \Lambda^0 K^- \pi^+$ and $\Xi_c^+ \to \Lambda^0 K^- \pi^+ \pi^+$.

Fit Range: To assert the uncertainties due to the choice of the fit range, we vary the selected mass region by ±20 MeV. The uncertainty in the signal yield is calculated as, $\Delta_{\text{sig}} = |N^+_{\text{sig}} - N^-_{\text{sig}}|/2$, and similarly the uncertainty in the background yield is calculated as, $\Delta_{\text{bkg}} = |N^+_{\text{bkg}} - N^-_{\text{bkg}}|/2$. Then, the systematic uncertainty in the original signal yield due to the fit range reads

$$\frac{\Delta_{\text{Yield}}}{N_{\text{sig}}} = \sqrt{\sum_{j=\text{sig, bkg}} \left(\frac{\Delta_j}{N_j}\right)^2} . \tag{6.27}$$

The relative uncertainties for each mode are summarized in table 6.10.

Tracking Uncertainties

Another source of systematic uncertainties to be included is due to imperfect tracking. From a study performed at Belle II using $e^+e^- \to \tau^+\tau^-$ events, a systematic uncertainty of 0.27% per track is recommended [74][3]. This uncertainty accounts for the systematic uncertainties in the Belle II tracking algorithms, covering a track momentum range of 200 MeV to 3.5 GeV. The tracking uncertainty in each ratio is identical for the numerator mode and the denominator mode, thus the leading systematic uncertainty given to $r(\Xi_c^0)$ is 1.08%, and to $r(\Xi_c^+)$ is 1.35%.

[3]The systematic uncertainty recommendation of 0.27% per track is an update to the previous recommendation of 0.24% per track, which was based on proc13 run-independent MC samples (MC15ri). The new recommendation is based on proc13 run-dependent MC samples (MC15rd), which are of the sample type we use in the present analysis.

Summary of Systematic Uncertainties

A summary of the collection of systematic uncertainties going into $r(\Xi_c^{0\{+\}})$ is provided in table 6.11. For each ratio, the uncertainties due to the PDF shape, per numerator mode and per denominator mode, correspond to the results listed in table 6.10. The total MC statistics uncertainties are added in quadrature. The PID uncertainties are added linearly for the uncertainty in the kaon identification and the highest uncertainty in the pion identification. The tracking uncertainty corresponds to the leading systematic uncertainty of the participating modes. The uncertainties from the external branching fraction $\mathcal{B}(\Xi^- \to \Lambda\pi^-)$ are negligible but are included in the table.

Source \ Ratio	$r(\Xi_c^0) = \frac{\mathcal{B}(\Xi_c^0 \to \Lambda K^-\pi^+)}{\mathcal{B}(\Xi_c^0 \to \Xi^-\pi^+)}$	$r(\Xi_c^+) = \frac{\mathcal{B}(\Xi_c^+ \to \Lambda K^-\pi^+\pi^+)}{\mathcal{B}(\Xi_c^+ \to \Xi^-\pi^+\pi^+)}$
Numerator PDF	3.57	3.40
Denominator PDF	1.10	0.90
MC statistics	1.74	1.54
Particle Identification	2.17	2.61
Tracking	1.08	1.35
$\boldsymbol{\mathcal{B}(\Xi^- \to \Lambda\pi^-)}$	0.04	0.04
Total	4.78	4.84

Table 6.11.: Summary of systematic uncertainties going into the ratio of branching fractions. All the values are relative uncertainties and are given in percent (%).

6.6.4. Ratio Results and Discussion

$r(\Xi_c^0)$:

Putting together all the established results, i.e., completing Eq. (6.24) with the systematic uncertainties provided in table 6.11, the ratio of branching fractions, $r(\Xi_c^0)$, reads

$$\frac{\mathcal{B}(\Xi_c^0 \to \Lambda K^-\pi^+)}{\mathcal{B}(\Xi_c^0 \to \Xi^-\pi^+)} = 0.817 \pm 0.048_{\text{stat}} \pm 0.039_{\text{syst}} \,. \tag{6.28}$$

Comparing this result to the world average by the PDG, 1.02 ± 0.14 [6], we find to agree within 1.3σ, with a percent error of 20%. The latter ratio result is based on a measurement by Belle that dates back to 2005 [72], at the time, it was the first reported measurement of the ratio. Currently, the Belle measurement remains as the only measurement included in the PDG listings. A direct comparison to the Belle result, $1.07 \pm 0.12_{\text{stat}} \pm 0.07_{\text{syst}}$,

yields a 1.7σ agreement and a percent error of 24%. The reconstruction at Belle of the modes involved in $r(\Xi_c^0)$ yielded approximately 3000 signal events using a data set of 140 fb^{-1}. However, their reconstruction efficiencies are found to be lower than 8% for each mode, with relative statistical uncertainties in the yields of 7% to 8%. In the present thesis, we used a Belle II data set of 90.17 fb^{-1}, which yielded over 2518 signal events in $\Xi_c^0 \to \Lambda^0 K^- \pi^+$ and 2235 in $\Xi_c^0 \to \Xi^- \pi^+$, with a corrected reconstruction efficiency ($\epsilon_{\rm MC}$) of about 15% and about 11%, respectively. Our relative statistical uncertainties in the signal yields are 5% for $\Xi_c^0 \to \Lambda^0 K^- \pi^+$ and 3% for $\Xi_c^0 \to \Xi^- \pi^+$. In terms of precision, the measurement presented in this thesis improves the previous Belle result.
Notably, in 2019, Belle reported a first measurement of the absolute branching fractions for various Ξ_c^0 modes [75]. Comparing $r(\Xi_c^0)_{\rm theirs} = 0.65 \pm 0.18_{\rm stat} \pm 0.04_{\rm syst}$ to our result, we find agreement within 1σ.

$r(\Xi_c^+)$:

Completing Eq. (6.25) with the systematic uncertainties provided in table 6.11, our result for $r(\Xi_c^+)$ reads

$$\frac{\mathcal{B}(\Xi_c^+ \to \Lambda K^- \pi^+ \pi^+)}{\mathcal{B}(\Xi_c^+ \to \Xi^- \pi^+ \pi^+)} = 0.308 \pm 0.024_{\rm stat} \pm 0.015_{\rm syst}. \tag{6.29}$$

Our measurement of this ratio is in very good agreement with the world average reported by the PDG, 0.323 ± 0.033 [6], at 0.3σ and with a percent error of 5%. In table 6.12, we present a list of independent measurements used for the PDG world average. Similar to $r(\Xi_c^0)$, the last reported measurement of $r(\Xi_c^+)$ is attributed to the 2005 Belle measurement. The measurements by FOCUS and CLEO were carried on a data sample yielding 100 (numerator) to 300 (denominator) signal events, while at Belle and in the present thesis, 1000 (numerator) to 3000 (denominator) signal events were treated.

Experiment	$r(\Xi_c^+)$	Method	Year
Belle	$0.32 \pm 0.03 \pm 0.02$	e^+e^-, $\Upsilon(4S)$	2005 [72]
FOCUS	$0.28 \pm 0.06 \pm 0.06$	γ-Nucleus, 180 GeV	2003 [76]
CLEO	$0.58 \pm 0.16 \pm 0.07$	e^+e^-, $\Upsilon(4S)$	1996 [77]

Table 6.12.: Independent measurements of $r(\Xi_c^+)$ used in the current world average by the PDG [6].

7. Summary and Conclusion

In this thesis, we studied the singly charmed baryons of the $J^P = 1/2^+$ $\overline{3}_\mathrm{A}$-plet (Λ_c^+, Ξ_c^0 and Ξ_c^+) in five different modes:

$$\Lambda_c^+ \to pK^-\pi^+, \tag{7.1}$$
$$\Xi_c^0 \to \Lambda^0 K^-\pi^+, \tag{7.2}$$
$$\Xi_c^0 \to \Xi^-\pi^+, \tag{7.3}$$
$$\Xi_c^+ \to \Lambda^0 K^-\pi^+\pi^+, \tag{7.4}$$
$$\Xi_c^+ \to \Xi^-\pi^+\pi^+. \tag{7.5}$$

We reconstructed these charmed baryon decays using Belle II data from collisions of the type $e^+e^- \to \Upsilon(4S) \to B\overline{B}$ and $e^+e^- \to q\overline{q}$ ($q = u, d, s, c$), and we worked on achieving an optimal selection of candidates. The optimizations were carried out on Monte Carlo (MC) samples of different sizes, depending on the mode. For $\Lambda_c^+ \to pK^-\pi^+$, we used (up to) $65.52\,\mathrm{fb}^{-1}$ ($16.50\,\mathrm{fb}^{-1}$ in data), and for the Ξ_c modes we used $356.70\,\mathrm{fb}^{-1}$ ($90.17\,\mathrm{fb}^{-1}$ in data). The selection of $\Lambda_c^+ \to pK^-\pi^+$ candidates was optimized based on the signal significance, i.e., the figure of merit (FOM), for various variables associated with the charged tracks p, K, and π. Charm contamination sources were vetoed and data/MC PID efficiency corrections were applied. An x_p-dependent binned fit revealed a clear separation between signal events originating from $B\overline{B}$ events and signal events originating from $c\overline{c}$ fragmentation. Subsequently, the reconstruction of the Ξ_c modes was carried out using an MC sample of $c\overline{c}$ fragmentation, with the condition $x_p > 0.4$. Because of the similarities across all Ξ_c modes, the loose selections and optimizations were discussed collectively. The final selection criteria were determined by optimizing the FOM of the PID variables associated with both the prompt tracks and hyperon daughter tracks. Another selection that contributed to the FOM performance was a cut on the flight significance of the hyperons.
Data events were reconstructed and the MC-derived final selection criteria was applied. In the fit to the invariant mass distributions in data, all the fit parameters were floated, i.e., no inputs from MC were used other than the overall PDF shape. The procedure for calculating the ratio of branching fractions was discussed, and among other considerations, the MC efficiency for each mode was corrected. Various sources of uncertainties were addressed and incorporated into the final results. Our final result for the first measured ratio of branching fractions, reads

$$\frac{\mathcal{B}(\Xi_c^0 \to \Lambda K^-\pi^+)}{\mathcal{B}(\Xi_c^0 \to \Xi^-\pi^+)} = 0.817 \pm 0.048_\mathrm{stat} \pm 0.039_\mathrm{syst}, \tag{7.6}$$

which is within 1.3σ agreement with the world average reported by the Particle Data Group (PDG), 1.02 ± 0.14 [6]. The PDG result is based on a 2005 Belle measurement

[72]. Comparing our result to a more recent Belle measurement, published in 2019, $0.65 \pm 0.18_{\text{stat}} \pm 0.04_{\text{syst}}$ [75], we find agreement within 1σ.
Our second measured ratio of branching fractions reads

$$\frac{\mathcal{B}(\Xi_c^+ \to \Lambda K^- \pi^+ \pi^+)}{\mathcal{B}(\Xi_c^+ \to \Xi^- \pi^+ \pi^+)} = 0.308 \pm 0.024_{\text{stat}} \pm 0.015_{\text{syst}}, \tag{7.7}$$

which is in very good agreement with the world average reported by the PDG, 0.323 ± 0.033 [6], at 0.3σ. This PDG result is based on the 2005 Belle measurement [72], measurements by FOCUS in 2003 [76] and measurements by CLEO in 1996 [77].

7.1. Outlook

Significant progress has been made over the past decade in the study of charmed baryons, particularly by Belle (II), BESIII, and the LHCb. The first absolute branching fraction, $\mathcal{B}(\Lambda_c^+ \to pK^-\pi^+)$, was measured by Belle [78] and BESIII [79]. The first absolute branching fractions of three Ξ_c^0 modes and two Ξ_c^+ modes were measured by Belle [75, 80]. The lifetime of Λ_c^+ was measured by Belle II with unprecedented precision [66]. The doubly charmed baryon Ξ_{cc}^{++} was observed by the LHCb [5]. Additionally, new excited states and ratios of branching fractions have been measured.

Understanding the excited spectrum, CP violation in the baryon sector, and the transition from the perturbative to the non-perturbative regime in QCD remain significant challenges. Many answers are likely to be found through the precise characterization of charmed baryons. Progress in the spectroscopy of heavy baryons also contributes to our understanding of the internal structure of light baryons, such as the proton and the neutron [20]. With the planned collection of $50\,\text{ab}^{-1}$ of data at Belle II in the coming years—over 550× the amount of data used in the present thesis—substantial insights into these unknowns are expected to be gained.

A. Gell-Mann matrices

A common matrix representation for $SU(3)$ transformations are the Gell-Mann matrices, [9, p. 225]

$$\lambda_1 = \begin{pmatrix} 0 & 1 & 0 \\ 1 & 0 & 0 \\ 0 & 0 & 0 \end{pmatrix}, \quad \lambda_2 = \begin{pmatrix} 0 & -i & 0 \\ i & 0 & 0 \\ 0 & 0 & 0 \end{pmatrix}, \quad \lambda_3 = \begin{pmatrix} 1 & 0 & 0 \\ 0 & -1 & 0 \\ 0 & 0 & 0 \end{pmatrix}, \quad \lambda_4 = \begin{pmatrix} 0 & 0 & 1 \\ 0 & 0 & 0 \\ 1 & 0 & 0 \end{pmatrix},$$

$$\lambda_5 = \begin{pmatrix} 0 & 0 & -i \\ 0 & 0 & 0 \\ i & 0 & 0 \end{pmatrix}, \quad \lambda_6 = \begin{pmatrix} 0 & 0 & 0 \\ 0 & 0 & 1 \\ 0 & 1 & 0 \end{pmatrix}, \quad \lambda_7 = \begin{pmatrix} 0 & 0 & 0 \\ 0 & 0 & -i \\ 0 & i & 0 \end{pmatrix}, \quad \lambda_8 = \frac{1}{\sqrt{3}} \begin{pmatrix} 1 & 0 & 0 \\ 0 & 1 & 0 \\ 0 & 0 & -2 \end{pmatrix}.$$

The two simultaneously diagonalisable matrices are λ_3 and λ_8. Since the generator expressions $\frac{1}{2}\lambda_3$ and $\frac{1}{2}\lambda_8$ commute (and are therefore compatible observables), the third component isospin is defined as $I_3 = \frac{1}{2}\lambda_3$, and the hypercharge is defined as $Y = \frac{1}{\sqrt{3}}\lambda_8$.

B. Λ_c^+ Distributions

B.1. PID efficiency corrections

For tracks of $\Lambda_c^+ \to pK^-\pi^+$, the PID efficiency correction coverage, in bins of θ and p, is illustrated in Fig. B.1 for each particle type and charge sign. The top figures (a-f) demonstrate the coverage for the PID efficiency of each reconstructed charged particle (p, K, π) and the lower figures (f-n) demonstrate the coverage for the PID fakes where the pion fakes the proton or kaon track, or the kaon fakes the pion or proton track. Not included here is the rate at which the proton fakes a pion or a kaon track as it is negligible [57].
We can concede from Fig. B.1(c) and Fig. B.1(f) that the PID efficiency-correction coverage, i.e., the weight production, is well suited for the proton and the kaon candidates, but not the pion. The requirement $\text{pion}_p > 0.4\,\text{GeV/c}$ thus ensures that the distribution shape comparison between the corrected MC and data are on par with each other.

PID-Efficiency Coverage

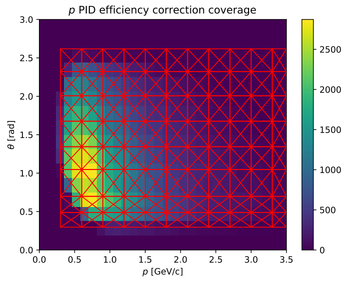

(a) p

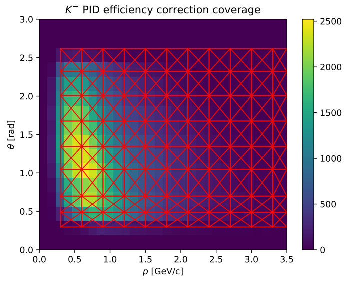

(b) K^-

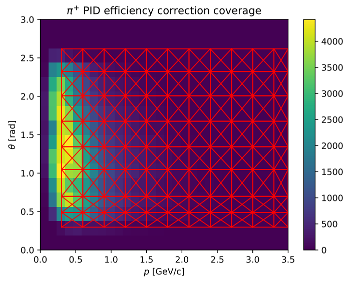

(c) π^+

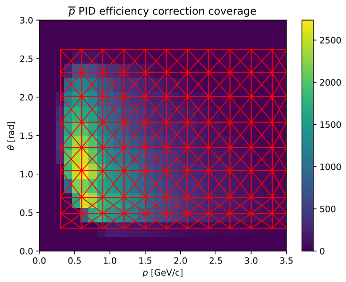

(d) $\overline{p}$

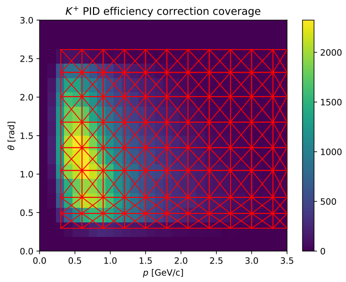

(e) K^+

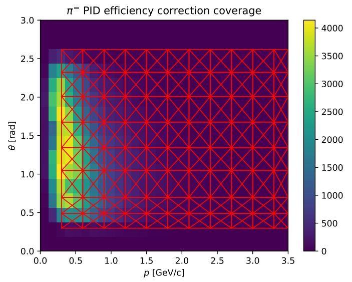

(f) π^-

PID-Fakes Coverage

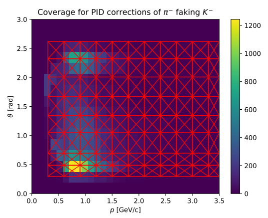

(g) π^- fakes K^-

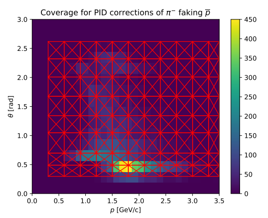

(h) π^- fakes $\overline{p}$

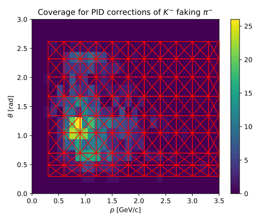

(i) K^- fakes π^-

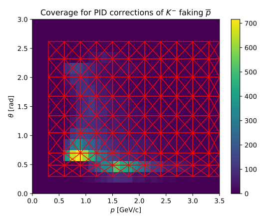

(j) K^- fakes $\overline{p}$

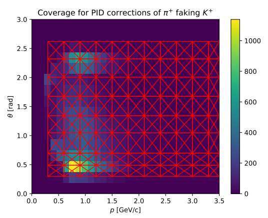

(k) π^+ fakes K^+

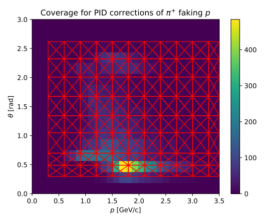

(l) π^+ fakes p

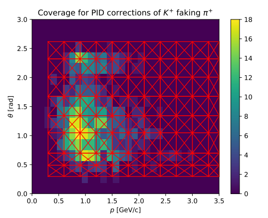

(m) K^+ fakes π^+

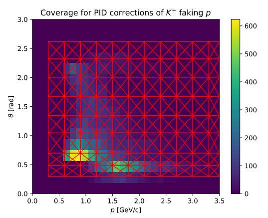

(n) K^+ fakes p

Figure B.1.: The weight production coverage (red grid span) per particle type and charge sign as functions of their momentum p and their polar angle θ. The bar on the right side of each plot indicates the number of events in each (θ, p) bin.

B.2. N-1 plots for the final Λ_c^+ candidate selection

A check on our selection criteria—composed of N cut variables—involves displaying the distribution of candidate events as a function of 1 cut variable (one at a time) while the other $N-1$ cuts are in place. For example, an N-1 plot displaying the proton$_{ID}$ distribution contains Λ_c^+ events that pass all the cuts except for the one plotted, i.e., the proton$_{ID}$ cut is not applied. Using N-1 plots, we show the data/MC agreement in a larger variable spectrum than the one retained by the full set of cuts.
A plot of a distribution where a cut is omitted is only sensible for variables that were reconstructed with a looser cut than the one kept in the final selection of candidates. Because the loose selection of candidates in the $65.52\,\mathrm{fb}^{-1}$ MC sample involves a kaon$_{ID}$ > 0.1 and a pion$_{ID}$ > 0.1 that are also kept as such in the final selection, the N-1 plots for these variables are not considered. The same argument applies for all the other variables where the loose cuts are kept in the final selection. In the case of the proton$_{ID}$, the reconstruction using the $65.52\,\mathrm{fb}^{-1}$ MC sample was carried out with a loose cut, proton$_{ID}$ > 0.1, thus it is included in the plots.
In Fig. B.2, we show the distributions of MC versus data, where the MC distributions are scaled down by a factor

$$l_{\text{scale}} = \frac{16.50\,\mathrm{fb}^{-1}}{65.52\,\mathrm{fb}^{-1}} = 0.252. \tag{B.1}$$

The plots are shown for the picked set of cut variables in the order that they were presented in Sec. 5.3:

- the proton identification, proton$_{ID}$, discussed in Sec. 5.3.2,
- the vetoed mass range given by the variable, $M(\pi^+K^-\pi^+)$, discussed in Sec. 5.3.3,
- the proton transverse momentum, proton$_{p_T}$, discussed in Sec. 5.3.4,
- and the momentum of the pion, pion$_p$, discussed in 5.3.5.

For better visibility of the comparison between MC and the data, the variable plot ranges shown in Fig. B.2 have been truncated.
Although the MC distributions generally follow the behavior seen in data, some discrepancies can be noted.

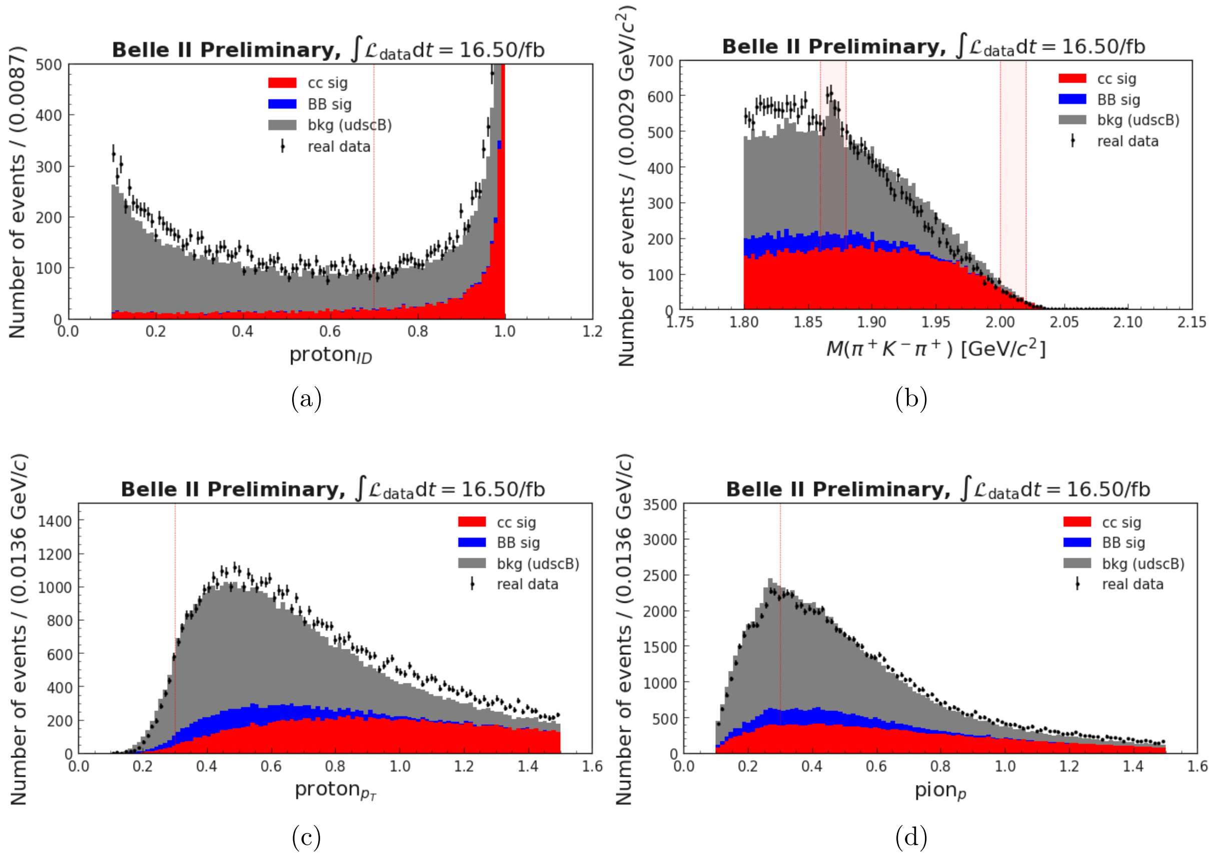

Figure B.2.: N-1 plots for (a) the proton identification, proton$_{ID}$, (b) the veto of events where the proton is given a pion hypothesis, (c) the transverse momentum of the proton, proton$_{p_T}$, and (d) the momentum of the pion, pion$_p$. The red vertical lines signify the regions where the cut is applied for the final selection of candidates. Every candidate below a red vertical line or between two red vertical lines, are removed in the final selection. These distributions display the comparison between MC and the data for candidate events where all the selection cuts are applied except for the one plotted. The error bars denote the standard Poisson error in the data.

C. Empirical Approach to the 'xp-problem'

During the development of this thesis, in a Belle II note [68] (published internally) an empirical parametrisation scheme for the shape of the x_p distributions of charmed baryons was suggested, which addresses the mismatch between the shape of the MC signal production and data yields. The parametrisation is based on the PDF functions given in Eq. (C.1) and Eq. (C.2).

$$\mathrm{PDF}_1(x_p) = \frac{1}{A} x_p (1 - x_p) \cdot e^{\alpha(1-x_p)+\beta(1-x_p)^2} \tag{C.1}$$

$$\mathrm{PDF}_2(x_p) = \frac{1}{A}(1 - x_p)^{\alpha} x_p^{\beta} \tag{C.2}$$

The fit over the x_p distribution of the data yields $N_{\mathrm{fit}}/\epsilon$—see Fig. 5.8 for reference—is done using Eq. (C.1), whereas the fit over the true MC distribution is done with Eq. (C.2), as it is a better fit for its shape. The results of the fits to our data yields and generated signal MC, with $x_p > 0.4$, are summarized in table C.1.
This procedure involves reconstructing events (again) with a random x_p-sampling that best resembles the shape seen in the efficiency-corrected data. For the reconstruction, we only accept generated MC events that obey the following inequality,

$$\texttt{random}(0,1) \cdot \mathrm{PDF}_{\mathrm{gen}} < C \cdot \mathrm{PDF}_{\mathrm{data}}, \tag{C.3}$$

In our case, $\mathrm{PDF}_{\mathrm{gen}} \equiv \mathrm{PDF}_2$, i.e., it represents the model for the generation of true MC events retrieved from our fit to the originally generated true MC distribution. $\mathrm{PDF}_{\mathrm{data}} \equiv \mathrm{PDF}_1$, i.e., it is the model that represents the shape of our efficiency-corrected data yields. The optimal factor C accommodates the MC signal generation to the shape seen in the efficiency-corrected data, $C \cdot \mathrm{PDF}_{\mathrm{data}}$ is then the "x_p-sampling PDF", see Fig. C.1. From our fits, we get $C = 0.94$.
In this manner, with $x_p > 0.4$, the disagreement between the shape in data vs. MC is resolved for $\Lambda_c^+ \to pK^-\pi^+$.

Distribution	PDF	A	α	β
$N_{\mathrm{fit}}/\epsilon$	PDF_1	4.5	14.6 ± 1.1	-17.9 ± 1.3
True MC	PDF_2	0.03	1.92 ± 0.06	3.17 ± 0.10

Table C.1.: Fit results using Eq. (C.1) and Eq. (C.2). The fit is done with all the final selections applied and $x_p > 0.4$.

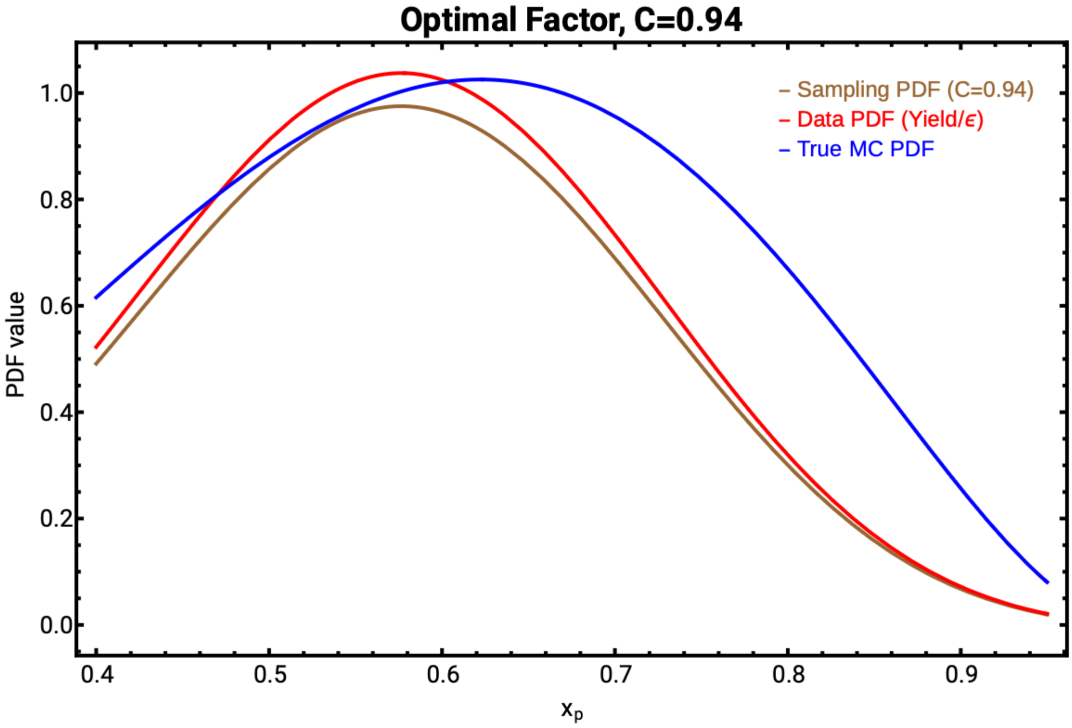

Figure C.1.: Extraction of the optimal factor C that accommodates the MC signal generation to the shape of the efficiency-corrected data yields, for $x_p > 0.4$.

List of Tables

List of Figures

Bibliography

[1] J. E. Augustin et al. *Discovery of a Narrow Resonance in e^+e^- Annihilation*. Vol. 33. Phys. Rev. Lett., 1974, pp. 1406–1408. DOI: 10.1103/PhysRevLett.33.1406.

[2] Samuel C.C. Ting. *The Discovery of the J Particle: A Personal Recollection*. Nobel Prize Lecture. December 11, 1976. URL: https://www.nobelprize.org/prizes/physics/1976/ting/lecture/. Last visited Sat. 15 Mar 2025.

[3] Burton Richter. *From the psi to charm - The experiments of 1975 to 1976*. Nobel Lecture, December 1976.

[4] Murray Gell-Mann. *The Eightfold Way: A Theory of strong interaction symmetry*. CTSL-20, TID-12608, Mar. 1961. DOI: 10.2172/4008239.

[5] R. Aaij et al. *Observation of the Doubly Charmed Baryon Ξ_{cc}^{++}*. Vol. 119. American Physical Society, Sept. 2017, p. 112001. DOI: 10.1103/PhysRevLett.119.112001. URL: https://link.aps.org/doi/10.1103/PhysRevLett.119.112001.

[6] S. Navas et al. *Review of particle physics*. Vol. 110. 3. Phys. Rev. D, 2024, p. 030001. DOI: 10.1103/PhysRevD.110.030001.

[7] Franz Gross et al. *50 Years of quantum chromodynamics*. Vol. 83. 12. The European Physical Journal C, 2023, p. 1125. ISBN: 1434-6052. DOI: 10.1140/epjc/s10052-023-11949-2. URL: https://doi.org/10.1140/epjc/s10052-023-11949-2.

[8] Robert D. Klauber. *Student friendly quantum field theory: Basic principles and quantum electrodynamics*. Sandtrove Press, Fairfield, Iowa, 2013. ISBN: 9780984513956. 2nd Edition with corrections, May 2014.

[9] Mark Thomson. *Modern Particle Physics*. Cambridge University Press, 2013. DOI: 10.1017/CBO9781139525367.

[10] M. E. Peskin and D. V. Schroeder. *An Introduction to Quantum Field Theory*. CRC Press, 1995.

[11] Jorge C. Romão and João P. Silva. *A resource for signs and Feynman diagrams of the Standard Model*. Vol. 27. 26. World Scientific Pub Co Pte Lt, Oct. 2012, p. 1230025. DOI: https://doi.org/10.1142/s0217751x12300256.

[12] Helmut Eberl. *Introduction to Models of Elementary Particle Physics II*. TU Wien Lecture, 141.B00, 2023. URL: https://tiss.tuwien.ac.at/course/courseDetails.xhtml?courseNr=141B02&semester=2023S&dswid=4631&dsrid=154.

[13] The Nobel Prize in Physics 1979. *NobelPrize.org*. Nobel Prize Outreach AB 2024, Tue. 27 Feb 2024. URL: https://www.nobelprize.org/prizes/physics/1979/summary/.

[14] Cush. *Standard Model of elementary particles*. Wikimedia Commons. CC BY 3.0. Last visited Feb. 19, 2025. URL: https://commons.wikimedia.org/wiki/File:Standard_Model_of_Elementary_Particles.svg.

[15] Makoto Kobayashi and Toshihide Maskawa. *CP-Violation in the Renormalizable Theory of Weak Interaction*. Vol. 49. 2. Progress of Theoretical Physics, Feb. 1973, pp. 652–657. DOI: 10.1143/PTP.49.652.

[16] Nicola Cabibbo. *Unitary Symmetry and Leptonic Decays*. Vol. 10. American Physical Society, June 1963, pp. 531–533. DOI: 10.1103/PhysRevLett.10.531.

[17] S. L. Glashow, J. Iliopoulos, and L. Maiani. *Weak Interactions with Lepton-Hadron Symmetry*. Vol. 2. American Physical Society, Oct. 1970, pp. 1285–1292. DOI: 10.1103/PhysRevD.2.1285.

[18] The Nobel Prize in Physics 2008. *NobelPrize.org*. Nobel Prize Outreach AB 2024, Tue. 27 Feb 2024. URL: https://www.nobelprize.org/prizes/physics/2008/summary/.

[19] William Fulton. *Young Tableaux: With Applications to Representation Theory and Geometry*. London Mathematical Society Student Texts. Cambridge University Press, 1996. DOI: https://doi.org/10.1017/CBO9780511626241.

[20] Volker Crede and John Yelton. *70 years of hyperon spectroscopy: a review of strange Ξ, $\boldsymbol{\Omega}$ baryons, and the spectrum of charmed and bottom baryons*. Vol. 87. 10. IOP Publishing, Sept. 2024, p. 106301. DOI: 10.1088/1361-6633/ad7610. URL: https://dx.doi.org/10.1088/1361-6633/ad7610.

[21] Jean-Marc Richard. *An introduction to the quark model*. 2012. arXiv: 1205.4326 [hep-ph]. URL: https://arxiv.org/abs/1205.4326.

[22] T. J. Moon et al. *First determination of the spin and parity of the charmed-strange baryon, $\Xi_c(2970)^+$*. Vol. 103. 11. American Physical Society (APS), June 2021. DOI: 10.1103/physrevd.103.l111101. URL: http://dx.doi.org/10.1103/PhysRevD.103.L111101.

[23] S. Kurokawa and E. Kikutani. *Overview of the KEKB accelerators*. Vol. 499. 1. KEK-B: The KEK B-factory. Nuclear Instruments, Methods in Physics Research Section A: Accelerators, Spectrometers, Detectors, and Associated Equipment, 2003, pp. 1–7. DOI: https://doi.org/10.1016/S0168-9002(02)01771-0. URL: https://www.sciencedirect.com/science/article/pii/S0168900202017710.

[24] A. Abashian et al. *The Belle detector*. Vol. 479. 1. Detectors for Asymmetric B-factories. Nuclear Instruments, Methods in Physics Research Section A: Accelerators, Spectrometers, Detectors, and Associated Equipment, 2002, pp. 117–232. DOI: https://doi.org/10.1016/S0168-9002(01)02013-7. URL: https://www.sciencedirect.com/science/article/pii/S0168900201020137.

[25] Kazunori Akai, Kazuro Furukawa, Haruyo Koiso. *SuperKEKB collider*. Nuclear Instruments, Methods in Physics Research Section A: Accelerators, Spectrometers, Detectors, and Associated Equipment. Volume 907, Pages 188-199, ISSN 0168-9002, 2018. DOI: https://doi.org/10.1016/j.nima.2018.08.017.

[26] Z. Dolezal, S. Uno. *Belle II Technical Design Report*. BELLE2-REPORT-2016-001, Oct. 2010.

[27] E Kou et al. *The Belle II Physics Book*. Progress of Theoretical and Experimental Physics, Volume 2019, Issue 12, 123C01, December 2019. DOI: https://doi.org/10.1093/ptep/ptz106.

[28] Werner Herr and Bruno D. Muratori. *Concept of luminosity*. CERN Accelerator School, 2006. URL: https://api.semanticscholar.org/CorpusID:34280714.

[29] K. Shibata. *Status and schedule of SuperKEKB*. Semantic Scholar, 2012. URL: https://api.semanticscholar.org/CorpusID:10926839.

[30] Institute of Particle and Nuclear Studies. NEWS. Last visited on January 21, 2025. URL: https://www2.kek.jp/ipns/en/news/7015/.

[31] H. Aihara et al. *The Belle II Detector Upgrades Framework Conceptual Design Report*. 2024. arXiv: 2406.19421 [hep-ex]. URL: https://arxiv.org/abs/2406.19421.

[32] Helmut Wiedemann. "Overview of Synchrotron Radiation". *Particle Accelerator Physics*. Cham: Springer International Publishing, 2015, pp. 815–855. ISBN: 978-3-319-18317-6. DOI: 10.1007/978-3-319-18317-6_24. URL: https://doi.org/10.1007/978-3-319-18317-6_24.

[33] Belle II Software Group. *Belle II Software Documentation*. Release light-2409-toyger. Belle II Collaboration, visited January 31, 2025. URL: https://software.belle2.org/light-2409-toyger/sphinx.

[34] Takanori Hara, Thomas Kuhr, and Yutaka Ushiroda. *Belle II Coordinate System and Guideline of Belle II Numbering Scheme*. Belle II Publications, BELLE2-NOTE-TE-2015-009 (internal). Alternative URL: https://indico.mpp.mpg.de/event/2308/contributions/4092/attachments/3414/3799/Belle2NumberingScheme.pdf. 2011.

[35] Valerio Bertacchi et al. *Track finding at Belle II*. Vol. 259. Computer Physics Communications, 2021, p. 107610. DOI: https://doi.org/10.1016/j.cpc.2020.107610. URL: https://www.sciencedirect.com/science/article/pii/S0010465520302861.

[36] F. Simon et al. *The Belle-II Pixel Vertex Detector at the SuperKEKB Flavor Factory*. 2010. arXiv: 1002.1007 [physics.ins-det]. URL: https://arxiv.org/abs/1002.1007.

[37] J. Kemmer and G. Lutz. *New detector concepts*. Vol. 253. 3. Nuclear Instruments, Methods in Physics Research Section A: Accelerators, Spectrometers, Detectors, and Associated Equipment, 1987, pp. 365–377. DOI: https://doi.org/10.1016/0168-9002(87)90518-3. URL: https://www.sciencedirect.com/science/article/pii/0168900287905183.

[38] Matej Srebre et al. *Generation of Belle II Pixel Detector Background Data with a GAN*. Vol. 245. EPJ Web of Conferences, Jan. 2020, p. 02010. DOI: 10.1051/epjconf/202024502010.

[39] L. Zani et al. *The Silicon Vertex Detector of the Belle II experiment*. Vol. 1038. Elsevier BV, Sept. 2022, p. 166952. DOI: 10.1016/j.nima.2022.166952. URL: http://dx.doi.org/10.1016/j.nima.2022.166952.

[40] Henrikas Svidras. *The Central Drift Chamber of Belle 2*. 5th Belle II Starterkit Workshop. January 30, 2020. URL: https://indico.belle2.org/event/1307/contributions/6445/attachments/3717/5649/CDC_B2SK.pdf.

[41] N. Taniguchi. "Central Drift Chamber for Belle-II". *Journal of Instrumentation* 12.06 (June 2017), p. C06014. DOI: 10.1088/1748-0221/12/06/C06014. URL: https://dx.doi.org/10.1088/1748-0221/12/06/C06014.

[42] I. Adachi et al. *sBelle Design Study Report*. 2008. arXiv: 0810.4084 [hep-ex]. URL: https://arxiv.org/abs/0810.4084.

[43] Rok Pestotnik et al. *Calibration of the Belle II Aerogel Ring Imaging Detector*. Oct. 2018. URL: https://docs.belle2.org/files/3469/BELLE2-CONF-PROC-2018-022/1/BELLE2-CONF-PROC-2018-022.pdf.

[44] Belle-ECL et al. “Electromagnetic calorimeter for Belle II”. *Journal of Physics: Conference Series* 587.1 (Feb. 2015), p. 012045. DOI: 10.1088/1742-6596/587/1/012045. URL: https://dx.doi.org/10.1088/1742-6596/587/1/012045.

[45] A. Kaplan and A. Taddy. *Hadronic Showers*. KIP Journal Club: Calorimetry and Jets. Last visited Feb. 7, 2025. URL: https://www.kip.uni-heidelberg.de/atlas/seminars/WS2009_JC/hadron_showers.pdf.

[46] T. Uglov. “K-long and muon system for the Belle II experiment”. *Journal of Instrumentation* 12.07 (July 2017), p. C07035. DOI: 10.1088/1748-0221/12/07/C07035. URL: https://dx.doi.org/10.1088/1748-0221/12/07/C07035.

[47] David J. Lange. *The EvtGen particle decay simulation package*. Nuclear Instruments, Methods in Physics Research Section A: Accelerators, Spectrometers, Detectors, and Associated Equipment, Volume 462, Issues 1–2, Pages 152-155, ISSN 0168-9002, 2001. DOI: https://doi.org/10.1016/S0168-9002(01)00089-4.

[48] B.F.L. Ward, S. Jadach, Z. Was. *Precision calculation for e+e → 2f: the KK MC project*. Nuclear Physics B - Proceedings Supplements, Volume 116, Pages 73-77, ISSN 0920-5632, 2003. DOI: https://doi.org/10.1016/S0920-5632(03)80147-0.

[49] Torbjörn Sjöstrand, Stephen Mrenna, Peter Skands. *A brief introduction to PYTHIA 8.1*. Computer Physics Communications, Volume 178, Issue 11, Pages 852-867, ISSN 0010-4655, 2008. DOI: https://doi.org/10.1016/j.cpc.2008.01.036.

[50] Phillip Urquijo and Torben Ferber. *Overview of the Belle II Physics Generators*. Belle II Publications. BELLE2-NOTE-PH-2015-006. 2016. URL: https://docs.belle2.org/files/444/BELLE2-NOTE-PH-2015-006-v2/1/BELLE2-NOTE-PH-2015-006-v2.pdf.

[51] S. Agostinelli et al. *Geant4—a simulation toolkit*. Vol. 506. 3. Nuclear Instruments, Methods in Physics Research Section A: Accelerators, Spectrometers, Detectors, and Associated Equipment, 2003, pp. 250–303. DOI: https://doi.org/10.1016/S0168-9002(03)01368-8. URL: https://www.sciencedirect.com/science/article/pii/S0168900203013688.

[52] T. Kuhr et al. *The Belle II Core Software*. Vol. 3. 1. Computing and Software for Big Science, 2018, p. 1. ISBN: 2510-2044. DOI: 10.1007/s41781-018-0017-9. URL: https://doi.org/10.1007/s41781-018-0017-9.

[53] Rene Brun and Fons Rademakers. *ROOT — An object oriented data analysis framework*. Vol. 389. 1. New Computing Techniques in Physics Research V. Nuclear Instruments, Methods in Physics Research Section A: Accelerators, Spectrometers, Detectors, and Associated Equipment, 1997, pp. 81–86. DOI: https://doi.org/10.1016/S0168-9002(97)00048-X. URL: https://www.sciencedirect.com/science/article/pii/S016890029700048X.

[54] ROOT Team 2025. *ROOT Data Analysis Framework*. Visited Febuary 3, 2025. URL: https://root.cern.

[55] J.-F. Krohn et al. *Global decay chain vertex fitting at Belle II*. Vol. 976. Nuclear Instruments, Methods in Physics Research Section A: Accelerators, Spectrometers, Detectors, and Associated Equipment, 2020, p. 164269. DOI: https://doi.org/10.1016/j.nima.2020.164269. URL: https://www.sciencedirect.com/science/article/pii/S0168900220306653.

[56] Tadeas Bilka et al. *Implementation of GENFIT2 as an experiment independent track-fitting framework*. 2019. arXiv: 1902.04405 [physics.data-an]. URL: https://arxiv.org/abs/1902.04405.

[57] Belle II Collaboration. *Systematics Corrections Framework*. Last visited Feb. 11, 2025. URL: https://syscorrfw.readthedocs.io/en/latest/index.html.

[58] Todd Pedlar. *Studies of Proton Identification using Λ^0 decays in Early Phase III Data* $(6.4\,\mathrm{fb}^{-1})$ *and MC12*. Belle II Publications, BELLE2-NOTE-TE-2019-031, 2019.

[59] Umberto Tamponi. *Study of hadron-ID using untagged K_s*. Belle II Publications, BELLE2-NOTE-PH-2019-048, 2019.

[60] Saurabh Sandilya and Alan Schwartz. *Study of Kaon and Pion Identification Performances in Phase III data with D^{*+} sample*. Belle II Publications, BELLE2-NOTE-TE-2019-024, 2019.

[61] Cesare Bini. *Data analysis in Particle Physics*. 2017. URL: https://api.semanticscholar.org/CorpusID:202116589.

[62] Luca Lista. *Statistical Methods for Data Analysis in Particle Physics*. Springer Cham, 2016. DOI: https://doi.org/10.1007/978-3-319-20176-4.

[63] Wouter Verkerke and David Kirkby. *The RooFit toolkit for data modeling*. arXiv, 2003. eprint: physics/0306116 (physics.data-an). URL: https://arxiv.org/abs/physics/0306116.

[64] Roger Barlow. *Extended maximum likelihood*. Vol. 297. 3. Nuclear Instruments, Methods in Physics Research Section A: Accelerators, Spectrometers, Detectors, and Associated Equipment, 1990, pp. 496–506. DOI: https://doi.org/10.1016/0168-9002(90)91334-8. URL: https://www.sciencedirect.com/science/article/pii/0168900290913348.

[65] Steve Baker and Robert D. Cousins. *Clarification of the use of CHI-square and likelihood functions in fits to histograms*. Vol. 221. 2. Nuclear Instruments and Methods in Physics Research, 1984, pp. 437–442. DOI: https://doi.org/10.1016/0167-5087(84)90016-4. URL: https://www.sciencedirect.com/science/article/pii/0167508784900164.

[66] F. Abudinén et al. *Measurement of the Λ_c^+ Lifetime*. Vol. 130. American Physical Society, Feb. 2023, p. 071802. DOI: 10.1103/PhysRevLett.130.071802. URL: https://link.aps.org/doi/10.1103/PhysRevLett.130.071802.

[67] R. Seuster et al. *Charm hadrons from fragmentation and B decays in e^+e^- annihilation at $\sqrt{s} = 10.6$ GeV*. Vol. 73. American Physical Society, Feb. 2006, p. 032002. DOI: 10.1103/PhysRevD.73.032002. URL: https://link.aps.org/doi/10.1103/PhysRevD.73.032002.

[68] Longke Li, Jing Yuan, Lin Zhu. *Momentum-correction in signal simulations for decays of charmed baryons at Belle and Belle II*. Belle II Publications, BELLE2-NOTE-TE-2024-013 (internal), June 18, 2024. URL: https://docs.belle2.org/files/460/BELLE2-NOTE-TE-2024-013/1/BELLE2-NOTE-TE-2024-013.pdf.

[69] Longke Li, Kay Kinoshita, Alan Schwartz. *Measurement of branching fractions and search for CP violation with five kinematic asymmetries for $\Lambda_c^+ \to \Lambda K_S^0 K^+$ and $\Lambda_c^+ \to \Lambda K_S^{0+}$ decays*. Belle II Publications, BELLE2-NOTE-PH-2023-067 (internal), June 9, 2024.

[70] Joseph McNeil. *Reconstructing Standard Hyperons at Belle II.* Belle II Note, BELLE2-NOTE-PH-2019-011 (internal), 2019.

[71] J. Yelton et al. *Observation of an Excited Ω^- Baryon.* Vol. 121. American Physical Society, Aug. 2018, p. 052003. DOI: 10.1103/PhysRevLett.121.052003. URL: https://link.aps.org/doi/10.1103/PhysRevLett.121.052003.

[72] T. Lesiak et al. *Measurement of masses and branching ratios of Ξ_c^+ and Ξ_c^0 baryons.* Vol. 605. 3. Physics Letters B, 2005, pp. 237–246. DOI: https://doi.org/10.1016/j.physletb.2004.11.038. URL: https://www.sciencedirect.com/science/article/pii/S0370269304016077.

[73] Y. Li et al. *Measurements of the branching fractions of $\Xi_c^0 \to \Lambda K_S^0$, $\Xi_c^0 \to \Sigma^0 K_S^0$, and $\Xi_c^0 \to \Sigma^+ K^-$ decays at Belle.* Vol. 105. 1. American Physical Society (APS), Jan. 2022. DOI: 10.1103/physrevd.105.l011102. URL: http://dx.doi.org/10.1103/PhysRevD.105.L011102.

[74] Petar Rados. *Tracking Efficiency with Taus: Update on MC15rd.* The Belle II note is currently in preparation. The provided slides are linked in the official (internal) confluence pages of the Belle II Physics Performance Groups. URL: https://indico.belle2.org/event/10572/contributions/68899/attachments/25231/37323/tau_eff_mc15rd_update_9Nov23.pdf.

[75] Y. B. Li et al. *First Measurements of Absolute Branching Fractions of the Ξ_c^0 Baryon at Belle.* Vol. 122. American Physical Society, Feb. 2019, p. 082001. DOI: 10.1103/PhysRevLett.122.082001. URL: https://link.aps.org/doi/10.1103/PhysRevLett.122.082001.

[76] J. M. Link et al. *Measurements of Ξ_c^+ Branching Ratios.* Vol. 571. Phys. Lett. B, 2003, pp. 139–147. DOI: 10.1016/S0370-2693(03)00809-8. arXiv: hep-ex/0305038.

[77] T. Bergfeld et al. *Observation of the Ξ_c^+ charmed baryon decays to $\Sigma^+ K^- \pi^+$, $\Sigma^+ \overline{K}^{*0}$, and $\Lambda K^- \pi^+ \pi^+$.* Vol. 365. Phys. Lett. B, 1996, pp. 431–436. DOI: 10.1016/0370-2693(95)01432-2. arXiv: hep-ex/9508006.

[78] A. Zupanc et al. *Measurement of the Branching Fraction $\mathcal{B}(\Lambda_c^+ \to pK^-\pi^+)$.* Vol. 113. American Physical Society, July 2014, p. 042002. DOI: 10.1103/PhysRevLett.113.042002. URL: https://link.aps.org/doi/10.1103/PhysRevLett.113.042002.

[79] M. Ablikim et al. *Measurements of Absolute Hadronic Branching Fractions of the Λ_c^+ Baryon.* Vol. 116. American Physical Society, Feb. 2016, p. 052001. DOI: 10.1103/PhysRevLett.116.052001. URL: https://link.aps.org/doi/10.1103/PhysRevLett.116.052001.

[80] Y. B. Li et al. *First measurements of absolute branching fractions of the Ξ_c^+ baryon at Belle.* Vol. 100. American Physical Society, Aug. 2019, p. 031101. DOI: 10.1103/PhysRevD.100.031101. URL: https://link.aps.org/doi/10.1103/PhysRevD.100.031101.